The University Of Sheffield.

Fabrication of Protein Nanostructures

By:

Sijing Xia

A thesis submitted in partial fulfilment of the requirements for the degree of Doctor of Philosophy

The University of Sheffield

Faculty of Science

Department of Chemistry

September 2015

Declaration

The work described in this thesis was undertaken at the University of Sheffield between October 2011 and July 2015 under the supervision of Professor Graham J. Leggett. Unless otherwise stated, it is the work of the author and has not been submitted in whole or in part for any other degree at this or any other institute.

September 2015

Signed: …….

Sijing Xia

Department of Chemistry,

Dainton Building,

University of Sheffield,

Brook Hill,

Sheffield, UK,

S3 7HF

Acknowledgement

First of all, I would like to thank Professor Graham J. Leggett giving me the opportunity to join his group. Thanks a lot for his patient guidance and kind support through this project.

Secondly, I would like to give my thanks to the members past and present in GJL group. A special mention has to go to Robert Ducker, Osama EI. Zubir, Anna Tsargorodska, Mar Cardellach, Nan Cheng, Abdullah Souwaileh, Alexander Johnson, Paul Chapman, Omed QHA AI-Jaf, Hang Xu, Rebecca Smith, Charlie Smith, Max W. Chamber, Brice Darroch and Deborah B Hammond.

I would also like to thank all the other friends in University of Sheffield for their kindness and help over the last few years, with much respect going to Claire Hurley for her kind help on XPS; Michael Carton for his supply of proteins and Keith Owen for his help on Karl Fisher titration.

I really appreciate the University of Sheffield providing the financial support for my PhD research in UK.

Finally, I would like to thank my family, my dear parents Ye Xia and Xiaolin Li, and my husband Jie Dai. I would not have been able to do this without their love and support.

Publications

1- Abdullah M. Alswieleh, Nan Cheng, Irene Canton, Burcin Ustbas, Xuan Xue, Vincent Ladmiral, Sijing Xia, Robert E. Ducker, Osama El Zubir, Michael L. Cartron , C. Neil Hunter, Graham J. Leggett*, and Steven P. Armes*, "Zwitterionic Poly(amino acid methacrylate) Brushes", *J Am Chem Soc* **136**, 9404-9413 (2014).

2- Sijing Xia, Michael Cartron, James Morby, C. Neil Hunter* and Graham J. Leggett*, "Fabrication of Nanometer and Micrometer Scale Protein Structures by Site-Specific Immobilization of Histidine-Tagged Proteins to Aminosiloxane Films with Photoremovable Protein-Resistant Protecting Groups", in preparation.

3- Sijing Xia and Graham J. Leggett*, "Site-specific attachment of proteins to nanostructured surfaces formed by UV photolithography, interferometric lithography and scanning near-field photolithography", Poster presentation at Soft Matter Conference, Freiburg Institute of Advanced Studies, Germany, October 2013

4- Sijing Xia and Graham J. Leggett*, "APTES SAMs formation and protein patterning", Poster presentation at Surface Science of Biologically important interfaces (SSBII) 14, University of Manchester, UK, 2012

Contents

Abbreviations

ABNTA	Aminobutylnitrilotriacetic acid
ADP	Adenosine diphosphate
AFM	Atomic force microscope
APDMES	Aminopropyldimethylethoxysilane
APTES	3-aminopropyltriethoxysilane
Aryl azide	4-azido-3-(triethoxypropysilane) benzamide
ATP	Adenosine triphosphate
ATRP	Atom radical transfer polymerization
BE	Binding energy
CCD	Charge-coupled device
CDI	Carbodiimide
CuAAC	Copper(I)-catalyzed azide-alkyne cycloaddition
DLD	Delay-line detector
DMF	Dimethylformamide
DPN	Dip-pen nanolithography
β-DDM	n-Dodecyl β-D-maltoside
EBL	Electron Beam Lithography
EDC	1-ethyl-3, 3-dimethyl carbodiimide
EDTA	Ethylenediaminetetraacetic acid
FWHM	Full width at half maximum
GA	Glutaraldehyde
HEPES	4-(2-hydroxyethyl)-1-piperazineethanesulfonic acid
HFE	Hydrofluororther
His	Histidine
IL	Interferometric lithography
ImR	Imprint resist
ISC	Intersystem crossing

L-B	Langmuir-Blodgett
LH1	Light-harvesting complex 1
LH2	Light-harvesting complex 2
MCH	Multivalent chelator heads
MeNPOC	Methyl-6-nitropiperonyloxycarbonyl
MHA	16-mercaptohexadecanoic acid
MPTMS	3-(mercaptopropyl) trimethoxysilane
NADPH	Nicotinamide Adenine Dinucleotide Phosphate Hydrogen
NHS	N-hydroxysuccinimide
NIL	Nanoimprint lithography
NPEOC	2-nitrophenylethoxycarbonyl
NPPOC	Nitrophenylpropyloxycarbonyl
NVOC	Nitroveratryloxycarbonyl
OEG	Oligo (ethylene glycol)
OTS	Octadecyltrichlorosilane
PBS	Phosphate buffered saline
PCysMA	Poly (cysteine methacrylate)
PDMP	Poly (2, 2-dimethoxy nitrobenzyl methacrylate-r-methyl-methacrylate-r-poly (ethylene glycol) methacrylate)
PDMS	Polydimethylsiloxane
PEG	Poly (ethylene glycol)
PI	Isoelectric point
PMMA	Poly (methyl methacrylate)
POEGMA	Poly (oligo (ethylene glycol) methacrylate)
Q	Ubiquinone
QH_2	Ubiquinol
RC	Reaction centre
RCA	Radio corporation of America
RIE	Reactive ion etching
RMS	Root mean square

SAMs	Self-assembled monolayers
SDS	Sodium dodecyl sulphate
SEM	Scanning electron microcopy
SIMS	Second ion mass spectroscopy
SNOM	Scanning near-field optical microscope
SNP	Scanning near-field photolithography
TFAA	Trifluoracetic anhydride
UHV	Ultra-high vacuum
XPS	X-ray photoelectron spectrometer

List of Figures

List of Tables

List of Schemes

Abstract

Plants can convert light energy to chemical energy with high efficiency through photosynthesis. Our group are trying to adapt the photosynthetic mechanisms of plants to anthropogenic purposes in order to develop biologically-inspired systems for solar energy collection and may provide a solution for energy shortage. We aim to reconstruct a synthetic low-dimensional system of the complete photosynthetic pathway of the bacterium Rhodobacter sphaeroides on a chip. The main focus of this thesis is to develop the methodologies to fabricate multiple protein patterns on silica surfaces and finally those biochips with multiple protein patterns will be used in the study on photosynthesis in this low dimensional chemistry (LDC) programme. Different photochemical techniques, including mask-based UV lithography, interferometric lithography (IL) and scanning near-field photolithography (SNP) have been used as tools for the fabrication of micrometre and nanometre scale structures on the self-assembled monolayers (SAMs) of silanes.

SAMs of 3-aminopropyltriethoxysilane (APTES) were prepared on silica surfaces. The amount of water in reaction solvent was investigated using Karl Fisher Titration method. Water content ranged from ca. 67 ppm to 93 ppm was found out in the solvent of toluene. The wettability, roughness and thickness of APTES films were measured using, respectively, contact angle goniometer, atomic force microscope (AFM) and ellipsometry. Their variations depending on the reaction time and adsorbate's concentration were found out. The contact angle could go up to ca. 55^{o} and the roughness was lower than 0.5 nm. Surface composition of APTES films was obtained by X-ray photoelectron spectrometer (XPS), the results of which combined with the thickness data suggested the formation of multiple layers.

SAMs of aminopropyltriethoxysilane protected by oligo (ethylene glycol) modified 2-nitrophenylethoxycarbonyl (OEG-NPEOC-APTES) were prepared on silica surfaces. The effect of UV exposure on OEG-NPEOC-APTES films was studied by XPS and

their deprotection rates under 244 nm and 325 nm laser were found out. The methodologies to fabricate micrometer and nanometer scale patterns by mask-based UV lithography, IL and SNP were developed. Single and multiple proteins were immobilized on Micro- and nano-patterned OEG-NPEOC-APTES SAMs to form very nice protein patterns.

Attachment of aminobutylnitrilotriacetic acid (ABNTA) to UV laser selectively deprotected OEG-NPEOC-APTES SAMs had been realized to enable the spatially selective fabrication of specific protein-binding surface sites. The efficiency of patterning and the binding affinity of Histidine (His) - tagged proteins was investigated by ellipsometry and by fluorescence measurements using confocal laser scanning microscopy. The results showed that an exposure dose of ca. 5 Jcm^{-2} is sufficient to ensure the formation of a monolayer of site-specifically oriented protein. The methodology to prepare micrometer and nanometer scale patterns of His-tagged GFP and CPCA onto NTA/Ni^{2+} functionalized structures had been developed.

SAMs of 4-azido-3-(triethoxypropylsilane) benzamide (aryl azide) had been prepared on silica surfaces. The effect of UV exposure on aryl azide films was obtained by XPS and contact angle measurements. Their deprotection rate under 244 nm and 325 nm laser were found out. An exposure dose of ca. 0.8 Jcm^{-2} under 244 nm laser and that of ca. 33 Jcm^{-2} under 325 nm laser were sufficient to convert eighty percentage of azide group to amide. The photoreactions of aryl azide SAMs with different amines were investigated by XPS and contact angle measurements. The results confirmed the reaction between amine and azide groups under irradiation. The methodology to pattern aryl azide SAMs at the nanometer scale was achieved by using IL followed by passivation with octadecylamine. Membrane proteins were photochemically coupled to the unmodified regions through flood exposure successfully.

Chapter 1 Introduction

1.1 General Introduction

Recently energy shortage has raised the importance of fully exploiting the enormous amounts of solar energy that fall upon the earth's surface. Plants can convert light energy to chemical energy with high efficiency through photosynthesis. By studying on the photosynthesis process we may learn how to take advantage of solar energy more effectively. To build up a biologically-inspired system that replicates the photosynthetic apparatus, oriented patterning of proteins, especially membrane proteins involved in photosynthetic process is an essential part. The history of protein patterning began in 1978 when MacAlear and Wehrung tried to use photoresist lithography to make patterns on an underlying compressed proteinaceous layer.[1,2] The technique was originally developed for application in molecular electronic devices and for the development of biological computers. Subsequently, the field of protein patterning has expanded rapidly and a growing number of new techniques have appeared in research papers and patents in the past ten years, including methods using patterning by microfabrication, photochemistry and other apparatus.

1.2 Self-Assemble Monolayers

Self-assembled monolayers (SAMs) are ordered molecular assemblies formed by the adsorption of a surfactant on a solid surface. Monolayers can be spatially organised on a surface, meaning that proteins can be patterned through the spatial control of the chemistry of the SAMs. The history of SAMs can be traced back to the beginning of the last century. In 1917 Irving Langmuir studied the molecular films formed at the air-water interface and introduced the concept of a monolayer.[3-5] A "Langmuir monolayer" is a monomolecular film of amphiphile surfactant at the air-water interface. Then in 1934 Katherine Blodgett invented the Langmuir-Blodgett (L-B) techniques[6] for the transfer of fatty acid molecules with long hydrocarbon chains and hydrophilic head

groups from the air-water interface onto a solid substrate as shown in figure 1.1. Loosely packed monolayers can be formed subsequently on the pure water surface and following compression yield to two dimensional crystalline structures.

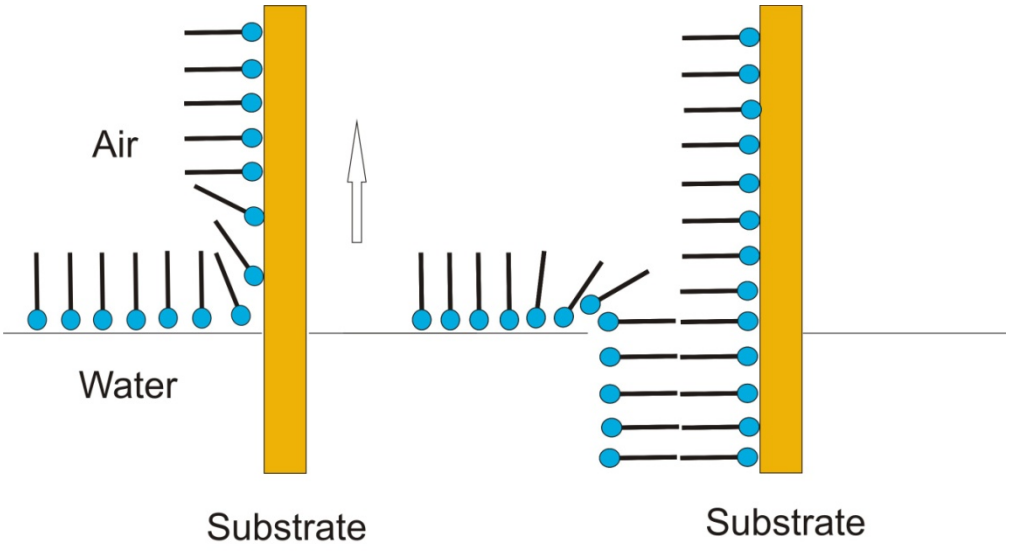

Figure 1.1 The process of using Langmuir-Blodgett techniques to transfer monolayers or multilayers onto a solid substrate.

In 1983 Jacob Sagiv and his co-workers first reported the formation of octadecyltrichlorosilane (OTS) films on oxide surface.[7] These films consisted of close-packed monolayers of amphiphiles on a solid surface which exhibited similar structural characteristics to L-B films. However, the films were not formed by compression, in contrast with L-B technique, but by simple immersion of a substrate into an organic solvent containing surface-active molecules. Spontaneous adsorption of monolayers would occur at the surface, a process known as "self-assembly" (Figure 1.2). Subsequently, this method has become widely used for monolayer preparation. The driving forces for SAM formation include formation of a strong interaction between the head group of the adsorbate and the surface and non-covalent intermolecular interactions that drive the ordering of adsorbate. As reported,[8] various combinations of substrates and adsorbates have been used to form SAMs including organosilane derivatives on hydroxylated surfaces[9] for example alkylaminosilanes on silicon dioxide; organosulfur adsorbates on metal and semiconductor surfaces[10]; alkanoic acids on

AgO[11]; alkyl monolayers on silicon[12] and diphosphonic acids on metal oxide surfaces.[13]

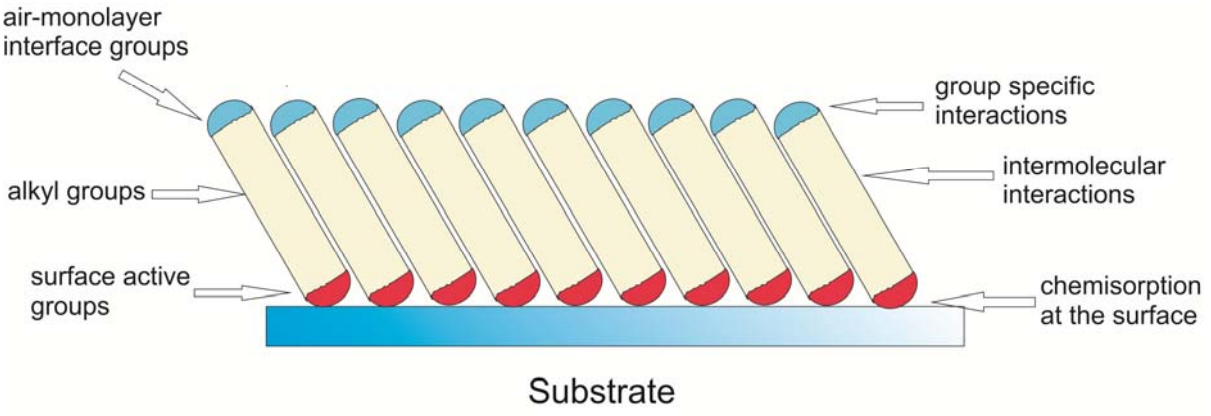

Figure 1.2 A close-packed ordered SAM structure formed by immersing a suitable substrate into a solution of a surface-active material.

Monolayers of organosilicon derivatives on hydrated surfaces such as 3-aminopropyl triethoxysilane (APTES) on silica have been widely used to prepare surfaces for further functional patterning,[14] for example the protein patterning. The mechanism of self-assembly is the formation of a polysiloxane layer which is connected to surface silanol groups (-SiOH) through Si-O-Si bonds.[8] As shown in figure 1.3, the Si-O bonds can be connected either to another polysiloxane chain or to the silica surface. The amount of water in solution plays an essential part in controlling the structure of the monolayers[15,16] because water is involved in the formation process of silane SAMs. The absence of water will cause incomplete monolayers[17] while an excess of water leads to facile polymerization in solution and polysiloxane deposition at the surface.[18] Temperature also has an effect on monolayer formation. As the temperature increases, the preference for surface reaction increases, which leads to the formation of ordered and structured assembly. The reaction time and concentration both affect the quality of monolayers: insufficient reaction time or too dilute a solution will lead to the formation of incomplete monolayers. Depending on solvent, adsorbate and concentration, different reaction times are required to prepare high quality monolayers. For example, to prepare alkyltrichlorosilane monolayers, Silberzan et al.[19] reported that monolayer formation

was completed within 3 minutes while Banga et al.[20] suggested that 90 minutes was better but Wasserman et al.[17] suggested over 24 hours was needed. It has been found that lots of factors would affect the silane formation but the best method of it is still dispute.

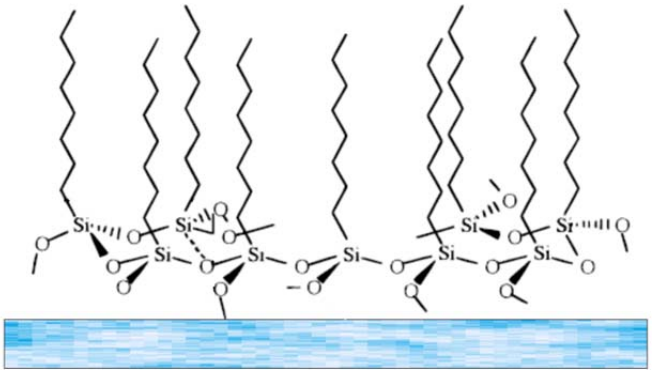

Figure 1.3 Schematic description of polysiloxane at the monolayer-substrate surface.[8]

1.3 Protein Immobilization Strategies

Immobilization is defined as the attachment of molecules to a surface resulting in reduction or loss of mobility. Protein immobilization with orientation is the most important part to realize the potential of protein biochips. Proteins should be immobilized onto an optimal surface with high density. Glass or silicon slides derivatised with SAMs of organosilanes are suitable substrates for immobilization of proteins as adsorbed film can enhance the biocompatibility of the surface and protect proteins from denaturation during immobilization. In order to retain biological activity, protein should be attached onto the surface through special strategies to avoid structural change and consequent loss of function. Currently, there are three common protein immobilization strategies including physical, covalent, and bioaffinity immobilization.[21]

1.3.1 Physical Immobilization

Proteins can be attached onto surfaces through physical adsorption via non-specific, non-convalent interactions including ionic interactions, hydrogen bonds and the hydrophobic effect. The resulting layer will be heterogeneous and randomly oriented

because each protein may contact the surface in different orientation to minimize the free energy of interaction with the surface and previously adsorbed proteins. This method has the obvious drawbacks that random orientation may lead to loss of protein activity and intermolecular forces are so weak that some buffers or detergents could remove proteins easily. Once physically adsorbed, most proteins will undergo conformation change so that adsorption becomes irreversible.

1.3.2 Covalent Immobilization

Immobilization of proteins onto modified supports through covalent bonds seems more practical method. Covalent bonds can be formed between side-chain-exposed or end-terminal groups in proteins and derivatised surfaces, resulting in irreversible binding and high surface coverage. Chemical binding through side chains of amino acids is often random because it is based upon residues typically present on the exterior of the protein. Table 1.1 summarizes some commonly available functional groups in proteins and corresponding derivatised surfaces.

Table 1.1 Functional groups in proteins and corresponding derivative surfaces[21]

Functional groups	Amino acids	Surfaces
$-NH_2$ (Side-chain and N-terminus)	Lys, hydroxyl-Lys	Carboxylic acid
		Active ester (NHS)
		Epoxy
		Aldehyde
-SH (Side-chain)	Cys	Maleimide
		Pyridyil disulfide
		Vinyl sulfone
-COOH (Side-chain and C-terminus)	Asp, Glu	Amine
-OH (Side-chain)	Ser, Thr	Epoxy

1.3.2.1 Amine Chemistry

All proteins have an N-terminus and many proteins contain lysine residues. In some cases these are accessible for surface coupling. Active esters, formed by treatment of carboxylic acids with N-Hydroxysuccinimide (NHS) and a carbodiimide, are very reactive towards amines, and N-Hydroxysuccinimidyl esters are widely used both for functionalization of proteins and also for surface attachment (Scheme 1.1a). The use of NHS chemistry on SAMs has been reported by Patel et al.[22], who prepared an active ester derivative on carboxylated surfaces. A solution of 1-ethyl-3, 3-dimethyl carbodiimide (EDC) and NHS in DMF was used to form active ester on the samples' surface. Then the sample was used to immobilize proteins at the N-terminus or with lysine residues depending on the pH condition. Carboxylated surfaces can be activated also by formation of an intra-monolayer anhydride (Scheme 1.1b). Yang et al.[23] reported that trifluoracetic anhydride (TFAA) was used to prepared anhydride surfaces through their reaction with carboxylated terminated monolayers. The active film was then put into protein solution to carry out further immobilization steps. Aldehyde is another commonly used coupling agent with amine groups, which would interact with amine to yield imide bonds (Scheme 1.1c). Cross-linking between amine groups via reaction with glutaraldehyde (GA) is a widely used preparation technique in microscopy. H. Wang et al.[24] reported that amine surfaces could be functionalized by aldehyde groups through their reaction with GA. Proteins with lysine residues can be attached subsequently onto the active aldehyde surface.

(a)

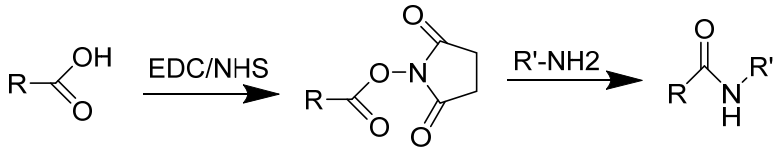

(b)

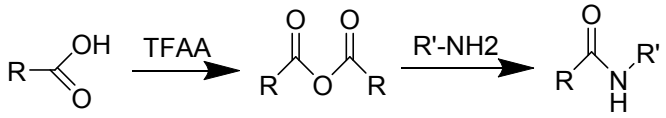

(c)

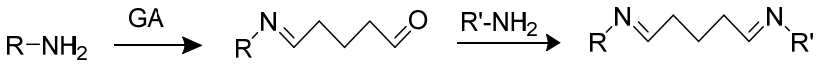

Scheme 1.1 (a) Activation of a carboxylic acid terminated monolayer by EDC/NHS, followed by reaction with an amine to yield an amide linkage; (b) Activation of a carboxylic acid terminated monolayer by TFAA, followed by reaction with an amine to yield an amide linkage; (c) Activation of an amine terminated monolayer by GA to form an aldehyde functionalized surface, followed by reaction with an amine to yield an imine linkage.[25]

1.3.2.2 Thiol and Carboxyl Chemistry

All proteins have a C-terminus. Glutamic acid, aspartic and cysteine residues are also on proteins but not as abundant as lysine. Some coupling approaches have been applied to form covalent bonds between those side or terminal groups and derivatized surfaces. Sulfhydryl groups in cysteine can undergo an addition reaction with a maleimide double bond at pH 6.5 to 7.5 on maleimide derivative surfaces (Scheme 1.2a).[26-28] They can participate in disulfide exchange reactions with the disulfide derivatized surfaces (Scheme 1.2b).[29] They can also undergo Michael addition reactions with vinyl sulfone derivatized surfaces (Scheme 1.2c).[30,31] In carboxyl chemistry, carboxyl groups in aspartic and glutamic acid are usually activated by carbodiimide (CDI) and then covalently binding with amine surfaces (Scheme 1.2d).[32]

(a)

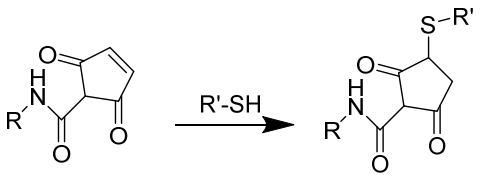

(b)

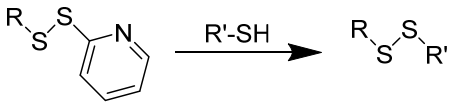

(c)

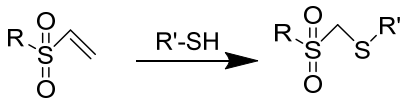

(d)

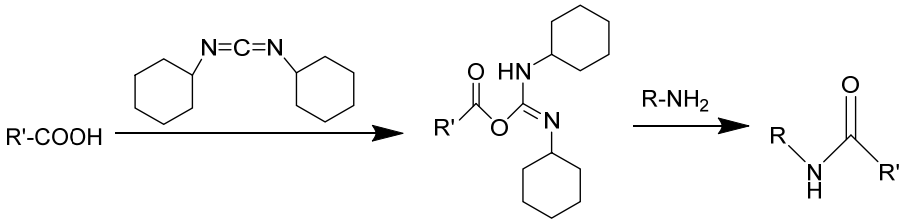

Scheme 1.2 Thiol chemistry on (a) maleimide derivatized, (b) disulfide derivatized, (c) vinyl sulfone derivatized surfaces and (d) carboxyl chemistry using carbodiimide activation.

1.3.2.3 Photoactive Chemistry

In photoimmobilization, photosensitive reagents are activated by incident photons. The reagents undergo chemical processes that lead to the formation of covalent bonds between the photogenerated intermediates and the biomolecules.[33] The photoreaction can be carried out under mild conditions efficiently, and may even facilitate immobilization of biomolecules without active functional groups. Thus the use of photoactive chemistry has become one of the most popular approaches of protein attachment. Three widely used photosensitive reagents are arylazide[34], nitrobenzyl[35] and diazirine compounds[33]. In arylazide chemistry, UV irradiation of an arylazide yields a reactive nitrene that can insert into covalent bonds including C-H, C-C, C=C, N-H, O-H

and S-H bonds (Scheme 1.3a). Nitrobenzyl chemistry, often called caging chemistry, represents a slightly different approach. It involves a protecting group known as "cage" for the molecule to inhibit the normal reactivity of a functional group. The cage can be broken down by irradiation with UV light generating a ketone, carbon dioxide and free reactive group (Scheme 1.3b). Commonly used cage groups include nitroveratryloxycarbonyl (NVOC) and methyl-6-nitropiperonyloxycarbonyl (MeNPOC).[36,37] In Diazirine chemistry, UV irradiation yields an active carbene, which can insert into C-H, C-C, C=C, N-H, O-H, or S-H bonds (Scheme 1.3c).

(a)

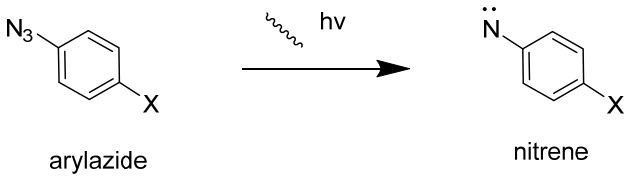

(b)

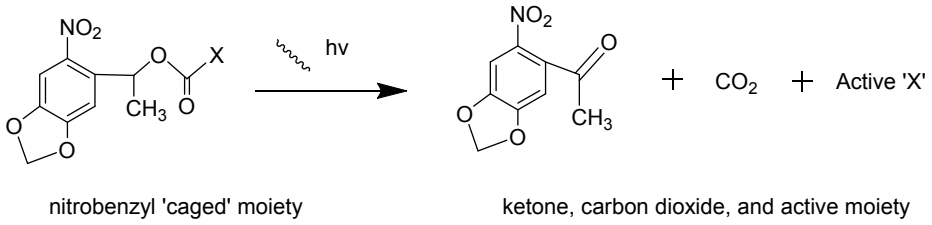

(c)

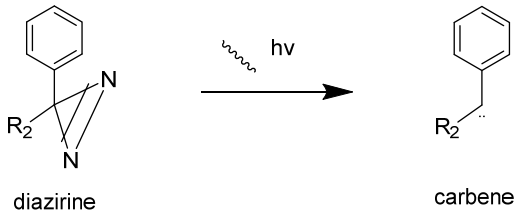

Scheme 1.3 Photoactive chemistry: (a) arylazide chemistry, (b) nitrobenzyl chemistry and (c) diazirine chemistry.

1.3.3 Affinity Immobilization

Site-specific affinity immobilization of proteins is better than covalent attachment because proteins can be attached onto surfaces in a certain orientation and in a

well-ordered manner resulting in homogeneous attachment. Functional domains on proteins can be exposed sufficiently due to their predictable orientation. Moreover, it can offer a reversible bonding of proteins creating reproducible attachment. The Avidin-Biotin system and nitriloacetic acid (NTA) - Ni^{2+} - Histidine (His) Tag system are two commonly used technologies in generating biocompatible surfaces.

1.3.3.1 Avidin-Biotin System

Avidin is a tetrameric glycoprotein that is soluble and stable in aqueous solutions with wide ranges of pH and temperature. Strepavidin is a closely related tetrameric protein but differs slightly in its molecular weight, amino acid composition and isoelectric point (pI). Both avidin and strepavidin display high affinity and specific binding to biotin ($K_a = 10^{15} M^{-1}$), which can rapidly bind to them in a 4:1 stoichiometry in a quasi-irreversible, non-covalent interaction. Biotin is a vitamin that is formed naturally in all living cells (Scheme 1.4a).[38] The bicyclic ring in it should be kept free to interact with avidin but the carboxyl group on the acid end can be modified to generate biotinylation reagents used for conjugation with proteins. For example, the NHS ester of biotin is a common biotinylation reagent to target amine groups (Scheme 1.4b),[39] while biotin hydrazide can be used to target carbohydrates or carboxyl groups (Scheme 1.4c).[40,41]

(a)

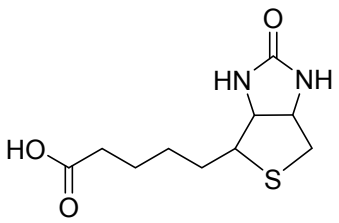

(b)

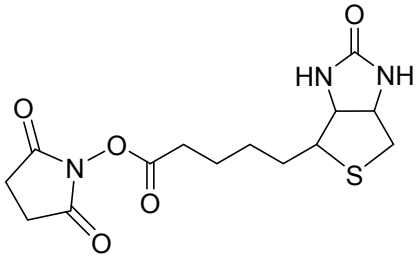

(c)

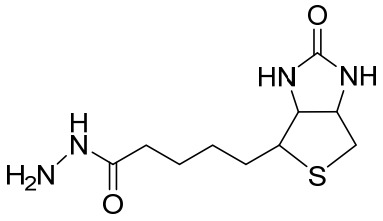

Scheme 1.4 Chemical structures of (a) biotin; (b) biotin NHS ester and (c) biotin hydrazide.

Typically, a biotin-avidin-biotin sandwich architecture is built up on surfaces, where biotin is firstly immobilized onto surface to create the first layer, then avidin is bond to the biotinylated surface through its biotin binding sites to create the second layer. The remaining biotin binding sites are used to capture biotinylated proteins (Figure 1.4).[42]

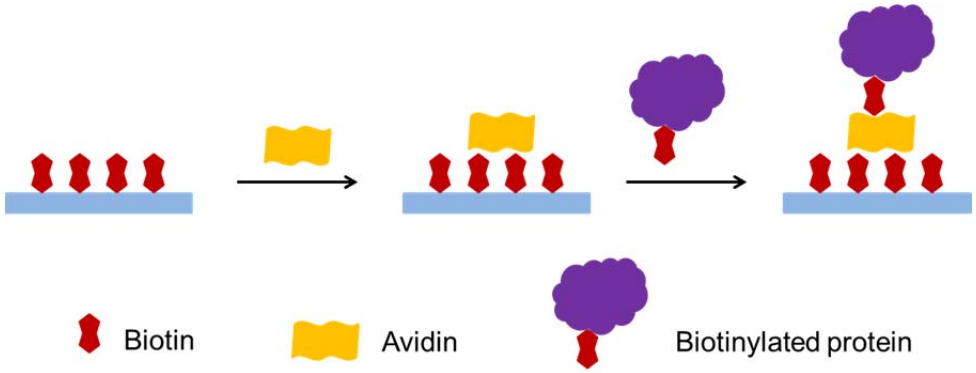

Figure 1.4 Immobilization of a biotinylated protein in a sandwich format.

Biotin photochemistry is also commonly used for attachment of proteins. There are two main types of methodology: photoactivable and photocleavable chemistry. Manchumas Hengsakul and Anthony E. G. Cass reported that they prepared a photobiotin named N-(4-azido-2-nitrophenyl)-N¢-(N-dbiotinyl-3-aminopropyl)-N¢-methyl-1, 3-propanediamine (acetate salt).[43] It contained three different functional parts. The photoactivable group was used to be selectively connected to the polymer surface. After irradiation, the exposed parts of the aryl azide would be converted into reactive aryl nitrenes which could insert into C-H bonds or other chemical groups (OH, NH, NO_2 etc.) of polymers and covalently bind them to the surface (Scheme 1.5). The biotin group was used to form biotin-avidin complexes with the addition of avidin and then biotinylated biomacromolecules like proteins could be bound to the surface resulting in the biotin-avidin-biotin structure, which could retain their bioactivities. The linker arm joined these two groups together.

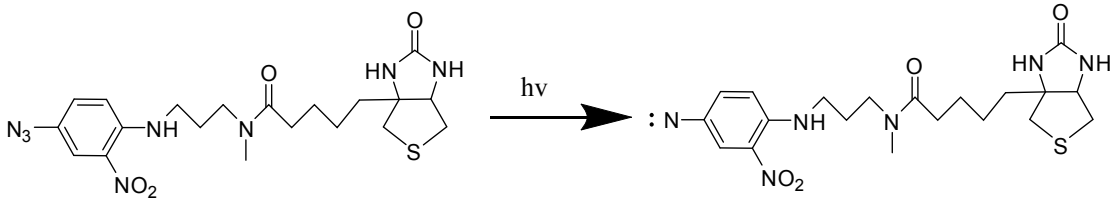

Scheme 1.5 Photoactive reaction of the photobiotin[43]

Photocleavable biotin, also known as caged biotin, usually has a photolabile group on

one of the nitrogen atoms of the imidazole ring, which can block the biotin from binding with avidin. Upon UV irradiation, the photolabile group is cleaved and the biotin is free to interact with avidin.[44] For example, Nitroveratryloxycarbonyl (NVOC) is a popular photolabile group, shown in Scheme 1.6. There is a number of reports of the spatially-directed immobilization of proteins on NVOC caged-biotin derivatized surfaces after activation by irradiation.[45,46]

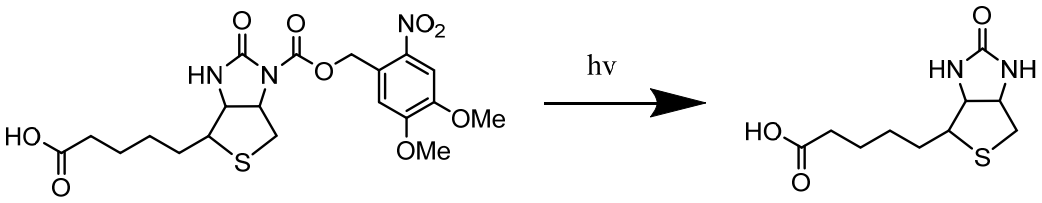

Scheme 1.6 Photocleavable reaction of NVOC caged-biotin

1.3.3.2 NTA-Ni^{2+}-His-Tag System

Genetic engineering can produce proteins with affinity tags, the most popular one of which is histidine (His). Proteins with a His-tag at the C- or N- terminus can be immobilized via a nickel-chelated complex like Ni-nitriloacetic acid (NTA) (Figure 1.5). NTA can be covalently bound to the surface via EDC-NHS or maleimide chemistry.[47,48] A nickel ion with octahedral coordination has four ligands donated by NTA molecules and the remaining two could be occupied by two imidazole groups from the His-tag on a protein. The binding is highly specific and entirely reversible upon the addition of a competitive ligand such as imidazole or EDTA so that the immobilized proteins can be detached leading to the repeated use of the same surface.

(a) (b)

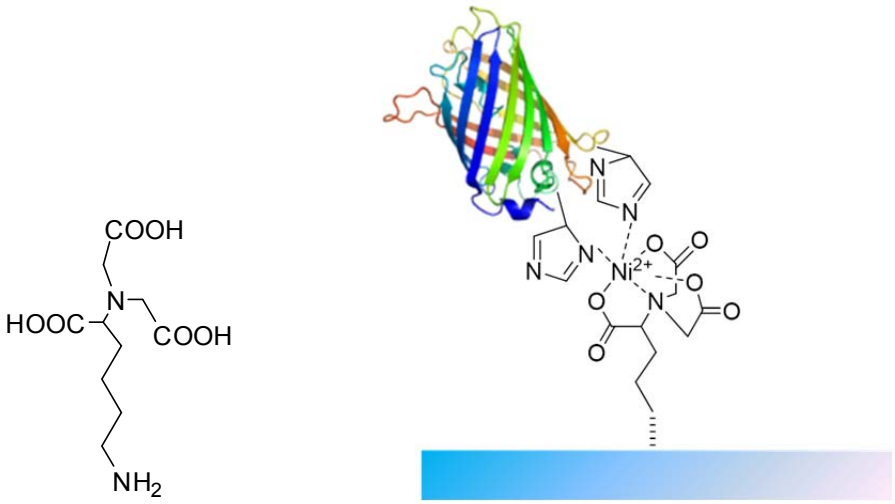

Figure 1.5 (a) Chemical Structure of aminobutyl-NTA, (b) schematic representation of the binding of His-tagged proteins on a Ni-NTA surface.

Hochuli first used NTA to purify recombinant proteins with His-tag in 1987.[49] Then it has been developed as an indispensable tool to immobilize proteins with high specificity on solid surfaces via NTA-Ni^{2+}-His-Tag system. George M. Whitesides and his colleague firstly developed a procedure to modify the gold surface with self-assembled monolayers (SAMs) of alkanethiolates for the binding and study of Histidine-tagged Proteins in 1996.[50] The SAMs were prepared by the adsorption of a mixture of two alkanethiols onto a gold surface: one thiol that terminated with a nitrilotriacetic acid (NTA) group and a second thiol that terminated with a tri (ethylene glycol) group, a group that resists protein adsorption (Figure 1.6). They tried to prepare a surface that would (i) control the orientation of the immobilized protein such that the active site would be accessible to molecules in solution, (ii) specifically immobilize a protein of interest while resisting nonspecific binding of other proteins, and (iii) avoid the requirement for nonspecific, covalent modification of the protein.

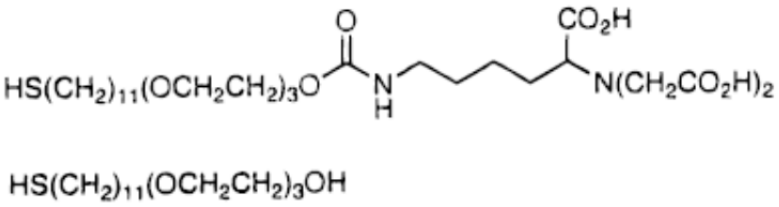

Figure 1.6 Chemical structures of thiols terminated with NTA (top) and OEG (bottom).[50]

In 1997 Horst Vogel and his colleagues developed a method for reversible immobilization of functional proteins on oxide surfaces like glass, silicon and quartz.[48] They prepared SAMs of 3-(mercaptopropyl)trimethoxysilane (MPTMS) on the active oxide substrate, functionalized them with NTA-maleimide via covalent bonding and subsequently loaded them with Ni^{2+} (Figure 1.7). They also demonstrated how His-tagged proteins can be immobilized reversibly onto those surfaces and suggested that this method opened new ways for structural investigation of proteins and receptor-ligand interactions in the future.

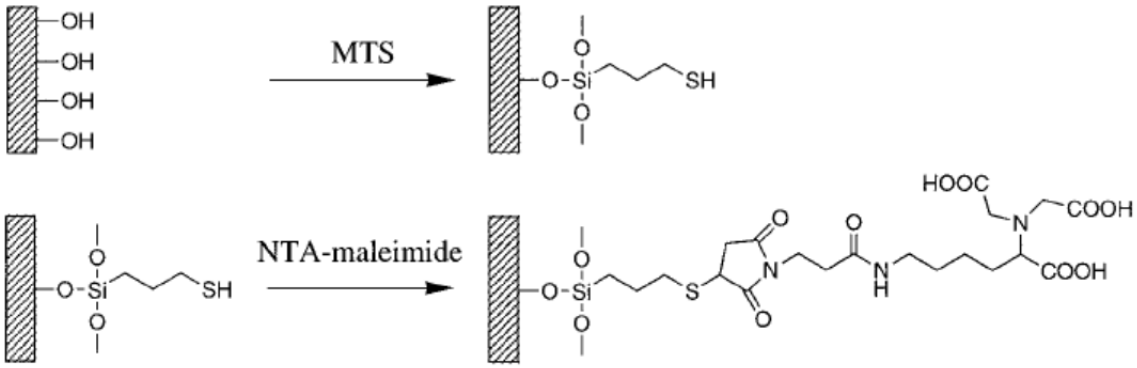

Figure 1.7 Chemical modification process of an oxide surface derivative with NTA-maleimide.[48]

Later, surfaces more densely covered by NTA were reported, leading to more stable

site-specific binding. A higher density of metal chelator at the surface has been achieved via multivalent chelator heads (MCH).[51,52] Suman Lata et al. synthesized several supramolecular entities containing two to four nitrilotriacetic acid (NTA) moieties (termed bis-, tris-, and tetrakis-NTA)[52] (Figure 1.8) and they found the binding stability of His-tagged proteins substantially increased with increasing number of NTA moieties. They also found that when coupling MCH onto glass surfaces modified with PEG polymer, nonspecific bonding could be reduced.[51]

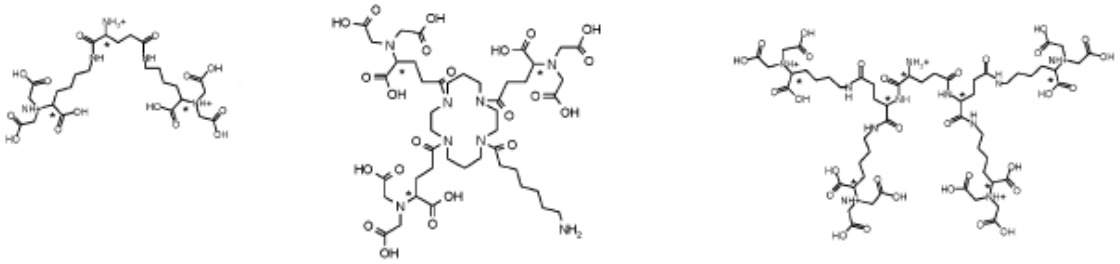

Figure 1.8 Chemical structure of bis-NTA (left), tris-NTA (middle) and tetrakis-NTA (right).[51]

1.4 Nonspecific Attachment

Proteins are regarded as 'sticky' biomacromolecules, which means most proteins will adsorb strongly onto surfaces. Proteins containing anionic, cationic, hydrophobic and hydrophilic residues may explore a large conformational space when interacting with a surface. Thus the inhibition of nonspecific attachment of proteins to other regions of the sample seems an important problem in protein patterning. We call the surfaces that resist protein adsorption 'nonadsorbing' or 'inert'. They usually exhibit four molecular level characteristics.[53] First, they are hydrophilic; second, they have hydrogen-bond acceptors; third, they do not have hydrogen-bond donors; fourth, they have neutral electrical charge. But some exceptions like SAMs presenting mannitol present inert surfaces even though they include many hydrogen-bond donors.[54] Whitesides and coworkers thought that the interaction between the surface and water was the key to understand the mechanism of protein resistance.[53] In the model of protein adsorption

onto surfaces (Figure 1.9), an interface is first formed between the surface and protein. There are two further separate interfaces involved, the interface between the surface and water, and the interface between the protein and water. Second, the protein will undergo conformational changes when adsorbing onto the surface, which leads to an increase in the interactions between the protein and surface. However, the detailed mechanism of resistance to the adsorption of proteins has not been well defined at present.

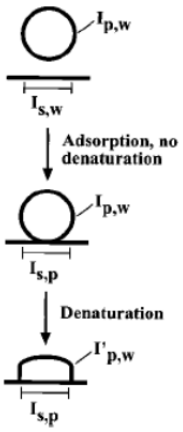

Figure 1.9 Schematic illustration of the interfaces that are involved in the process of protein adsorption onto surfaces (I: interface, P: protein, W: water, S: solid).[53]

Poly (ethylene glycol) (PEG) and its derivatives are commonly used to prepare inert surfaces. Harris et al. first reported the biocompatible character and protein resistance of PEG functional surfaces.[56] However, as a polyether, PEG is unstable in environments rich in oxygen or transition metal ions, [57-59] where the hydroxyl group in PEG is oxidized rapidly to yield aldehydes and acids.[60,61] SAMs presenting oligo (ethylene glycol) (OEG) groups on their surface could be another choice. It was reported that SAMs terminated with $(EG)_{n=3-7}OH$ have the best resistance to protein adsorption. Meanwhile, $(EG)_{n=3-7}OH$ groups resist the adsorption of proteins as well as $(EG)_{n=17}OH$ groups.[62,63] Some polymer brushes also exhibit excellent resistance to protein adsorption. Ahmad et al. prepared poly (oligo(ethylene glycol) methacrylate) (POEGMA) bottle-brush films by surface-initiated atom radical transfer polymerization (ATRP) and they selectively degraded the films to yield protein-binding areas. Their results showed that POEGMA brushes were highly protein-resistant.[64] Recently

Alswieleh et al. prepared poly (cysteine methacrylate) (PCysMA) brushes, which is a zwitterionic polymer, and found that they were also showed highly protein-resistant.[65,66] In addition, other SAMs have been found to exhibit resistance to protein adsorption. Mrksich et al. observed that mannitol-terminated SAMs could resist the adhesion of fibroblasts in 2000.[54] Despite the availability of other materials, $(EG)_nOH$ terminated SAMs are still the most widely used non-fouling monolayers.

1.5 Common Surface Analysis Technologies

1.5.1 Contact Angle Goniometer

The contact angle is the angle between the tangent to the drop surface and the solid surface at the perimeter of a drop in contact with a solid (Figure 1.10). It describes the wettability of a solid surface by a liquid drop, whose shape depends on the interaction between two surfaces and surrounding air.

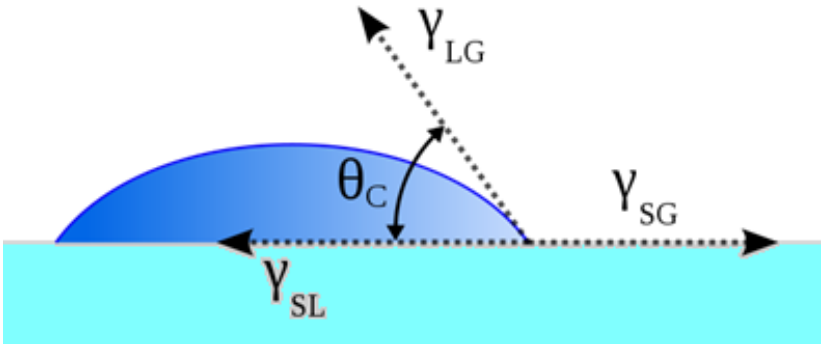

Figure 1.10 Schematic illustration of contact angle on the liquid/solid interface.

A given system of solid, liquid, and vapor at a given temperature and pressure has a unique equilibrium contact angle, which may be described by the Young's equation below.[114] The theoretical description of contact angle comes from the consideration of a thermodynamic equilibrium between the three phases: the liquid phase (L), the solid phase (S), and the gas/vapor phase (G). The equilibrium contact angle reflects the relative strength of the liquid, solid, and vapor molecular interaction.

$$\gamma_{LG} \cos \theta c = \gamma_{SG} - \gamma_{SL}$$

Whereθ_C is the equilibrium contact angle, γ_{LG}, γ_{SG} and γ_{SL} are the liquid/vapour interface energy, solid/vapour interface energy and solid-liquid interface energy respectively.

From Young's equation above, a relationship can be derived that gives the work of adhesion for a known liquid:

$$W_{SLV} = \gamma(1 + \cos \theta)$$

Where W_{SLV} is the solid - liquid adhesion energy per unit area. Analysis of contact angles is capable of providing information about the thermodynamics of the solid surfaces.

If the water contact angle of a water drop is smaller than 90°, the solid surface is considered hydrophilic, while if the contact angle is larger than 90°, the solid surface is considered hydrophobic (Figure 1.11). Rough surfaces can be very water repellent due to the formation of air pockets under the liquid drop. Bico et al. [115] placed a macroscopic drop on a microscopic "spiked" surface and created nearly spherical droplet which they called "Pearl drops".

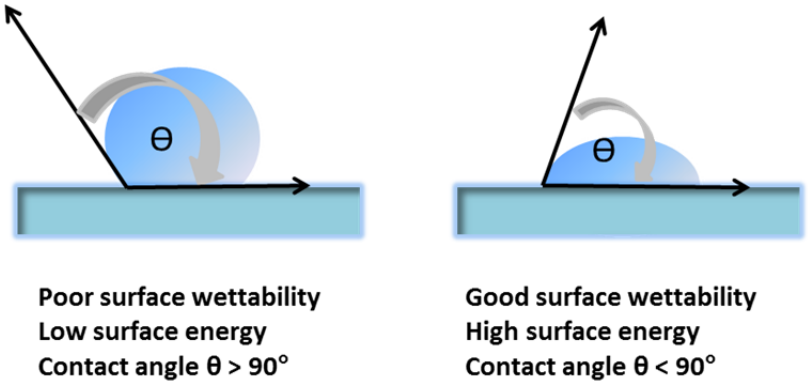

Figure 1.11 Schematic illustration of contact angle on the liquid/solid interface. Left: hydrophobic surface; right: hydrophilic surface.

1.5.2 Ellipsometry

Ellipsometry is an optical technique used to analyse dielectric properties of thin films.[117] By measuring the change of polarization of light, which is reflected off a sample, ellipsometry can yield information about layers that are thinner than the wavelength of the probing light itself, even down to angstrom resolution. The polarization change is determined by the sample's properties such as thickness, complex refractive index or dielectric function tensor. The sample must be uniform and consist of discrete layers that are optically homogeneous and isotropic. In the schematic setup of an ellipsometer (Figure 1.12), light source emits electromagnetic radiation which is polarized by a polarizer. The radiation passes through an optional compensator and falls down onto the sample with a certain angle Φ. After reflection, the radiation will go through a second compensator and analyzer, and finally arrive at the detector.

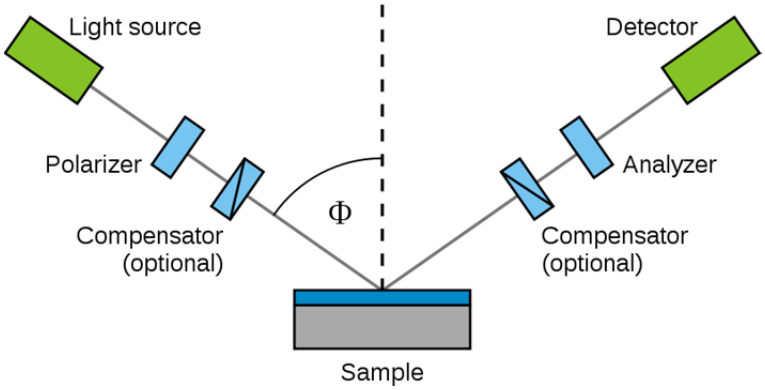

Figure 1.12 Schematic setup of ellipsometric equipment.[118]

Ellipsometry measures the complex reflectance ratio ρ of a system, which can be written as:

$$\rho = \frac{\gamma p}{\gamma s} = \tan(\psi)e^{i\Delta}$$

Where γs and γp denote the amplitudes of the *s* and *p* components. The polarization state of the light incident upon the sample may be decomposed into an *s* and a *p* component (the *s* component is oscillating perpendicular to the plane of incidence and

parallel to the sample surface, and the *p* component is oscillating parallel to the plane of incidence). The complex reflectance ratio ρ can be parametrized by the amplitude component ψ and the phase difference Δ. Normally, a model analysis must be performed on the data collected by ellipsometry because it's not a direct method. The thickness parameters, complex refractive index or dielectric function tensor of all individual layers on a substrate along with the layers' sequence should be considered in this model.[118]

1.5.3 Atomic Force Microscopy

Atomic force microscopy (AFM) is a type of scanning probe microscopy, with resolution on the order of fractions of a nanometre. Binnig et al. invented the first AFM in 1986, and the technique as emerged as one of the most widely used tools for materials characterization.[119] As shown in figure 1.13a, AFM uses a microscopic cantilever with a sharp tip at its apex to scan the specimen surface (Figure 1.13b).[120] The cantilever is typically fabricated from silicon or silicon nitride with a tip radius of curvature on the order of nanometers. When the tip is brought into close proximity with a sample surface, forces between the tip and the sample lead to a deflection of the cantilever according to Hooke's law：

$$F = - kx$$

Where *F* is the force, *k* is the force constant of the cantilever and *x* is the deflection.

Due to the Hooke's law above, the cantilever should be very flexible. Even if the forces are very small, the deflection must be detected as accurately as possible. Thus in order to decrease the spring constant and then provide a higher deflection at a given force, soft materials were used to fabricate the cantilever and its length over width ratio was increased. However, the resonant frequency (ω) of a cantilever is proportional to the square root of its spring constant:

$$\omega = (\frac{1}{2\pi})\sqrt{\frac{k}{m}}$$

The resonant frequency would be decreased if only the spring constant is decreased, leading to high levels of interference by mechanical noise from the environment. To avoid this problem, the mass of the cantilever (m) is reduced along with the spring constant to meet a compromise between the sensitivity to forces and to the background noise because the resonant frequency is also inversely proportional to the square root of the mass of the cantilever. Silicon and silicon nitride cantilevers are thus fabricated using micromachining techniques.

AFM may be used to measure mechanical contact forces, van der Waals forces, capillary forces, chemical bonding, electrostatic forces, magnetic forces and others. Several methods have been used for deflection measurement including electron tunneling[119], optical interference[121], capacitance[122] and optical deflection[123]. But the most commonly used is the beam deflection method. Typically, the deflection is measured using a laser spot reflected from the top surface of the cantilever into an array of photodiodes (Figure 1.13a).

(a)

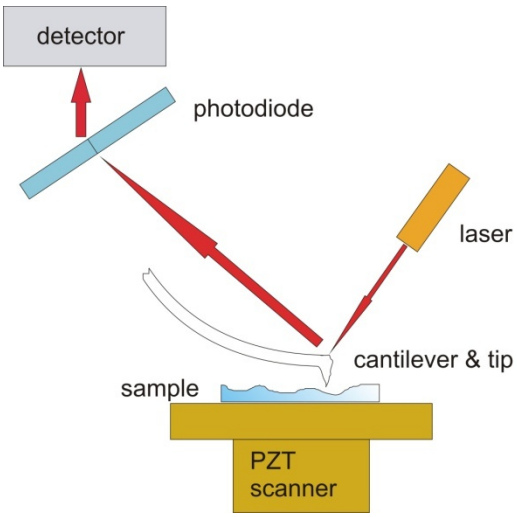

(b)

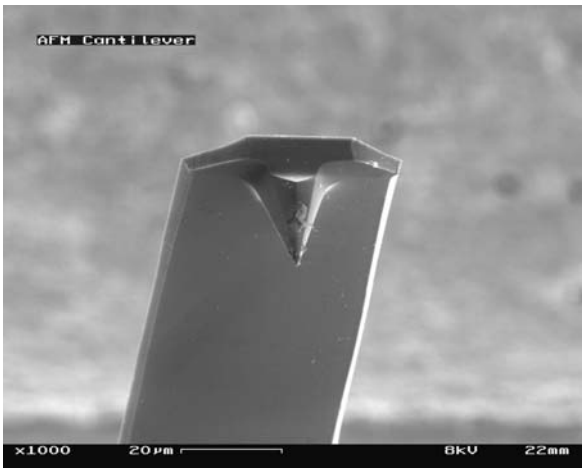

Figure 1.13 (a) Illustration showing the working principle of AFM; (b) Scanning electron microscopy (SEM) image of AFM tip on a cantilever.[124]

AFM can work in different modes depending on the application. The most common ones are contact (static) mode and tapping (dynamic) mode. In contact mode operation (Figure 1.14a),[125] the probes are made of silicon nitride. The tip remains in continuous mechanical contact with the sample. Because the measurement of a static signal is sensitive to noise and drift, low stiffness cantilevers are used to boost the deflection signal. While measurement of attractive forces is possible in principle, attractive forces can be quite strong especially at short range, causing the tip to "snap-in" to the surface.

This makes the measurement of attractive forces very difficult in practice. Thus static mode AFM is always done in contact where the overall force is repulsive. The force between the tip and the surface is kept constant during scanning by adjusting the tip-sample distance using a feedback mechanism to maintain a constant deflection. The feedback signal enables analysis of surface topographic information. However, if the stress under the AFM tip is very large and the sample surface is very soft, such as the case for the surface of a polymer or adsorbed biomolecules, the contact force may be sufficient to damage the sample. Tapping mode solves this problem.[126] In tapping mode operation (Figure 1.14b),[127] the cantilever oscillates close to its resonance frequency at ca. 300 kHz, and the tip contacts the surface intermediately to minimize the damage to soft samples. The amplitude of oscillation is typically a few nanometers. The van der Waals forces, which are strongest from 1 nm to 10 nm above the surface, or any other long range force which extends above the surface, act to decrease the resonance frequency of the cantilever. This decrease in resonant frequency combined with the feedback loop system maintains a constant oscillation amplitude or frequency by adjusting the average tip-to-sample distance. Measuring the tip-to-sample distance allows the scanning software to construct a topographic image of the sample surface.

(a)

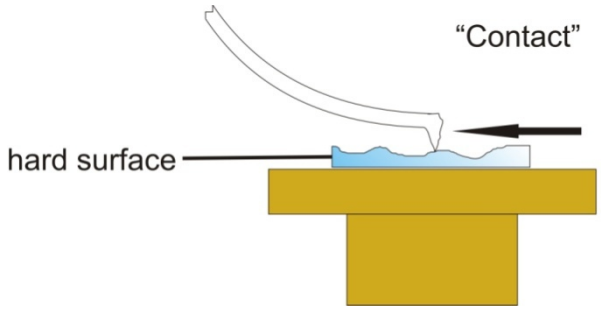

(b)

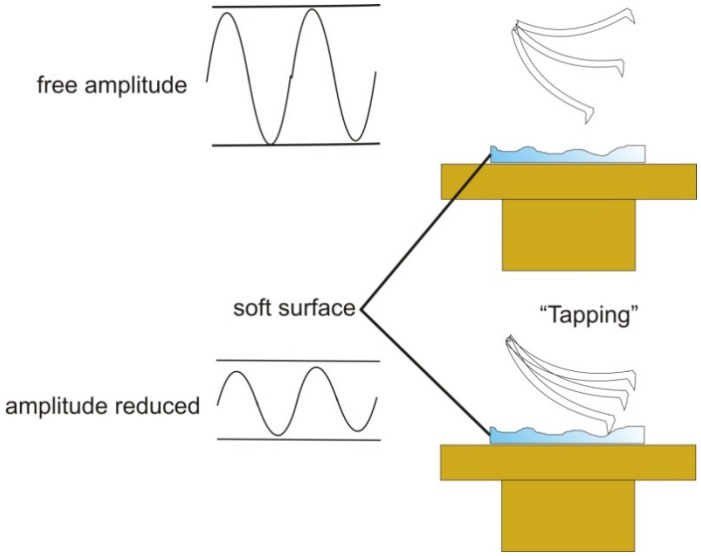

Figure 1.14 Schematic illustration of the working mechanism of (a) contact (static) mode AFM and (b) tapping (dynamic) mode AFM.

1.5.4 X-ray Photoelectron Spectroscopy

X-ray photoelectron spectroscopy (XPS) is a quantitative spectroscopic technique that can be used to analyze the surface chemistry of a material such as its elemental composition and chemical structure.[128] The sample is irradiated with X-ray photons generated by bombarding a metal anode with electrons. The X-rays penetrate deep into the solid, causing the ejection of core shell electrons. However, inelastic scattering effects mean that these electrons can only escape from the top 10 nm of material. The detector collects the ejected electrons and analyzes their kinetic energies, from which

the binding energies of the orbitals from which they are emitted may be determined. Because the binding energy for each element is specific, a characteristic set of XPS peaks at certain binding energy values can be produced to directly identify each element that exists in the surface of the material being analyzed. Thus XPS spectra can give us the surface composition of a material.[129] Besides, the binding energies are subject to small "chemical shifts", determined by their binding environment; analysis of these chemical shifts enables information about bonding to be determined from spectra. The binding energy of emitted photons can be determined by an equation below which is based on the work of Ernest Rutherford (1914).[130]

$$Eb = hv - Ek - \Phi$$

Eb represents the binding energy of emitted photons; *hv* represents the energy of an X-ray with particular wavelength which is known; *Ek* is the kinetic energy of the electron measured by the instrument and *Φ* is the work function of the spectrometer.

Figure 1.15 illustrates the photoemission process. When an X-ray photon hits the sample surface, an electron from shell K is ejected from the atom and will be detected by the spectrometer later. X-rays can also cause emission from binding (valence orbitals) but with much lower intensity and energy.

The experiment is carried out in ultra-high vacuum (UHV) at about 10^{-9} mbar, which minimizes the sample contamination and prevent scattering/absorption of photoelectrons.[131]

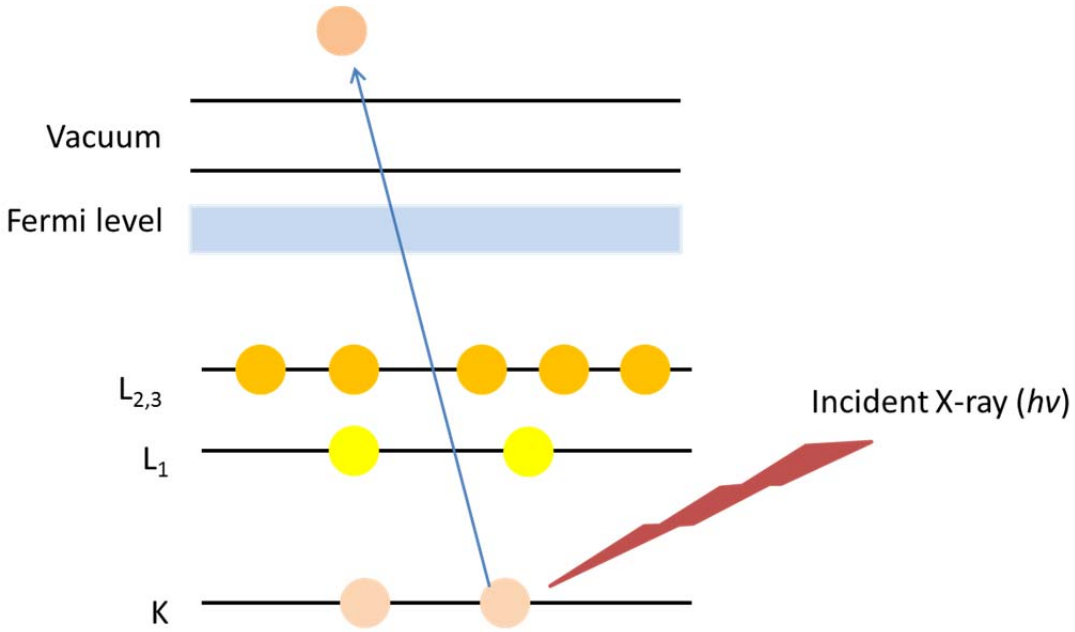

Figure 1.15 Schematic illustration of photoemission process and the relation to atomic band structure.

XPS analysis yields two kinds of spectra. The "survey spectrum" covers a wide range of binding energy and gives information about the chemical composition of the surface. The other is the "high resolution" spectrum, which covers a small range of binding energy but shows the detailed lineshape that enables the determination of chemical shifts. The observed lineshape is the sum of contributions from each binding environment of the element concerned. By peak fitting, these contributions may be determined and information obtained about the chemical structure. For example, the binding energy (BE) of C1s is 285 eV, but when it bonds to some other elements like oxygen or nitrogen, the peak will shift to higher binding energy because they are more electronegative elements.[132] Thus from the small shifts in binding energy, we could determine information about chemical structure.

The accurate calibration of XPS instrument has been important for valid analytical measurements.[133] Because the oxidation state of an element is identified by the small energy shift from the corresponding peak of the pure element in the spectrum, an error

of less than 0.5 eV in the bonding energy scale can lead to qualitative errors. The bonding energy tabulations of copper, silver and gold have been used for energy calibration because they have the advantages of being easily cleaned, chemical inert and stable conductors. To avoid errors arising from the work function differences between spectrometers, binding energies are most accurately defined by referencing the zero to the Fermi level of conducting samples. The *d*-bands of palladium and nickel with intense and sharp Fermi edges are usually used to define this zero. Binding energies of copper, silver and gold referenced to nickel Fermi edge using Al $K\alpha$ and Mg $K\alpha$ as the source radiations are listed in Table 1.2.

Table 1.2 XPS calibration binding energies, eV (Ni Fermi edge zero)

	Al $K\alpha$	**Mg $K\alpha$**
Cu 3*p*	75.14 ± 0.02	75.13 ± 0.02
Au $4f_{7/2}$	83.98 ± 0.02	84.00 ± 0.01
Ag $3d_{5/2}$	368.27 ± 0.02	368.29 ± 0.01
Cu L_3MM	567.97 ± 0.02	334.95 ± 0.01
Cu $2p_{3/2}$	932.67 ± 0.02	932.67 ± 0.02
Ag M_4NN	1128.79 ± 0.02	895.76 ± 0.02

In order to quantify spectra from XPS, peak intensities (peak areas) should be converted to atomic concentrations.[134] There are several factors to be considered, which are either sample-related factors or spectrometer-related factors. Sample related factors include the cross-section for emission and the escape depth of the electron emitted from the atom. For XPS measurement, the cross-section for photoelectron emission from a given orbital increases with atomic number for a given series of core levels, such as 1s, 2p, etc, and the escape depth of the electron emitted from the atom depends on its kinetic energy and the nature of the sample. Spectrometer related factors include the transmission function of the spectrometer, the efficiency of the detector and the effects of stray magnetic fields. When assuming the samples are homogeneous, the intensity (I) of a

photoelectron peak can be given in a simplified form as below.

$$I = J\rho\sigma K\lambda$$

Where J is the X-ray flux, ρ is the concentration of the atom or ion on the samples, σ is the cross-section for photoelectron emission, K covers all the spectrometer related factors and λ is the electron attenuation length.

The above equation can be used for direct quantification but usually experimentally determined sensitivity factors (F) will be employed. F includes the terms σ, K and λ as well as some additional features of photoelectron spectrum. Once the peak areas of the detected elements have been calculated, the intensity (I) could be determined. If the X-ray flux (J) remains constant during the experiment, the atomic percentage ($A\%$) could be deduced in the equation below.

$$A\% = \left\{ \frac{\frac{Ia}{Fa}}{\sum\left(\frac{I}{F}\right)} \right\} * 100\%$$

Where the atomic percentage ($A\%$) is determined by dividing the peak area by the sensitivity factors (F) and expressed as a fraction of the sum of all normalized intensities.

1.5.5 Confocal Laser Scanning Microscopy

In confocal laser scanning microscopy a laser beam reflected by multiple mirrors or a lens (typically 2 or 3 scanning linearly along the x and y axis) is used to scan the sample and generate an image through a fixed pinhole and detector. The concept of confocal imaging was developed by Marvin Minsky.[135] He developed a point-by-point image construction method by focusing a point of light sequentially across a specimen and then collecting some of the returning rays. For the process of fluorescence, it is known

that when light is incident on a dye molecule it may be absorbed and a photon may be emitted with a different wavelength. When fluorescent the dye molecule is raised to an excited energy state by absorbing a high-energy photon, it may lose energy to other molecules via collisional processes or by intersystem crossing and drop to a lower excited state. Relaxation from this state occurs via emission of a photon of lower energy (Figure 1.16).

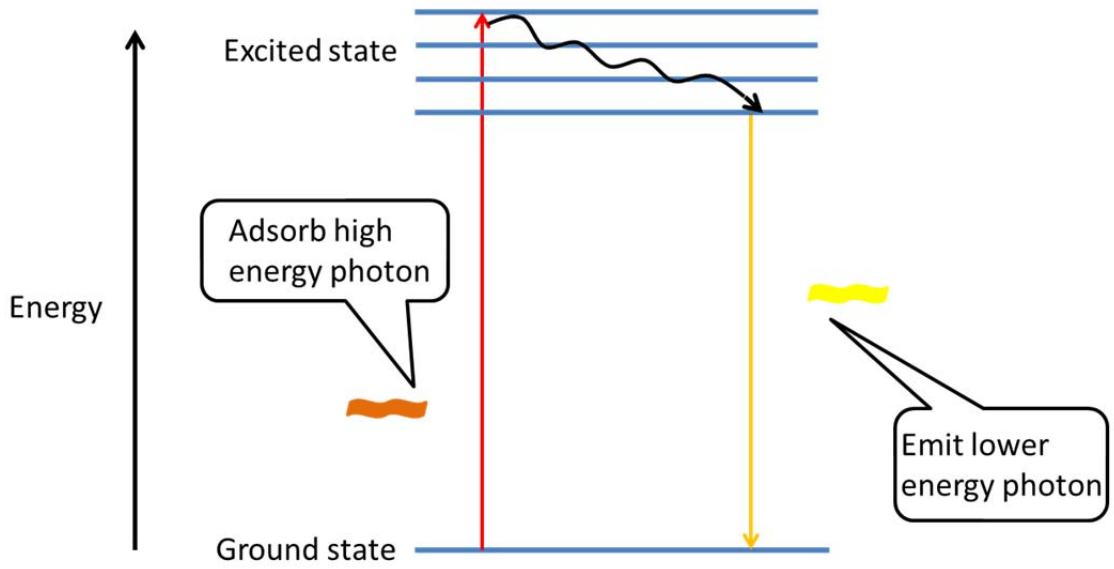

Figure 1.16 Schematic description of the fluorescence mechanism.

The microscope uses a dichroic mirror that reflects light shorter than a certain wavelength but transmits light of longer wavelength. Thus, the light from the laser source with short wavelength is reflected off and passes through the objective to the sample, while the longer-wavelength light from the fluorescing samples will pass through both the objective and the dichroic mirror to the eye-piece. This technique uses point illumination and a spatial pinhole to eliminate out-of-focus light from samples that are thicker than the focal plane. It enables the reconstruction of three-dimensional structures from the obtained images (Figure 1.17).[136,137]

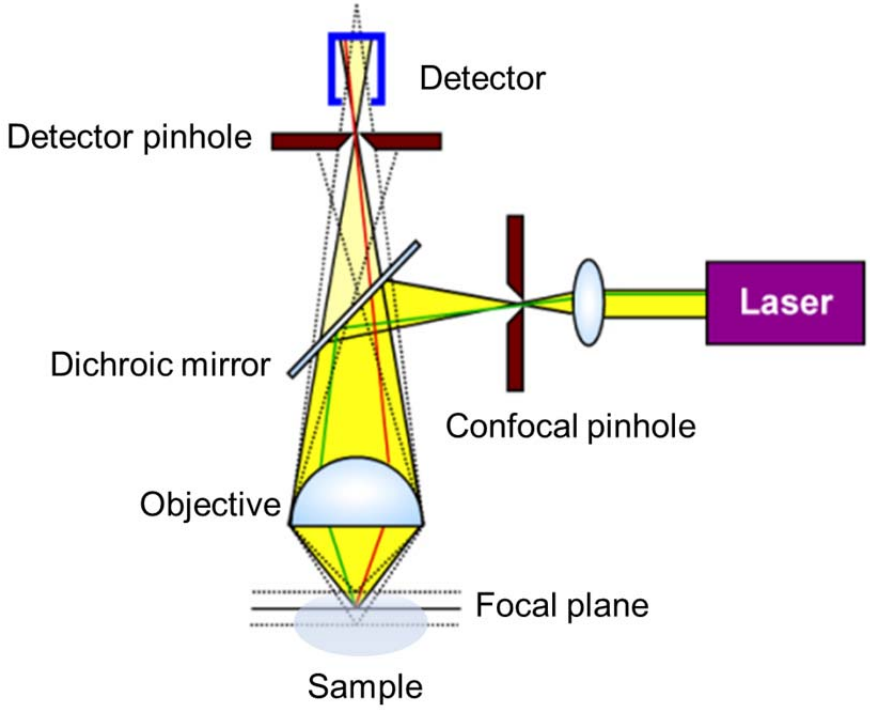

Figure 1.17 Schematic optical layout of confocal laser scanning microscopy.[137]

1.5.6 Scanning Near Field Optical Microscopy

In conventional optical microscopy, the resolution of the system is given by Rayleigh's equation[82,97]

$$d = 0.61\left(\frac{\lambda_0}{n\sin\theta}\right)$$

Where d is the minimum resolution, the distance from the highest intensity point to the first node of intensity; λ_0 is the wavelength of light used in vacuum; n is the refractive index and θ is the light convergence angle, $n\sin\theta$ can be taken as the numerical aperture as high as 1.3 or 1.4 for modern objectives. The resolution can be regarded as approximately $\lambda_0/2$. The implication of this is that the optical resolution in a microscope depends on the wavelength of the light we used. For visible light with wavelength between 400nm and 600nm, the average resolution is 200nm to 300nm.

Several methods have been used to improve the resolution of optical system. One approach is to use radiation with short wavelength, as in the X-ray microscope (wavelength 10~0.1nm) and the electron microscope (wavelength 0.14nm). However, for these techniques using electronic beams, the resolution is limited by scattering which yields a plume of excitation larger in size than $\lambda_0/2$. Another approach is to use near field methods. Diffraction has always been regarded as the main limitation on the resolution of far field optical methods of characterization. When a sample is held close enough to a nanoscopic aperture, light is diffracted after passing through the aperture resulting in the propagating waves in the far field. However, the evanescent near field ($d < \lambda_0$) will decay rapidly with distance from aperture, and is not subject to diffraction effects (Figure 1.18).[82,97] Synge realized that the near field can be used in microscopes between the late 1920s and early 1930s.[110,111] His idea was to use an opaque screen with a nanometric aperture. By bringing a sample very close to the aperture and scanning it beneath, he thought it would be possible to get high resolution optical images. For technical difficulties, his hypothesis was not experimentally proven until 1972 when Ash and Nicholls demonstrated sub-diffraction-limit measurement.[112,113]

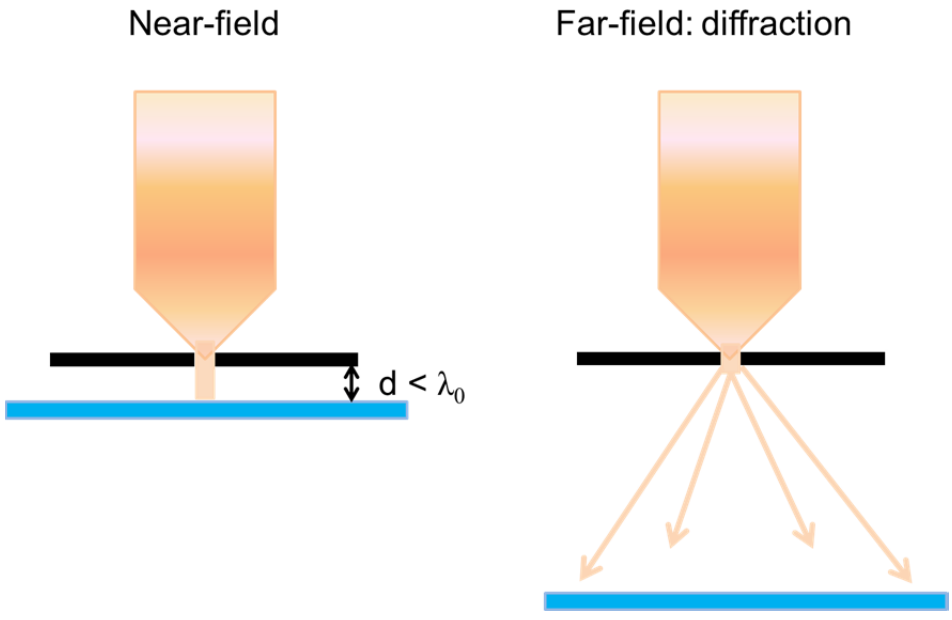

Figure 1.18 Schematic showing the near field (left) and far field (right). Near field waves interact non-diffractively with the aperture.[97]

Scanning near field optical microscopy (SNOM) was first introduced by Dieter Pohl[113] at IBM Zurich in 1984 and then developed by Betzig and Trautman[98] in 1992. Their instruments were based around an optical fiber probe with a sharp tip, which has a nanoscopic aperture at its apex and could be controlled by shear-force modulation. A laser beam is focused onto the back of the aperture, and the sample interacts with the near field at the front of the aperture. A tuning fork is usually connected to the fiber probe. When the probe approaches the surface, the oscillations of the tuning fork decrease. The shear force can be determined by a piezoelectric detector through the slight change of tuning fork motions. By using the shear-force feedback mechanism, it is possible to keep the probe within 5-15 nm of the surface in order to acquire near field images. However, SNOM has failed to become a widely used characterization tool because of the difficulties associated with acquisition of images. As shown in Figure 1.19, a fixed position detector cannot collect all the scattered light emitted from the sample. Even if using the probe to acquire signal, most light may be lost in the fibre.

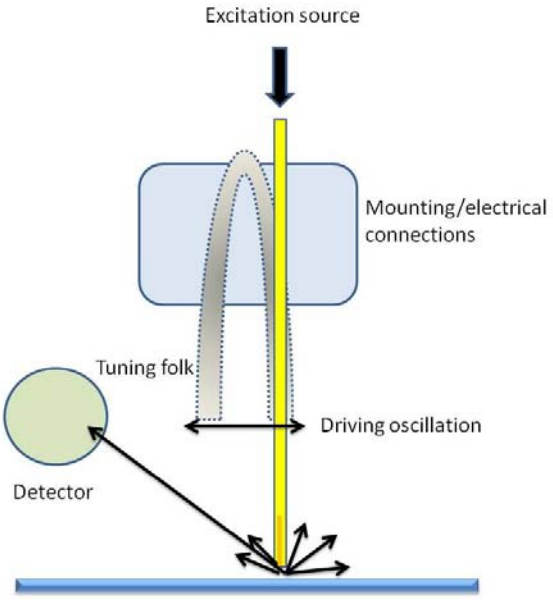

Figure 1.19 Schematic illustration of a shear-force mode SNOM system.

1.6 Summary of Micro and Nanofabrication Techniques for Protein Patterning

1.6.1 Mask-based UV Lithography

Monolayers of a photolabile chemical may be prepared on a substrate and selectively illuminated by UV light through a mask in order to modify the photolabile groups on the surfaces. Exposed regions can be functionalized by chemical reactions and further derivatisations like protein attachment can be carried out. Figure 1.20 shows a process that can be used to make micron-scale patterns of proteins through mask-based UV lithography. Ducker et al.[67] used this technique to prepare some micron-scale patterns of streptavidin on the OEG-terminated SAMs. Alang Ahmad et al.[68] deprotected 2-nitrophenylethoxycarbonyl (NPEOC) modified aminosilane surfaces by mask-based UV lithography and produced the micron-scale patterns of NeutrAvidin particles.

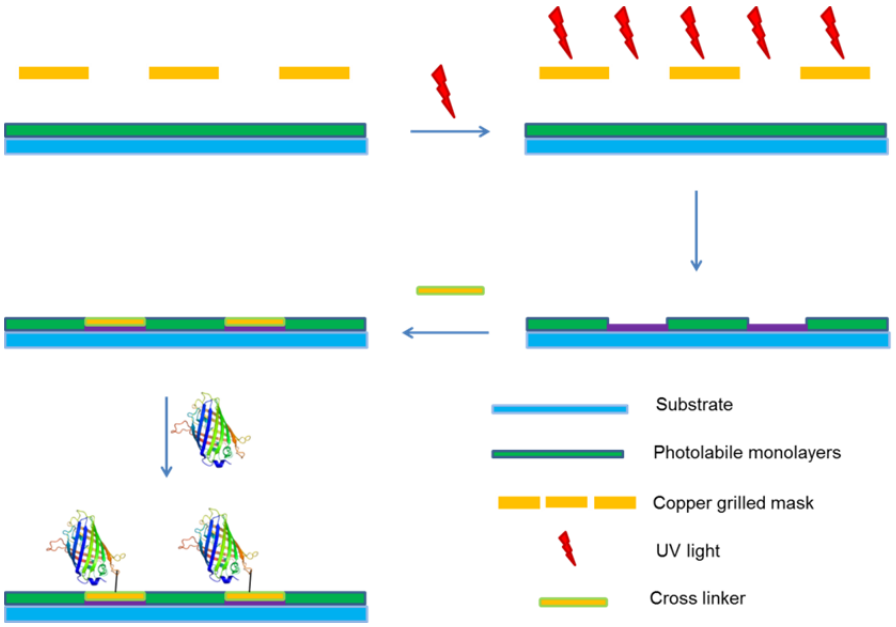

Figure 1.20 Schematic illustration of the process to prepare micron-scale patterns of proteins through mask-based UV lithography.

1.6.2 Micro-Contact Printing

In micro-contact printing, a poly (dimethylsiloxane) (PDMS) stamp is used to "ink" a substrate with suitable chemicals, which are transferred to the substrate in a contact process.[69-71] For example, after a PDMS stamp was inked with an alkyl thiol, it may be

pressed onto the gold surface leading to the transfer of a monomolecular layer of thiol to the gold surface by the protruding regions of the stamp (Figure 1.21). Different "inks" can be used to functionalize different surfaces. Chien Ching Wu et al.[72] prepared NTA-terminated SAMs on glass substrates and then used metal ions (Ni^{2+}) as ink to print micron-scale patterns of Ni^{2+} on the surface. Protein patterns with micron-scale size would be formed after site-specific attachment of proteins through the NTA-Ni^{2+}-His-Tag system. Juergen Groll et al.[73] prepared star PEG layers with amino-reactive isocyanate groups on a silicon substrate and then they used amino functional NTA molecules as an ink to produce patterns of covalently bond NTA through the chemical reaction in the "ink" area.[74] His-tagged proteins could be selectively bound to the NTA patterns and the unmodified PEG regions would prevent nonspecific protein adsorption.

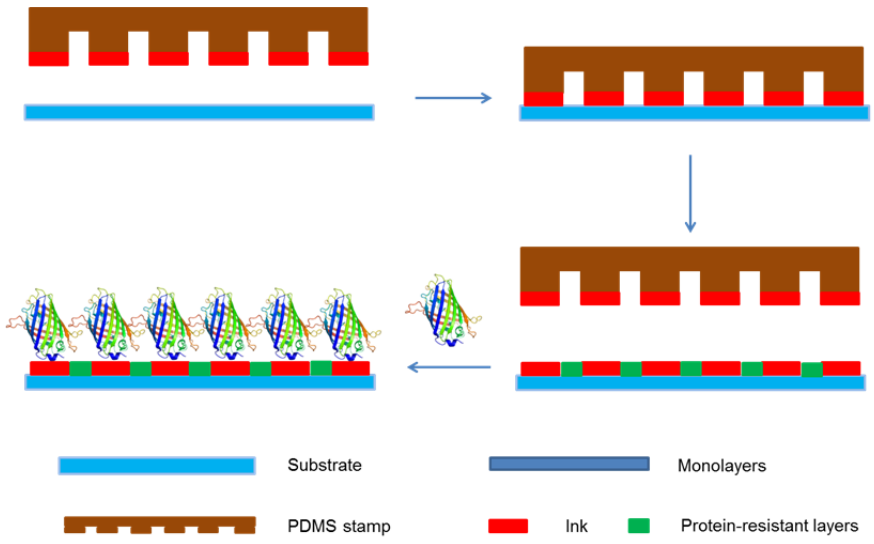

Figure 1.21 Schematic illustration of the process to prepare micron-scale patterns of proteins through micro-contact printing.

1.6.3 Electron Beam (e-beam) Lithography

In electron beam (e-beam) lithography, a beam of electrons is scanned across a surface covered with a film of resist, leading to selective removal of either exposed or non-exposed regions of the resist. Very small structures can be created in the resist film,

which can be transferred subsequently to the substrate material, often by etching. Because the wavelength of electrons is very small, e-beam lithography beats the diffraction limit for light and enables the fabrication of features in the nanoscale region without the use of a mask. This technique can not only generate arbitrary protein patterns of various shapes and sizes but it can also control interfeature spaces and locations precisely. Christman et al. [75] used an electron beam as a tool to position multiple proteins at the nanoscale. At first they prepared PEG polymer layers on silicon substrate as the resist film by spin-coating. When the PEG film was exposed to the focused e-beams, it underwent cross-linking both to itself and to a silicon surface. They used this e-beam lithographic system to produce several desired PEG patterns. When regions of the PEG polymers were sequentially functionalised with four protein-reactive handles (biotin, maleimide, aminooxy, or NTA), they could be used to position different proteins on the surface through the resulting specific interactions to produce multi-protein patterns. Turchanin et al. [76] first prepared 4'-nitro-1, 1'-biphenyl-4-thiol (NBPT) SAMs on a gold surface, on which patterns were created by using e-beam lithography to reduce the terminal nitro groups into amino groups and to cross-link the underlying aromatic substrate. Then multivalent tris-NTA chelator with protected carboxyl functionality was grafted onto the amino area and deprotected to form carboxyl groups which could chelate with Ni^{2+}. The unexposed regions of NBPT SAMs were exchanged with protein-repellent 16-mercaptohexadecanoic acid (triethylene glycol) ester (EG_3-OH thiols). Finally, His_{10}-tagged maltose binding protein (At_{565}MBP-His_{10}) was immobilized specifically on the chip through NTA-Ni^{2+}-His-tagged system (Figure 1.22).

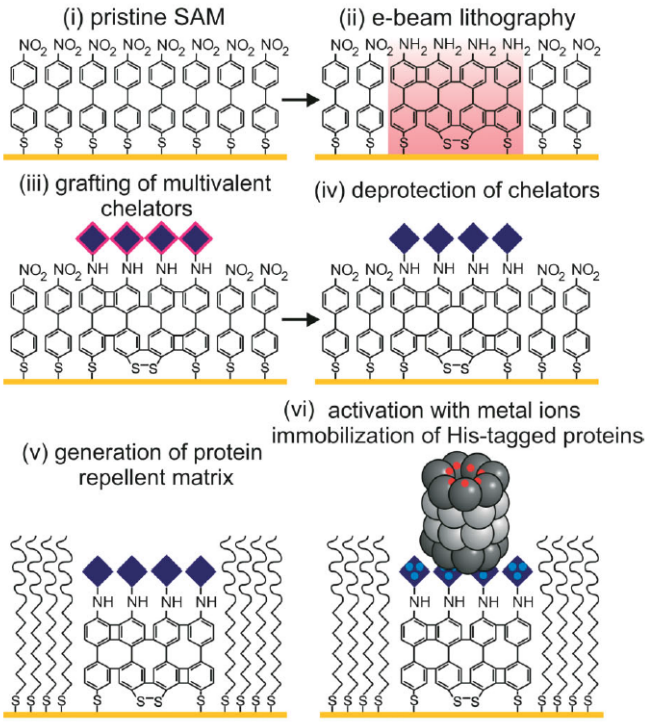

Figure 1.22 Schematic representation of surface patterning by e-beam lithography and controlled immobilization of His-tagged protein complexes.[76]

1.6.4 Nanoimprint Lithography

Nanoimprint lithography (NIL) is method based on mechanical pattern formation which achieves nanoscale resolution (to ca. 10nm) over large areas. A silicon template which is fabricated by e-beam lithography is usually used as the stamp to press against the substrate, leaving an imprint of the template features in a film of resist. The patterned substrate is then developed and functionalized to attach proteins. Hoff et al. [77] prepared poly (methyl methacrylate) (PMMA) films on silicon and glass substrates. A substrate was brought into physical contact with the stamp at 175°C under a pressure of 5000kPa for 5 min before cooling to room temperature. After the stamp was separated from the substrate, O_2 reactive ion etching (RIE) was used to remove PMMA residual in the patterned regions and a thin passivating layer of CFx polymer was deposited at this area. The remaining PMMA was stripped away with acetone, leaving an exposed silicon dioxide surface. The oxide pattern reacted with aminopropyldimethylethoxysilane

(APDMES) to become covered with a monolayer. Then biotin-succinimidyl ester was covalently bound to the exposed primary amine tail group of the patterned APDMES. Streptavidin and biotinylated proteins could be bound to the patterns sequentially (Figure 1.23). Escalante et al.[78] used NIL to pattern discrete regions of fluoro-terminated or PEG SAMs and amines onto a glass substrate in a similar way to Hoff. They assembled the photosynthetic membrane proteins LH1 and LH2 directly onto chemically patterned surfaces through electrostatic interactions and confirmed that the proteins exhibited optical spectra similar to those measured in the solution phase.

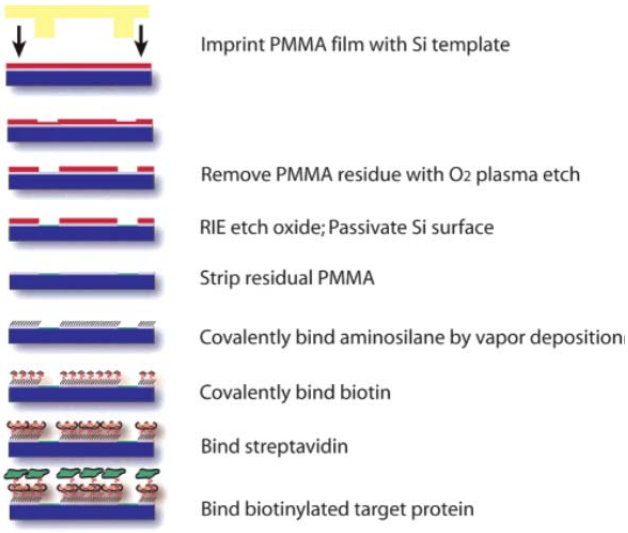

Figure 1.23 Diagram of imprint substrate patterning and protein immobilization process.[77]

1.6.5 Interference Lithography

Interference lithography (IL) is an ideal technique to produce large area, defect-free nanostructures. It is based on the interaction between two or more coherent light sources. Figure 1.24 shows a schematic diagram of a two-beam interferometer. UV light from the laser source is split into two beams; one of these is reflected by the mirror onto the sample's surface and the other interacts with the sample directly, where it interferes with the other beam. The interferogram consists of alternating bands of constructive and destructive interference with a sinusoidal cross-section and a period $\lambda/2n\sin\theta$.[79] If the

substrate is coated with photolabile chemicals, a pattern will be formed as a result of exposure to the interferogram, leading to spatially periodic regions of exposure with nanoscale amine sites. Tsargorodska et al.[80] fabricated reusable, robust gold nanostructures over macroscopic (cm^2) areas by interference lithography of self-assembled monolayers. They prepared SAMs of alkylthiolates on chromium-primed polycrystalline gold films and created IL patterns on SAMs using a Lloyd's mirror interferometer. The sample was then etched using mercaptoethylamine in ethanol in a rapid process resulting in gold nanostructures, which could be used as substrates to form protein patterns. Adams et al.[81] prepared large-area nanoscale patterns on alkanethiolates SAMs by interferometric lithography. They exposed the OEG-terminated SAMs to photodegrade and introduce the aldehyde groups to attach proteins. Nanostructured assemblies of streptavidin followed by biotinylated IgG were formed on the gold substrates.

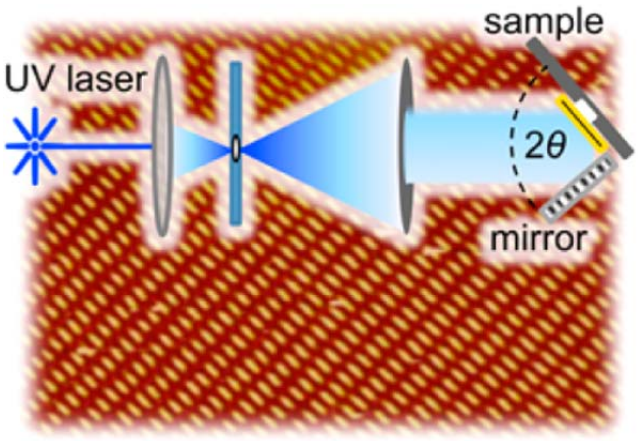

Figure 1.24 Schematic illustration of the setup of two beams IL and gold nanostructures fabricated by it.[80]

1.6.6 Scanning Probe Lithography

Scanning probe lithography has been used widely in molecular patterning. Generally speaking, it is a technique relying on a physical process involving deposition or removal of materials.[82] There are several different techniques based on scanning probe lithography (Figure 1.25).

1.6.6.1 Dip-Pen Nanolithography

Dip-pen nanolithography (DPN) was first reported by Mirkin et al. in 1999.[83-86] They found that the water meniscus formed between an AFM tip and a surface by capillary condensation could be used to transfer molecules from tip to surface (Figure 1.25a). The AFM tip is a "pen" while a solution of molecular adsorbate is the ink. Initially, the ink was a thiol but later a wide range of complex molecules such as conducting polymers and biological molecules such as proteins and DNA has been used.[87,88] After the ink is deposited onto the AFM tip, the tip is brought into contact with surface as if imaging the surface in contact mode. Ink material is then transferred onto the surface via the meniscus. By controlling the scan rate, contact time, humidity and other parameters, it is possible to create features smaller than 100 nm in size.[88,89] In addition, the roughness of the surface may have an effect on the lithography, constraining the choice of substrate somewhat and meaning that only solid substrates like gold or silicon with smooth surfaces could be used. Hyun et al.[90] reported their fabrication of protein nanostructures by DPN. They used 16-mercaptohexadecanoic acid (MHA) as ink and patterned it on a gold substrate by DPN. The unpatterned regions were passivated with protein-resistant OEG-terminated alkanethiol SAMs, after which biotin-NH_2 and streptavidin were coupled to the terminal COOH groups in the MHA SAMs. Finally biotinylated proteins were immobilized onto the nanostructures through molecular recognition between biotin and streptavidin. Irvine et al.[91] fabricated protein immunoassay arrays on nitrocellulose using DPN. A capture antibody was used as the ink and delivered to nitrocellulose slides to generate spot arrays by DPN. Then a prostate specific antigen was applied to the arrays to form protein immunoassay arrays.

1.6.6.2 Nanoshaving or nanografting

Nanoshaving or nanografting is a technique that uses a probe to remove the adsorbates from selected areas of a complete surface layer (Figure 1.25b). A number of works have demonstrated the removal of alkylthiols from SAMs on gold surfaces.[92-95] AFM is used to exert a force on the tip which is significantly higher (ca. 5.2 nN) than the normal

imaging force (ca. 0.03 nN) in order to displace the surface bound adsorbate. If the displacement is carried out under a solvent containing the desired adsorbate for example, a second alkanethiol, a chemical pattern will be formed. Other examples of mechanical removal of adsorbates from different surfaces have been reported recently. EI Zubir et al.[96] used nanoshaving to fabricate nanostructures in SAMs of alkylphosphonates adsorbed at aluminium oxide surfaces. They selectively removed aryl azide-terminated alkylphosphonates from the aluminium oxide surface using an AFM probe, and adsorbed aminobutylphosphonic acid into the nanoscale exposed areas. Then they attached polyethylene glycol onto the unmodified regions in a photochemical coupling reaction in order to create a protein-resistant surface and deposited NeutrAvidin onto the nanostructures. Under optimum conditions they could fabricate structures as narrow as 39 nm.

1.6.6.3 Scanning Near Field Photolithography

Scanning near-field photolithography (SNP) is an optical approach for nanopatterning, which uses a scanning near field optical microscope (SNOM) to carry out lithography.[97] Although SNOM has failed to become a widely used tool for nanoscale characterisation because of the difficulties associated with image acquisition, it has proved to be an efficient instrument to carry out lithography. An aperture-based SNOM system can provide a very small light source in the form of a fibre-based probe, which can be used to selectively illuminate nanoscale regions of a surface (Figure 1.25c). The shear-force feedback system in an optical fibre SNOM is convenient to use and reliable. Early approaches to this technique include the work done by Betzig et al.,[98] who used a shear force SNOM system to irradiate certain regions of Co/Pt multilayer in order to reverse the magnetic polarization of the material, leading to the formation of domains of approximately 60nm. Recently many works related to this technique have been done in the author's laboratory to fabricate nanoscale structures of biomolecules.[67,99-102] For example, Sun et al. [103] used SNP to pattern alkanethiol monolayers by photochemical conversion of alkylthiolates to alkylsulfonates and replacement of the oxidation products by other contrasting adsorbates. Further derivatization of proteins could be

carried out on them. The best resolution achieved was 9nm, comparable with the size of many biomolecules. Reynolds et al. [104] used SNP to fabricate nanostructures on an OEG-terminated siloxane film. UV exposure caused the photodegradation of OEG groups and introduced aldehyde groups, to which NTA was coupled and then his-tagged proteins were attached via NTA-Ni^{2+}-His-Tag system. Ahmad et al. [68] prepared SAMs of an aminosilane protected by oligo (ethylene glycol)-derivatised nitrophenylethoxycarbonyl (OEG-NPEOC), which would undergo a photocleavage when exposed to UV laser and render protein-resistant by the presence of the oligo (ethylene glycol) chains. Nanometer-scale patterns were fabricated using SNP to selectively deprotect OEG-NPEOC-aminosiloxane on the substrates. Then the resulting amine terminated area could be derivatized by protein linkages and then proteins. Through this method, nanopatterns with a resolution of 150 nm were achieved.

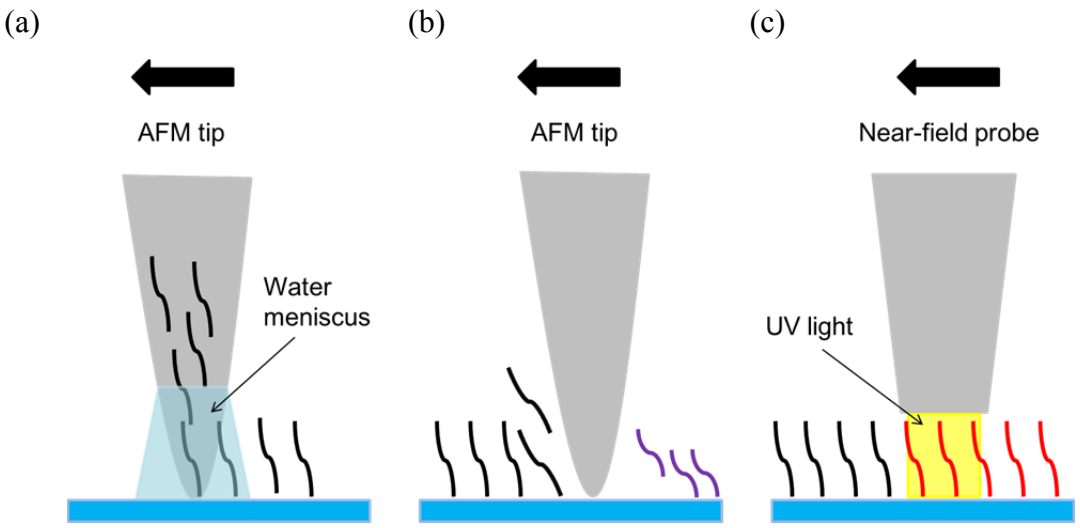

Figure 1.25 Schematic illustrations of different approaches to scanning probe lithography. (a) Dip-pen lithography; (b) nanoshaving or nanografting; (c) scanning near field photolithography.

1.7 Photosynthesis and Low-Dimensional Chemistry

Photosynthesis is the process by which plants and other organisms use solar energy to drive a cascade of electron transfer leading to the formation of NADPH and ATP, which

then drive the production of carbohydrate. In plants and bacteria, several proteins embedded in a specialised membrane are involved in these energetic reactions. Those membrane proteins can mediate the energy interconversion, store the solar energy in a chemical form as ATP, control the movement of chemicals and transduce signals. Plants and bacteria harvest solar energy with remarkable efficiency, which is the basis for life. To benefit from biology, we need to know how those natural systems work and then learn from them to develop new technologies in order to solve the practical problem of the scarcity of energy supply.

Figure 1.26 shows the chromatophore vesicle from R. sphaeroides (a), which contains the bacterial photosynthetic apparatus, and the mechanism of bacterial photosynthesis (b). Light is captured by light-harvesting complex 2 (LH2) and the energy funnelled to a special chlorophyll-protein complex consisting of light-harvesting complex 1 (LH1) and the photosynthetic reaction centre (RC). The LH1-RC complex contains a metal complex at its heart where ubiquinone (Q) is converted to ubiquinol (QH_2). QH_2 diffuses through the membrane to membrane-bound cytochrome bc_1 complexes, which oxidise QH_2 to Q. During the QH_2 – Q redox cycle, cytochrome bc_1 complexes pump protons across the membrane, leading to a transmembrane proton gradient which drives proton transfer back through ATP synthase, driving the conversion of ADP to ATP.

(a)

(b)

(c)

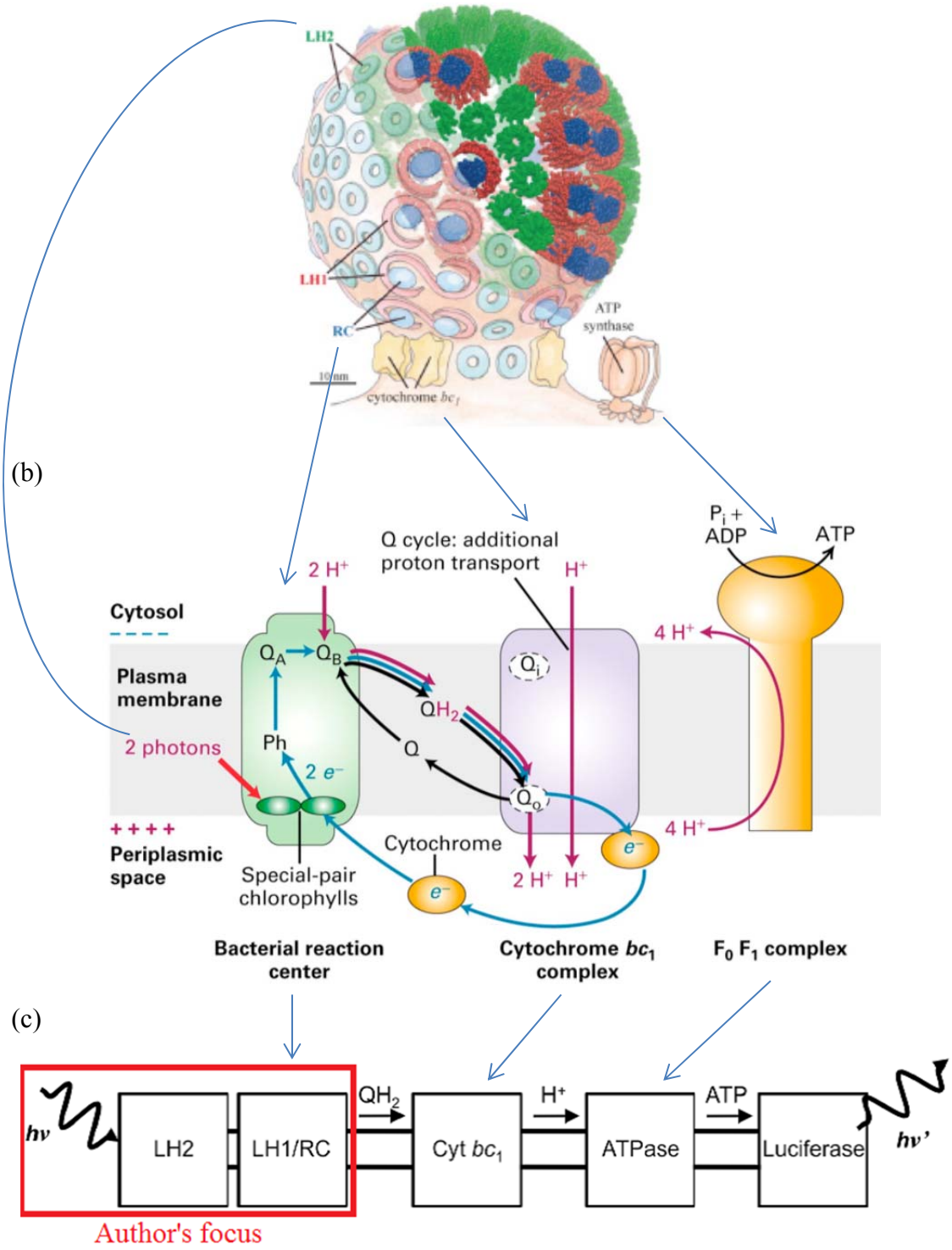

Figure 1.26 (a) The chromatophore vesicle containing the bacterial photosynthetic apparatus from Rhodobacter sphaeroides[105]. (b) The mechanism of bacterial photosynthesis[106]. (c) A low-dimensional system that replicates the bacterial photosynthetic apparatus.

In physics, low-dimensional structures are defined to be ones with highly constrained lengths in two or more dimensions. In many senses, the chromatophore vesicle even all biomolecules may be considered to be low-dimensional. Our ambition is to construct a low-dimensional system that replicates the bacterial photosynthetic apparatus on a chip as shown in Figure 1.26 (c). When irradiated by light, LH2 would transfer the excitation energy through LH1 to RC. QH_2 could be generated during the process and migrate to cytochrome bc_1 by itself, where it would be oxidised back to Q. Concomitantly photons would be pumped across a membrane from the photon-accumulated reservoir to a photon-permeable polymer film that connects with ATP synthase, where ADP could be converted to ATP. Luciferase would consume those ATP and emit luminescence. Each "corral" shown as the box below will be fabricated on the solid substrates from nanostructured polymer brushes. Channels which allow quinones, protons and ATP to diffuse will be built up to connect those "corrals".

1.8 Aims of this research

The big goal of our LDC programme is to develop a new field of research, Low-Dimensional Chemistry, which is the manipulation of chemical structure and bonding in a spatially selective fashion at the level of single molecules, the interfacing of molecules with functional elements and the assemble of components into systems. To achieve this goal, top-down (lithographic) methodology and bottom-up (synthetic) techniques are unified to yield control of molecular structure and function across the length scales, from molecular to the macroscopic. To replicate the functionality of the low-dimensional system, the fabrication of multiple-component systems remains the biggest challenge.

This thesis will focus on the research of methodology to fabricate multi-component structures. The aim is to achieve the biochips with multi-protein patterns with the size of nanometer scale, like the two protein patterns of LH1 and LH2. Chapter 3 will detail the optimized conditions to prepare the ideal silane SAMs on silica surfaces. Chapter 4 will

demonstrate how to fabricate single and multiple protein patterns on OEG-NPEOC-APTES SAMs. Based on the work of Chapter 4, Chapter 5 will show the study on the site-specific immobilization of His-tagged proteins on the NTA functional OEG-NPEOC-APTES surface. Chapter 6 will show a different method to prepare protein patterns on azide terminated surfaces.

Chapter 2 Experimental

2.1 Materials

Chemicals	Sources
(3-Aminopropyl) triethoxysilane (APTES) (99%)	Sigma-Aldrich (Poole, UK)
Sodium dodecyl sulfate (SDS)	Sigma-Aldrich (Poole, UK)
Sulfuric acid ((1.83 S.G. 95+ %)	Fisher Scientific (Loughborough, UK)
Hydrogen peroxide solution (100 volumes 30+ %)	Fisher Scientific (Loughborough, UK)
Ammonia solution (S. G. 0.88, 35%)	Fisher Scientific (Loughborough, UK)
Toluene (HPLC grade)	Fisher Scientific (Loughborough, UK)
Ethanol (absolute)	VWR international (Lutterworth, UK)
Silicon wafers (reclaimed, p-type, <100>)	Compart Technology (Tamworth, UK)
Glass cover slips (20 x 60 mm)	Menzel-Gläser (Braunschweig, Germany)
N-{2-[2-nitro-4-(2,5,8,11,14,17,20-heptaoxa docosan-22-yloxy)-phenyl]ethoxycarbonyl}-3-aminopropyltriethoxysilane (OEG-NPEOC-APTES)	AF ChemPharm Ltd
4-azido-3-(triethoxypropylsilane) benzamide (Acryl azide)	Paul Taylor (Department of Chemistry)
Glutaraldehyde solution (GA, Grade II, 50% in water)	VWR international (Lutterworth, UK)
N-(5-amino-1-carboxypentyl)iminodiacetic acid (ABNTA)	Dojindo Molecular Technologies (Munich, Germany)
HS-C_{11}-$(EG)_3$-NTA	Prochimia Surfaces (Sopot, Poland)
2, 2, 2-Trifluoroethylamine (95.5%)	Sigma-Aldrich (Poole, UK)
Octadecylamine (97%)	Sigma-Aldrich (Poole, UK)
Phosphate buffered saline (PBS) tablets	Sigma-Aldrich (Poole, UK)
Ammonium acetate	Sigma-Aldrich (Poole, UK)

HEPES buffer	Sigma-Aldrich (Poole, UK)
Histidine-tagged (his-tagged) proteins	Dr. Michael Cartron (Department of molecular biology and biotechnology)
Light-harvesting proteins	Dr. Michael Cartron (Department of molecular biology and biotechnology)
Immunoglobulin G (IgG)	Life Technologies
Streptavidin 750	Life Technologies
NeutrAvidin	Life Technologies
Streptavidin 425, 488 and 655	Sigma-Aldrich (Poole, UK)
Quartz slides (50mm x 25mm x 1mm)	Agar Scientific Limited (Stansted, UK)

2.2 Glassware and Substrate Cleaning

All the glassware used in the formation of SAMs was first cleaned with piranha solution, which is a mixture of 30% hydrogen peroxide and 95% concentrated sulfuric acid in the ratio of 3:7, and subsequently by immersion in the Radio Cooperative of America (RCA) cleaning solution, which is a mixture of water, 30% hydrogen peroxide and 35% ammonia solution in the ratio of 5:1:1. (Caution: piranha solution is an extremely strong oxidising agent which has been known to detonate spontaneously upon contact with organic material).

Glass slides, silicon wafers or quartz slides were cut to a suitable size using a diamond scribe such that they fitted into 25mL tubes with flat bottoms. Several tubes were placed in a large Pyrex beaker and were cleaned by filling with SDS water solution (ca. 0.1% v/v) and placing in a sonicator for 15 min. De-ionised water was used to rinse them 4 times. The tubes containing substrates were then immersed in piranha solution for 1 h and rinsed with water 7 times. Subsequently the tubes containing substrates were treated by filling with the RCA solution and maintained at boiling temperature for 30 min on a hot plate. Finally, the tubes were rinsed with de-ionised water 7 times and placed in an oven overnight to dry them.

2.3 Preparation of Self-Assembled Monolayers (SAMs)

Clean dry tubes containing substrates were removed from the oven and allowed to cool. Silane SAMs were prepared by immersing the substrates into a silane solution of the appropriate concentration in toluene. The silane solution was prepared by transferring 25 mL HPLC grade toluene into tubes with the appropriate amount of liquid silane. The tubes were sealed and sonicated to ensure mixing. The reaction was left on for a period from several minutes to days and then stopped by removing the silane solution. The substrates were rinsed using a 1:1 toluene : ethanol mixture at first and then ethanol several times. Nitrogen gas was used to dry the substrates. Finally, the substrates were annealed in a vacuum oven at 120°C for 1 h.

2.4 Protein attachment

XFP (GFP, YFP, CFP and Mcherry), Avidin (Streptavidin and Neutravidin) and IgG were either dissolved in 0.1 M PBS or 0.1 M ammonium acetate solution. Membrane proteins (LH1 and LH2) were dissolved in 20 mM HEPES solution with 0.03% (v/v) βDDM. All protein solutions were 10 μgmL^{-1} unless otherwise stated. The surfaces were immersed in protein solutions for periods ranging from several hours up to overnight dependent on the type of protein. Finally, the samples were rinsed with buffer and dried under a stream of nitrogen.

2.5 Photo-Patterning

2.5.1 Micron-scale UV Lithography

A Coherent Innova 300C frequency doubled argon ion laser system (wavelength of 244 nm) and a Kimmon He-Cd laser system (wavelength of 325 nm) were used to make micro-scale patterns on SAMs. The power output of the argon ion laser was varied from 1 to 100 mW while the power of the He-Cd laser was fixed to 11 mW. The UV laser beam was passed through several lenses, and finally reflected by a 45° mirror and focused onto the sample as a spot with diameter of 0.5 cm. A small round electron microscope grid with square patterns (1000 or 2000 mesh, Agar, Cambridge, UK) was used as mask placed in the center of sample and a bigger round quartz disk was used to

cover the whole mask and sample in case they may move during the exposure (Figure 2.1). Each sample was cut into small piece and put under the laser spot, which exposed the center of sample's surface through the mask at a certain exposure dose.

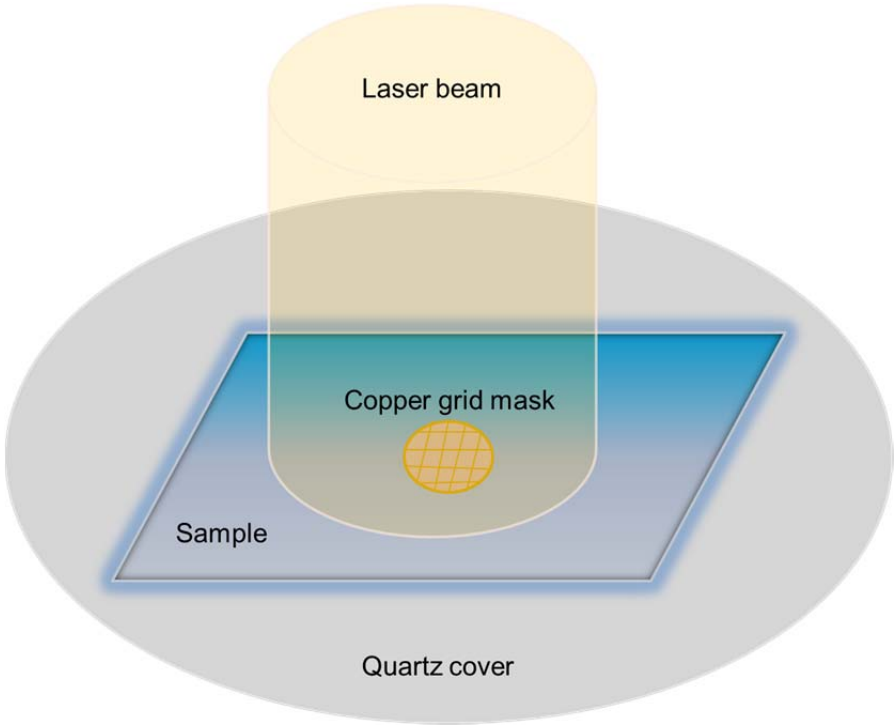

Figure 2.1 Schematic illustration of micron-scale UV lithography.

2.5.2 Interference Lithography

As introduced in chapter 1, interference lithography (IL) is an ideal technique to produce large area, defect-free nanostructures, which is based on the interaction between two or more coherent light sources.[107,108] Figure 2.2 illustrates the process schematically. In a Lloyd's mirror two-beam interferometer, a coherent laser beam coming from the laser source is aligned after passing through several lens, beam splitter and aperture (Figure 2.2a). A flat mirror is fixed perpendicular to the sample stage. Part of the laser beam is reflected by the mirror and directed onto the sample's surface, which would interfere with the undisturbed part of the laser beam on the sample's surface. The altered path length of photons in the reflected beam results in interference with the half of the beam that is incident directly on the sample, giving rise to an

interferogram consisting of alternating bands of constructive and destructive interference. Figure 2.2 (b) and (c) shows the constructive and destructive interference schematically. Red line represents half of the laser beam reflected by the mirror while blue line represents the undisturbed half. Orange line represents the sum of the interaction between the two beams, which is amplified in constructive interference but cancelled out in destructive interference.

(a)

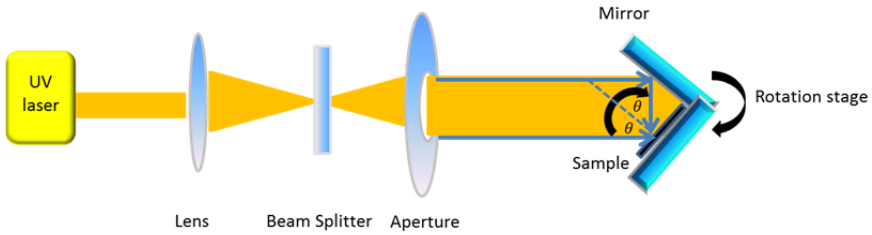

(b)

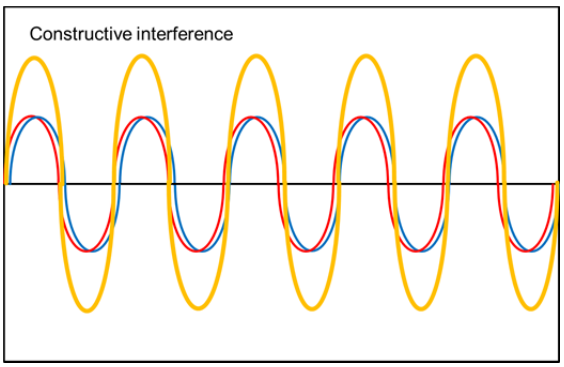

(c)

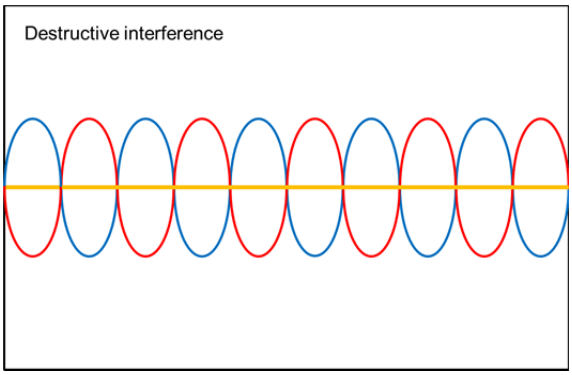

Figure 2.2 Schematic illustration for (a) the setup of Lloyd's mirror two-beam interferometer; (b) constructive interference and (c) destructive interference of two coherent beams.

Consider a sample's surface that is coated with a photosensitive medium, for example OEG-NPEOC-APTES. A pattern will be formed when two coherent beams constructively and destructively interfere at the sample surface resulting in spatially periodic regions of high and low intensity, which are recorded by photosensitive medium. The periodicity of the interference patterns Λ depends on the incident angle θ of the beam and the wavelength of the laser λ.[107,109]

$$\Lambda = \frac{\lambda}{2 \sin \theta}$$

In the present work, when the sample stage is rotated, the incident angle θ will be changed and the periodicity of patterns will be changed as well. For example, when we used the 244nm laser to prepare IL patterns, if incident angle $\theta = 10^{o}$, the periodicity of interference patterns Λ = 703nm; if $\theta = 20^{o}$, Λ = 357nm; and if $\theta = 30^{o}$, Λ = 244nm.

2.5.3 Scanning near field photolithography

Aperture-based SNOM system could provide a very small light source through its fiber-based probes, and thus it should be possible to carry out lithography with it. In our experiment, scanning near field photolithography (SNP) was carried out by a near field probe using SNOM system. The near field probes used in the present work are similar to conventional AFM probes with the exception that they have hollow pyramidal tips with apertures formed at their apices as shown in Figure 2.3(a). Those commercial UV probes come from WITec (WITec focus innovations) with apertures of ca. 100nm as seen in small image in the right head side of Figure 2.3(a). As shown in experimental setup scheme (Figure 2.3b), light from the 325nm excitation excited laser was transferred through an optical fiber and focused onto the near field probe through an objective. The excitation laser passed through the aperture to the tip of the near field probe and was focused onto its backside. Interaction between the surface and tip was monitored by an optical lever detection system, in which a feedback laser spot was

reflected off the cantilever of the probe and onto the segmented photodiode. When the probe approached close to the surface, there was a change of interaction resulting in a change in the deflection of the feedback laser. When the system detected the change, it would maintain a pre-set interaction force between the tip and surface. The near-field excitation was used to modify a photosensitive layer like the OEG-NPEOC-APTES films. The WitecSNOM software was used to control the speed and movement of the probe and to program its movements to make different structures lithographically.

(a)

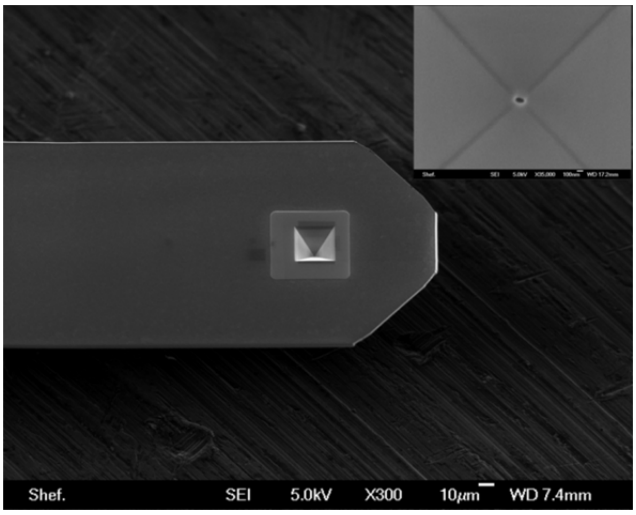

(b)

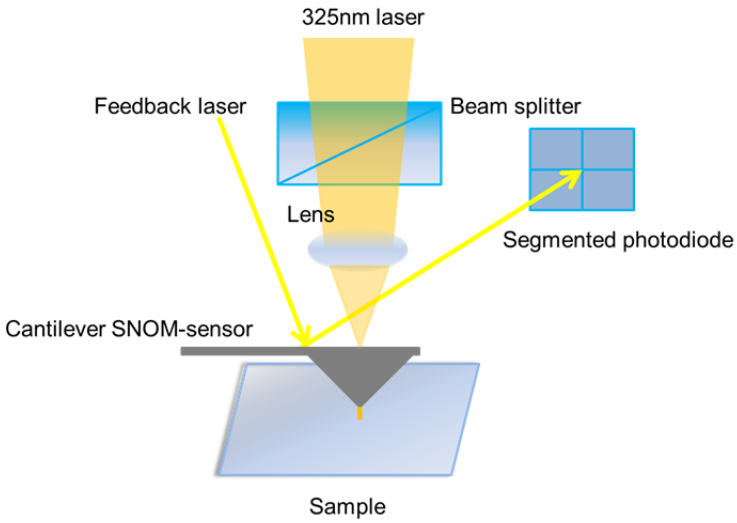

Figure 2.3 (a) SEM image of a SNOM probe. The insert shows a micrograph of the tip at higher magnification. (b) Schematic diagram showing the operation of a cantilever based SNOM system.

2.6 Surface analysis

2.6.1 Contact angle

Contact angles were measured using a Rame-Hart goniometer by the static sessile drop method. A water droplet was placed onto the surface of a solid substrate and the angle formed between the liquid/solid interface and the liquid/vapor interface was observed through a telescope as shown in Figure 2.4. The drop was illuminated from behind and the contact angle was measured using a goniometer scale fitted inside the eyepiece of the telescope. Three measurements were taken at each of three different areas on each sample and the mean of three values was reported.

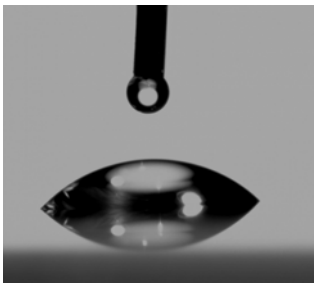

Figure 2.4 Photograph of a droplet of water onto the surface of a solid substrate.[116]

2.6.2 Ellipsometric thickness

A model M-2000V ellipsometer (J. A. Woollam Co. Inc) was used to measure the thickness of different layers. A sample was placed on the small table between the light source and detector. The height of the table could be adjusted to make reflected radiation go into the compensator and analyser. The table could also be moved in the horizontal and vertical direction to get the maximum signal in analyser. CompleteEASE software (J. A. Woollam Co. Inc) was used to capture the data. For each sample, the mean of measurements at three different locations was recorded. CompleteEASE was also used to analyse the data. A layer model with either Cauchy layer or B-Spline layer or both was built up to fit different layers. The thickness of constituent layers could be calculated from the model.

2.6.3 AFM images

AFM images were obtained by multimode AFM with a Nanoscope IV controller. Samples were washed prior to analysis by rinsing with ethanol and dried by nitrogen. Then the samples were attached onto a magnetic disk using carbon tape. The magnetic disk was placed on the scanner head. An optical video feed on the microscope was used to find the right position of the sample and cantilever was placed over the position. Then the laser was aligned on the end of the cantilever to get the maximum sum. The Vertical and horizontal position of the reflected laser point on the photodiode were adjusted to the right value (-2, 0 for contact mode and 0, 0 for tapping mode) respectively. The cantilever was lowered down to the surface and stopped when it almost contacted the surface through the control of software. Generally speaking, in contact mode, height and friction images were acquired while in tapping mode, height and phase images were acquired. The value of integral and proportional gains was optimized during the capture of images. NanoScope Analysis software was used to analyze the data. Information about the roughness of surfaces; structure of patterns and thickness of proteins could be obtained from those images.

2.6.4 XPS spectra

An Axis Ultra X-ray photoelectron spectrometer (Kratos Analytical, Manchester, UK) fitted with a delay-line detector (DLD) was used to obtain both survey and high resolution spectra. Samples were cleaned and attached to the sample bar, which was placed into an ultra-high vacuum chamber. A flow chart programme was set up to run analysis on each sample and save the data. CasaXPS software was used to analyse the data. In survey and high resolution spectra, all peak positions were charge-corrected using the position of the C1s peak (BE = 285 eV) in the high resolution spectrum as a reference for the reason that most organic monolayers contain saturated C-H bonds. The chemical composition of the surface could be obtained from survey spectra, and the bonding was obtained by analysing high resolution spectra.

2.6.5 Confocal fluorescence images

Confocal fluorescence images of protein patterns were captured using an LSM 510 Meta laser scanning confocal microscope (Carl Zeiss, Welwyn Garden City, UK). The sample was placed on a glass slide and a drop of glycerol-PBS solution was put on the sample. A microscope glass cover slide was placed on top of the sample and a drop of immersion oil was put on the cover slice over the sample but below the objective. 40x and 63x magnification oil dipping objectives with numerical aperture of 1.30 were lowered down to focus onto the surface of sample and image the micro-scale and nanoscale structures respectively. Argon lasers with different wavelength were used to excite different proteins or dyes. The fluorescence images were analyzed by software Zeiss LSM image browser.

Chapter 3 Study on the APTES SAMs formation

3.1 Introduction

In the present work, silane films are to be employed for the control of surface chemistry and to pattern the attachment of proteins.[140,141] In order to produce optimal conditions for the organization of membrane proteins, the conditions for silane film formation must first be optimised. In particular, uniform, defect-free films are required that exhibit minimal surface roughness in order that mechanisms of energy exchange in photosynthetic membrane proteins may be studied.

Much work has been reported on the formation of organosilane films on solid surfaces, but the detailed mechanism of film formation is still disputed.[142-144] A widely accepted mechanism for the silanization of silica is shown in figure 3.1. It is assumed that the head groups of the organosilanes undergo hydrolysis to form cross-links with each other before finally becoming coupled to the hydrated silica surface in a condensation reaction. Solvent, concentration, reaction time, and temperature all have effects on the attachment kinetics, but most studies only examine one or two of these parameters.[145] The aim of this work is to establish the optimum reaction conditions for preparing smooth, uniform and defect-free films of APTES on silica.

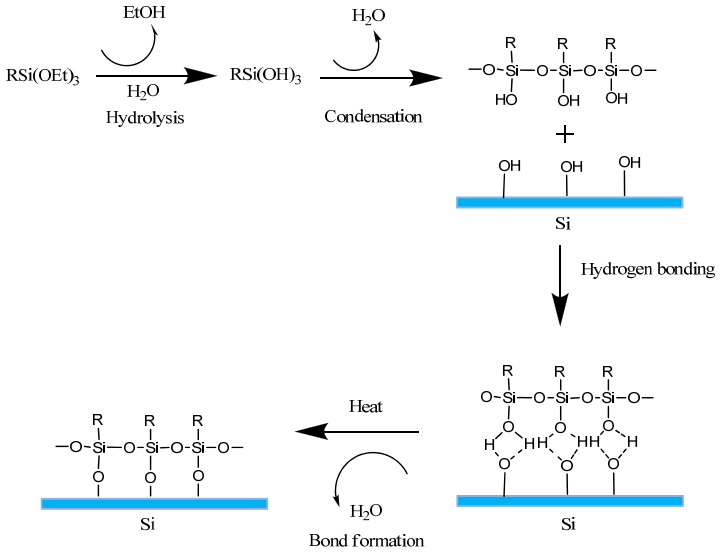

Figure 3.1 A putative mechanism for silanisation of a hydrated silica surface.

Aminosilanes are widely used as coupling agents for glass or other silicon based surfaces because of their bifunctional properties. 3-aminopropyltriethoxysilane (APTES) is one of the most commonly used silanes.[146] APTES can interact with the hydrated silica surface to form different conformations through hydrogen bonds, electrostatic attractions or siloxane bonds (figure 3.2).[147]

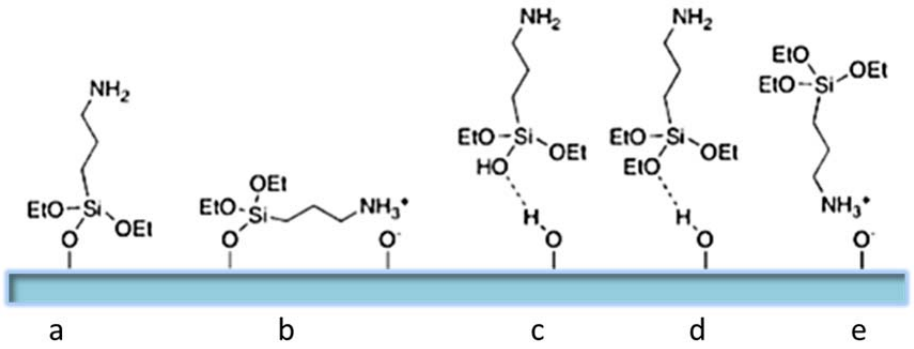

Figure 3.2 Different conformation of APTES on surface formed through a) siloxane bond; b) and e) electrostatic attraction; c) and d) hydrogen bonds.[148]

Because each APTES molecule has three ethoxy groups, it can polymerize under the right conditions. For example, in the presence of water, polymerization can give rise to several possible surface processes such as horizontal polymerization (two-dimensional self-assembly) and vertical polymerization (multilayers). Horizontal polymerization can occur when ethoxy groups are hydrolysed to form silanol moieties which can react with each other via a condensation reaction to produce siloxane bonds, while vertical polymerization can occur when APTES molecules physically adsorb to each other on an already APTES-treated surface.[148-150] Some reports show that amine groups may contribute to the self-catalysis of silane attachment and the formation of oligomers and polymers.[148,151,152] Considering the many different types of interaction like covalent bonding, hydrogen bonding and electrostatic attractions, it can be seen that APTES films with many configurations can be formed onto a silica surface (Figure 3.3).

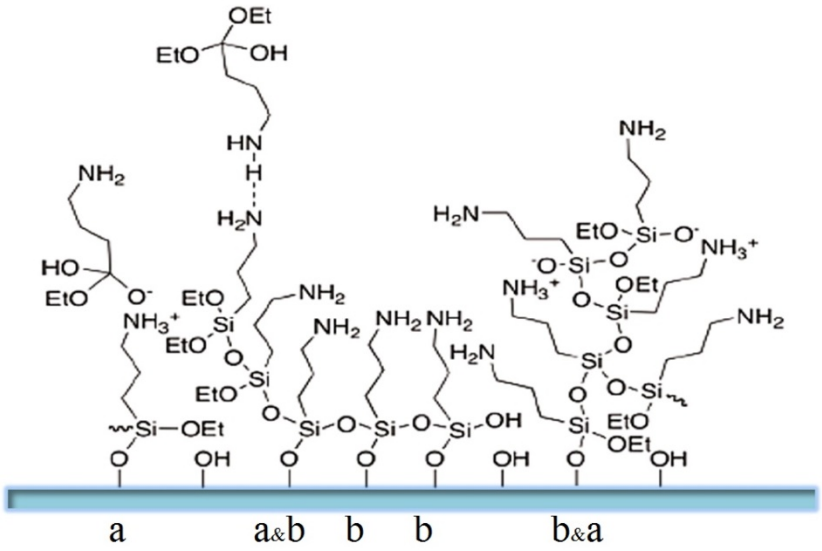

Figure 3.3 Different configurations of oligomers or polymers' film structures on the surface.[148] (a) Vertical polymerization; (b) horizontal polymerization.

Because of the complexity of the nature of bonding at the interface, the best method of film formation is still disputed. However, some basic mechanistic elements have been agreed upon. Firstly, attachment of APTES to the substrate is driven by the hydrolysis of the alkoxy groups followed by the covalent adsorption of the hydroxysilane product resulting in the formation of siloxane bonds. The quantity of water plays a vital role in the formation of a complete monolayer. Thompson suggested that water deficiency would cause the formation of an incomplete silane monolayer, while an excess of water could result in a high degree of polymerization of silane in the solvent. In their research, Thompson and co-workers had investigated the role of water in the silanization of glass by octadecyltrichlorosilane (OTS) in 1994.[153] Their results indicated that when OTS is dissolved in anhydrous toluene it only react with the surface silanol groups, producing a low density film. However when a small quantity of D_2O was added to the solvent, it resulted in the formation of a film nearly twice as dense as that obtained under anhydrous conditions. A great deal of evidence has showed that control of moisture is the key for the reproducible preparation of a siloxane film. Second, siloxane bond hydrolysis is self-catalysed by basic functional groups like amine, which can inter- and intra-molecularly catalyse the silane attachment and the formation of oligomers and

polymers.[152] Third, temperature may affect the formation of APTES films.[154] A popular assumption is that horizontal polymerisation between APTES molecules is enhanced upon heating so that denser APTES film and more ordered and structured Si-O-Si bonds will be formed. Temperatures ranging between 90℃ and 120℃ have been used to treat samples after removal from the silane solution, a process called *ex situ* post-annealing. There has been some speculation that *in situ* annealing, by increasing the solution temperature before reaction would have better effect. However, the self-polymerization of silane molecules may occur if the temperature of silane solution is too high. Moreover, solvent, concentration and reaction time all have some effect on the attachment kinetics. By studying these factors, our aim is to establish an optimum method for the routine preparation of smooth, dense and well-controlled APTES films. In addition, it is hoped to obtain some information about the process of APTES film formation.

3.2 Experiment

3.2.1 Materials

(3-Aminopropyl) triethoxysilane (APTES) (99%) and sodium dodecyl sulphate (SDS) were supplied by Sigma-Aldrich (Poole, UK) and used as received. Sulfuric acid ((1.83 S.G. 95+ %), hydrogen peroxide solution (100 volumes 30+ %), ammonia solution (S. G. 0.88, 35%) and toluene (HPLC grade) were supplied by Fisher Scientific (Loughborough, UK) and used as received. Ethanol (absolute) was supplied by VWR international (Lutterworth, UK). Silicon wafers (reclaimed, p-type, <100>) were supplied by Compart Technology (Tamworth, UK) and cover slips (20 x 60 mm) were supplied by Menzel-Gläser (Braunschweig, Germany). Water was de-ionised using an ELGA Veolia water system (PURELAB Ultra).

3.2.2 Variation of water content in reaction solvent

Toluene was chosen as the reaction solvent. The water content was measured using the Karl Fisher Titration method on different days. 10 mL toluene was removed from the original 2.5 L bottle of toluene and kept in a sealed 15 mL tube for analysis. Each day, the humidity and temperature of the environment were recorded using the testo 615 humidity meter.

3.2.3 Preparation of APTES SAMs

Substrates, either glass slides or silicon wafers, were cleaned as discussed in chapter 2. Tubes containing substrates were removed from the oven and allowed to cool. The tubes were filled with a solution of APTES in toluene. Care was taken to ensure that the whole substrate was immersed in. The reaction time varied from 15 min to 72 h. After reaction, substrates were rinsed with toluene and ethanol several times and dried under a stream of nitrogen. The tubes containing substrates were placed on the heater to anneal the samples for half an hour at 120°C. In control experiments, the same procedure was used but without addition of APTES to the solvent.

3.2.4 Surface analysis

Contact angles were measured using a Rame-Hart goniometer by the static sessile drop method. Three measurements were taken at each of three different areas and the average of these values was reported.

The thickness of the APTES films was measured by ellipsometry using an ellipsometer M-2000V (J. A. Woollam Co. Inc). For each sample, the mean of measurements at three different locations was recorded. The thickness of the native oxide layer (empty samples) was measured first and then the thickness of the whole film was measured after reaction. In the work described here, the APTES coated substrates may be treated simply as consisting of isotropic and homogeneous films. The samples were modelled using two layers, one a native oxide layer and the other a Cauchy layer corresponding to the APTES film. The thickness of the native oxide layer is ca. 1.9nm and the thickness value of Cauchy layer was calculated from the software Complete EASE.

The roughness was obtained from AFM height images acquired using a Digital Instruments Nanoscope IV multimode atomic force microscope (Veeco Instruments, Cambridge, UK). For each sample, three height images from different areas were obtained. The root mean square (RMS) values were calculated through the software supplied with AFM instrument and the results of measurements from different areas were averaged.

Survey and high resolution spectra were obtained using an Axis Ultra DLD X-ray photoelectron spectrometer (Manchester, UK) and analysed using the CasaXPS software.

3.3 Results and discussion

3.3.1 Water content in solvent

From the previous discussion, we know that water plays a vital role in the formation of silane SAMs. In this study HPLC grade toluene was used as received, and it was essential to determine how much water is in the solvent. The Karl Fisher titration is a classical and widely used method for the determination of trace amounts of water in a sample through a colorimetric or volumetric titration. The basic mechanism is that one mole I_2 will be consumed by one mole H_2O. Two moles of electrons will be consumed by one mole H_2O so that the amount of current needed to generate I_2 can then be used to calculate the amount of water in the original sample. The reaction equation is shown below. B represents base, usually imidazole and ROH represents alcohol, usually MeOH.

$$B{\cdot}I_2 + B{\cdot}SO_2 + B + H_2O \rightarrow 2BH^+I^- + BSO_3$$
$$BSO_3 + ROH \rightarrow BH^+ROSO_3^-$$

Figure 3.4 shows measurements of the water content on each day along with the corresponding humidity. The water content of toluene from a newly opened bottle (Day 1) to the one with little solvent inside (Day 10) was measured. At the start, there was 67.3 ppm water in the newly opened bottle, and the water content increased to 93.3 ppm over ten days. The room temperature was typically ca. 20 °C but the humidity changed every day. However, these parameters had little effect on the variation of water content. The water content of toluene left in the bottle increased gradually from Day 1 to Day 10 at either high or low humidity. The water content seems to depend only on the time the solvent is kept under ambient condition and amount of remaining solvent in the containers. Subsequent measurements will yield higher water content than previous ones because the toluene would adsorb water from air around. If the bottle of solvent is newly opened and full, the water content is lower. If the solvent has been used and left in ambient air for a period, the water content will be higher. However, even for the highest value on Day 10, the amount of water in the solvent was very small and would

be expected to have very little effect on the formation of APTES SAMs.

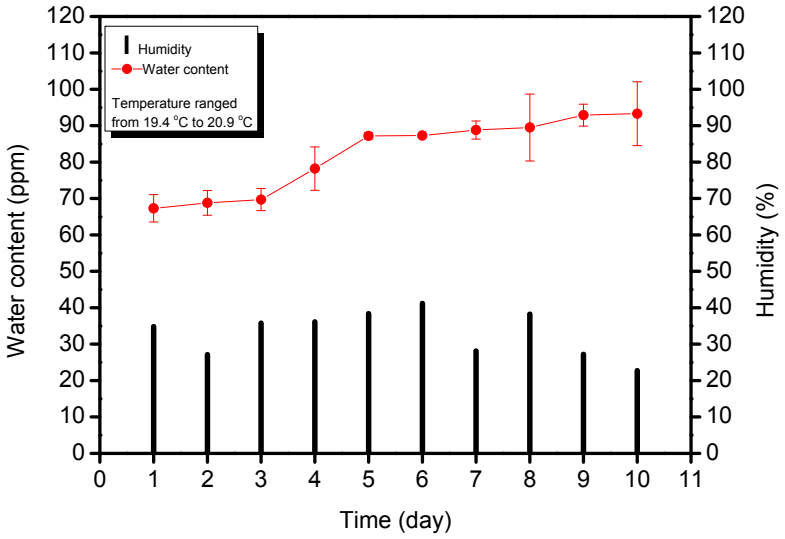

Figure 3.4 Graphic shows the water content of toluene along with the corresponding temperature and humidity as a function of time.

3.3.2 Water contact angle

Figure 3.5 shows the variation in the contact angle of APTES films with time at a variety of concentrations of APTES in toluene. Although the results cannot be fitted into a reasonable dynamic equation, some trends have been observed. In Figure 3.5 (a), pink triangles show the results of control experiments, in which the adsorbate was not added to the solvent. All the contact angles are below 10°. This means that the solvent, toluene, has a very weak interaction with the clean substrate surfaces. For the samples prepared with a very low APTES concentration, 10^{-7} (v/v) and 10^{-6} (v/v), the contact angle increases from ca. 5° (green triangles) and 15° (blue triangles) respectively to ca. 40° after 72h. For samples prepared with higher APTES concentrations, 10^{-5} (v/v) and 10^{-4} (v/v), the contact angles are ca. 35° (red points) and 40° (black squares) respectively at the earliest time point and increase slowly to ca. 50° after 72h. Figure 3.5 (b) shows the contact angles for surfaces prepared from solution with high APTES concentration. Even at short immersion times, the contact angle is much higher than the value measured for the clean substrate surface (ca. 35° - 40°), and it increases little with extended immersion times. Even after 72h, a contact angle of ca. 40° was measured.

The results indicate that the monolayers of APTES formed very quickly when the concentration was high.

(a)

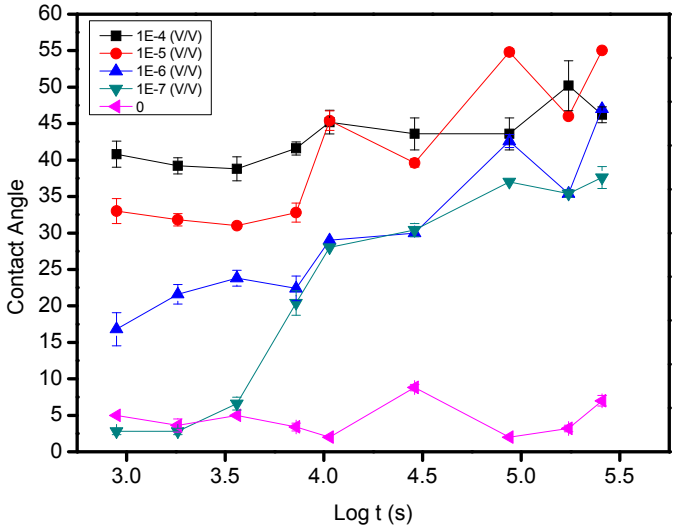

(b)

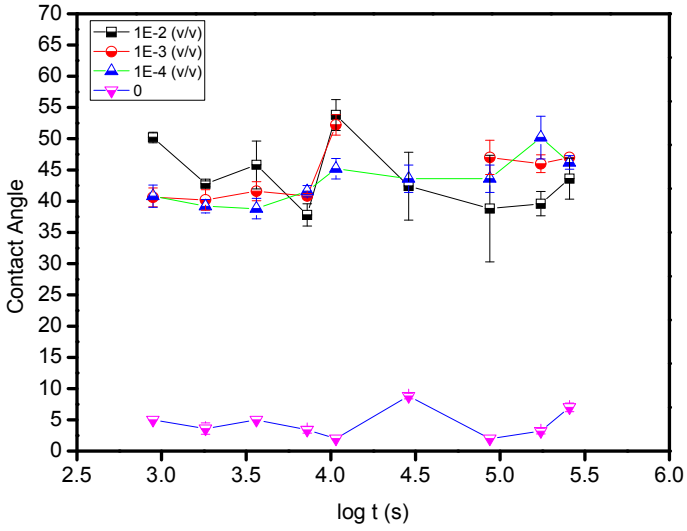

Figure 3.5 Graphic illustrates the relationship between water contact angle of APTES films, reaction time (log t) at (a) low concentration (v/v = 10^{-4}, 10^{-5}, 10^{-6}, 10^{-7}) and (b) high concentration (v/v = 10^{-2}, 10^{-3}, 10^{-4}).

Previous reports have shown that smooth amine-terminated surfaces have a contact angle up to 60° while clean substrates terminated with hydroxyl groups have a contact angle close to 0°. From Cassie's law[155]:

$$\cos\theta_c = f_1 \cos\theta_1 + f_2 \cos\theta_2$$

Where θ_c is the effective contact angle for a liquid drop on a composite surface, θ_1 is the contact angle for component 1 occupying a fraction f_1 of the surface and θ_2 is the contact angle for component 2 with area fraction f_2 present in the composite material. In a 2-component system one component is air with a contact angle θ_2 of 180°. If $\cos\theta_2 = -1$, the equation reduces to:

$$\cos\theta_c = f_1 \,(\cos\theta_1 + 1) - 1$$

It means small f_1 and large θ_1 can create large contact angle, which implies that roughing up a surface could increase the apparent surface contact angle.

3.3.3 Roughness

Most surfaces are not ideally smooth so a model is needed to describe the contact angle of a rough and heterogeneous surface. The Cassie–Baxter equation does this:

$$cos\,\theta * = \gamma f cos\,\theta + f - 1$$

Where θ is the contact angle for ideal surface, and $\theta*$ is the contact angle for equilibrium state. γ is the roughness ratio of the wet surface area and f is the fraction of solid surface area wet by the liquid.

This equation implies that when we increase the surface roughness, the surface will be more hydrophobic. So it is important to study the effect of the roughness of the APTES film. Figure 3.6 shows the roughness of APTES surfaces prepared in different

conditions. All the roughness values are ≤ 0.5nm, which means the APTES film is very smooth and that the roughness is not expected to influence the contact angle significantly. Although the mean RMS roughness is small under most conditions, some trends are observed. The roughness decreases to 0.1 nm between 3h and 24h depending on the concentration of adsorbates and then increases again. From the discussion about APTES film formation in the introduction to this chapter and the distribution of roughness data, it is suggested that this phenomenon may result from the formation of APTES multilayers. At the start of the reaction, a monolayer of APTES is formed on the hydrated surface through the formation of Si-O-Si bonds. Subsequently, more molecules aggregate onto the surface. They link with each other through different interactions and finally form layer by layer APTES films. During the formation of an APTES film, roughness will increase with the aggregation of molecules. Eventually, as a thick layer builds up, the surface becomes flat and roughness decreases. The animation below the graph in Figure 3.6 shows the formation process of multiple layers at the concentration of 10^{-2} (v/v) and it also displays the change of roughness during this process. The reaction condition (Concentration of APTES in toluene equals to 10^{-2} v/v) corresponding to the black blocks in the graph were marked out by black solid line to show their AFM images in Figure 3.7.

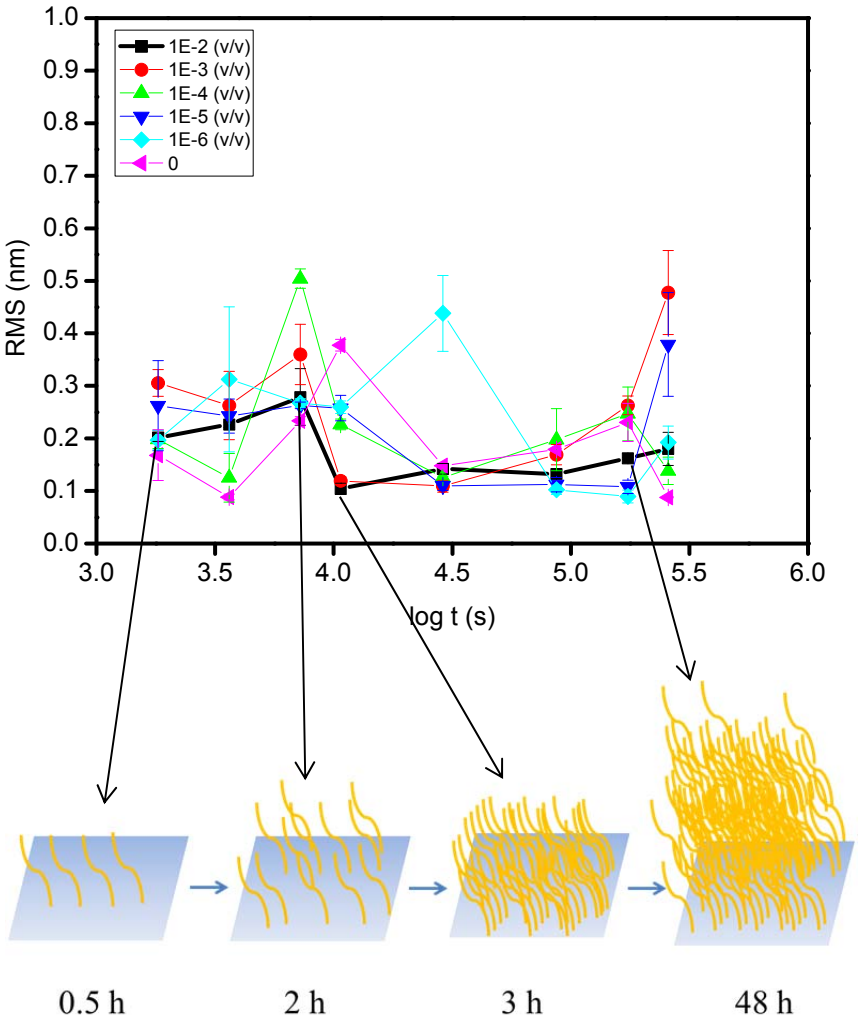

Figure 3.6 The Graph (up) shows the variation of the roughness of APTES films dependent on the immersion time at different concentrations and the animation (down) shows the formation of multiple layers at the concentration of 10^{-2} (v/v).

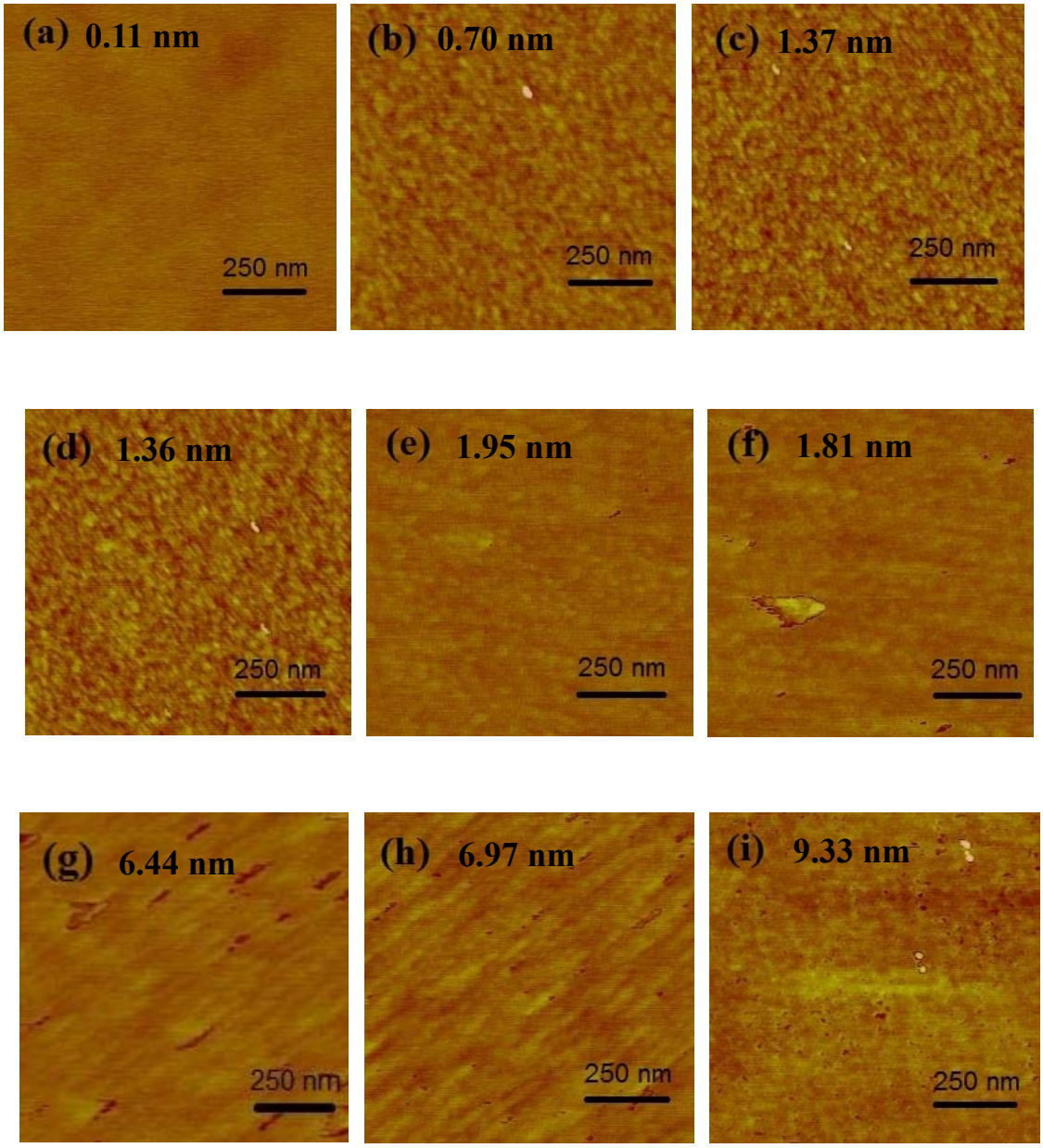

Figure 3.7 AFM height images (size: 1μm * 1μm; z-range: 5nm) and corresponding thickness of APTES films prepared in 10^{-2} (v/v) solution for (b) 30min; (c) 1h; (d) 2h; (e) 3h; (f) 8h; (g) 24h; (h) 48h; (i) 72h, (a) is the height image of clean silicon wafers.

AFM height images support the suggestion of the formation of multiple layers. Figure 3.7 shows height images of APTES films prepared in a 10^{-2} (v/v) solution at different reaction times. The surface of a clean silicon wafer is very smooth (a). After 30min, the surface becomes rough with what appears to be particulate matter being observed (b).

After 1h, more particle-like matter is formed and aggregates on the surface to form areas that resemble small “island” (c and d). After still longer time than 3h, the surface roughness begins to decrease again (e and f). Eventually, after long time like 24 h the surface becomes rougher again (g), attributed to the formation of several layers of adsorbates (h and i), which can be deduced from the thickness of APTES films.

3.3.4 Ellipsometry

Ellipsometry was used to determine the thickness of APTES films (Figure 3.8). From Figure 3.8 (a), it can be seen that the thickness increases with the reaction time when the concentration is high. Moreover, the thickness does not stop increasing when monolayer coverage is reached (expected to be at a thickness of ca. 1nm). For example, the thickness of APTES films prepared in 10^{-2} (v/v) solution increased from ca. 0.7 nm to ca. 10 nm after 72 h, which was also shown in Figure 3.7. The thickness of APTES films prepared in 3 x 10^{-2} (v/v) solution was even greater, at ca. 40 nm after 72 h. Figure 3.8 (b) shows the thickness change of the samples prepared in solution with lower concentration. The thickness increased slowly with reaction time. For example, the samples prepared in solution with an APTES concentration less than 10^{-5} (v/v), the thickness did not reach 2 nm even after 72 h. However, the corresponding contact angle (around 50°) suggested that the adsorbate should have a good coverage so that we can assume that an APTES monolayer had formed, because the thickness of an APTES monolayer is expected to be less than 1 nm. The thickness results for surfaces prepared at high APTES concentrations condition are probably explained by the formation of multilayers, which is consistent with the previous AFM images.

(a)

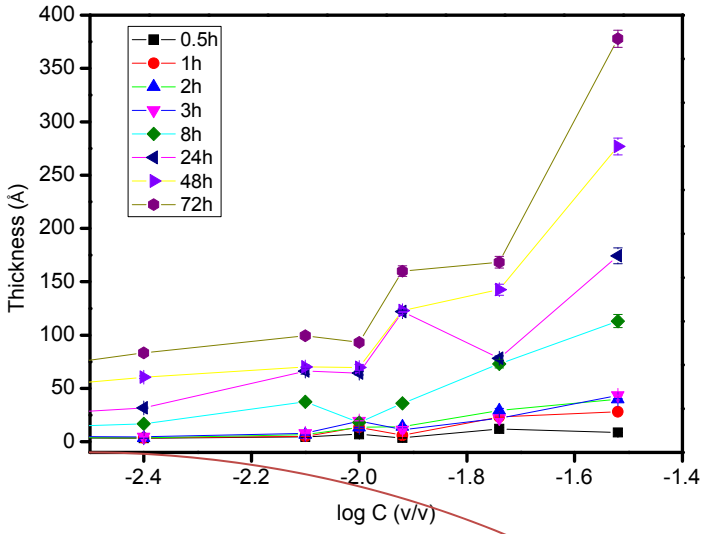

(b)

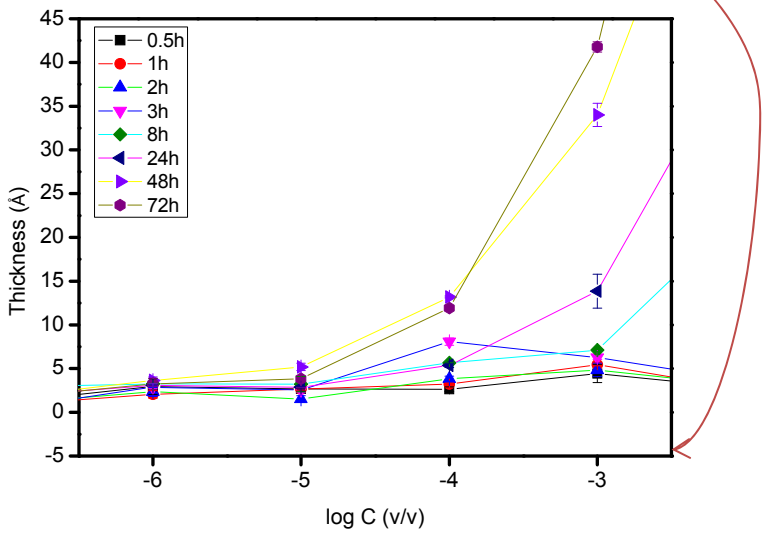

Figure 3.8 Dependence of the film thickness on (a) high concentration and (b) low concentration of APTES solution in toluene at different immersion times.

3.3.5 XPS analysis

Film formation was investigated by XPS. Figure 3.9 (a) shows the C1s XPS spectrum. It has been fitted with two components, one corresponding to aliphatic carbons (285 eV) and the other to carbon singly bonded to nitrogen (287.5 eV). Figure 3.9 (b) shows the

N1s XPS spectrum. Only one component is observed, corresponding to the nitrogen atoms in the amine group (400.3 eV).

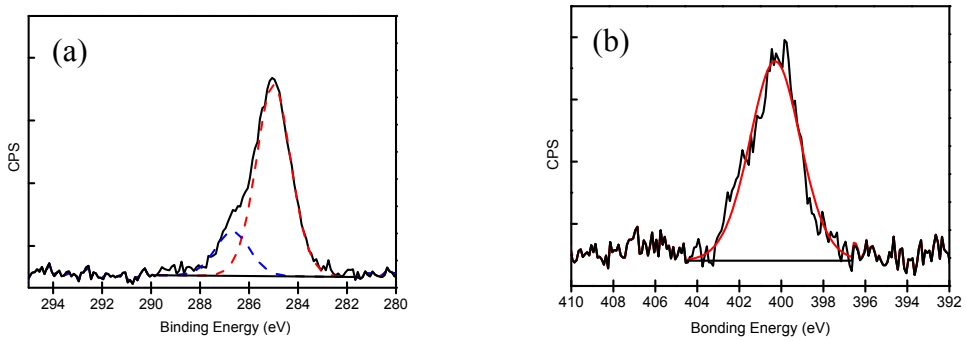

Figure 3.9 XPS spectra of APTES films prepared in 10^{-4} (v/v) solution for 72h (a) C1s region and (b) N1s region.

If APTES assembles in layer by layer fashion on the substrates, the amount of nitrogen on surfaces will increase with immersion time. The area of the N1s peak was thus measured for films formed under a variety of conditions. Figure 3.10 shows the change in the N1s region for samples prepared with different reaction times and concentrations. In XPS N1s spectra in Figure 3.10 (a) (left), it's observed that the area of the N1s peak increases with reaction time when solution concentration is kept to 10^{-4} (v/v), which results from the aggregation of APTES molecules onto the surface. Similarly, if we keep the reaction time to half an hour and increase the solution concentration, the area of the N1s peak will increase as well (Figure 3.10b，left). The graphics on the right side shows the corresponding nitrogen composition of these APTES surfaces determined from those spectra on the left. The percentage of nitrogen increases with the immersion time and concentration in a general trend, which is consistent with the changes observed in the N1s spectra on the left. All these results support the formation of multilayers APTES films.

(a)

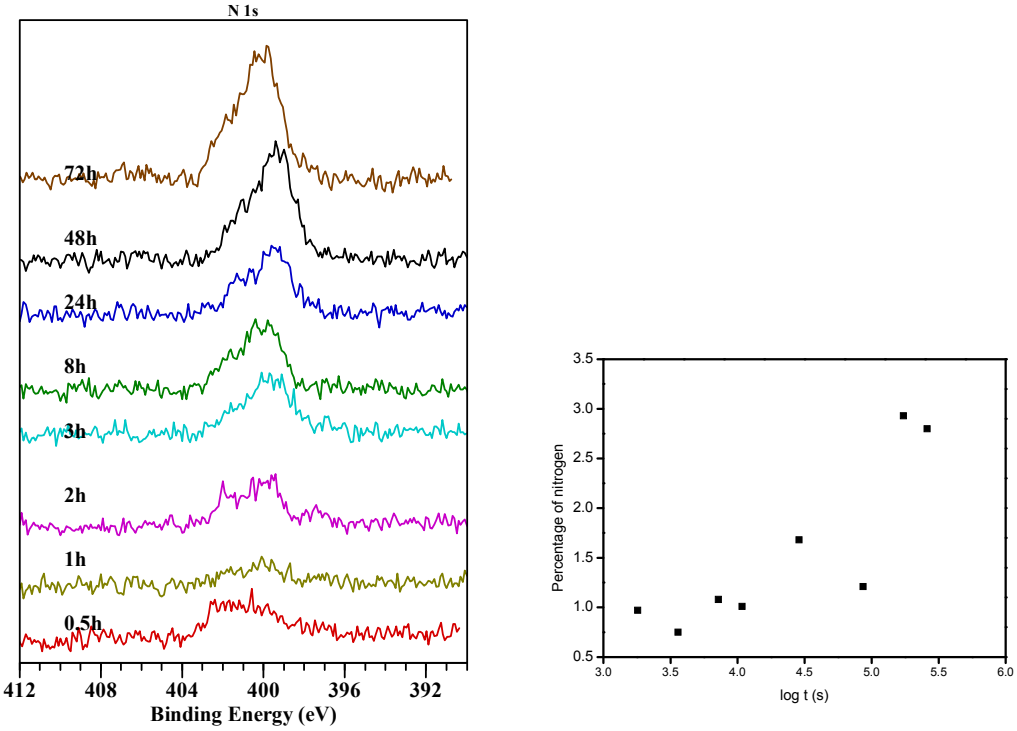

(b)

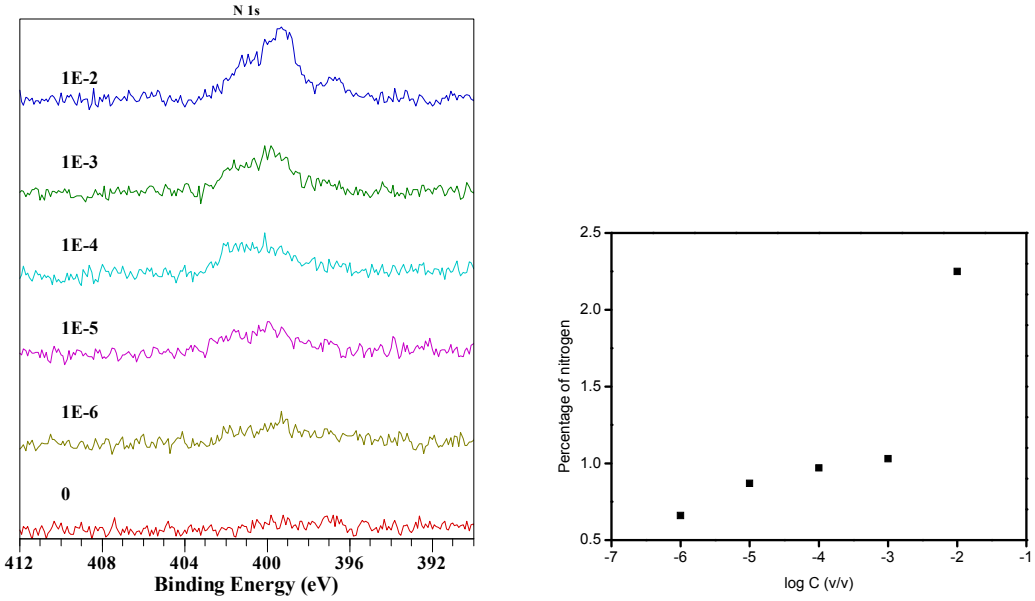

Figure 3.10 XPS nitrogen spectra (left) and their compositional data (right) for APTES films as a function of (a) immersion time when concentration is 10^{-4} (v/v) and (b) concentration when reaction time is 0.5 h.

3.4 Conclusions

APTES films have been formed on hydrated substrates under ambient conditions. Study of the water content in HPLC grade toluene indicated that the amount of water in the solvent was small and varied comparatively little over time. It was found that small amount of water ranged from 67.3 ppm to 93.3 ppm in HPLC grade toluene did not affect the film formation process during the experiment. At room temperature, contact angle results indicate that APTES surfaces prepared by our method have good surface coverage with a water contact angle up to ca. 55°. The surface roughness is lower than 0.5 nm, which means that they are quite flat surfaces. AFM height images reveal the surface topography, and indicate the formation of multilayers. Ellipsometric results show that thickness increases with the immersion time and concentration, and show that films thicker than a monolayer are typically formed. Furthermore, XPS results provide us with information about the variation of surface chemical composition as a function of immersion time and concentration, supporting the hypothesis that multilayer formation occurs. Considering all the data achieved, it's thought that a dense and smooth APTES monolayer can be formed in 10^{-2} (v/v) APTES solution in toluene for 1 h.

Chapter 4 Single and Multi-protein patterning using Aminosilanes with Protein-Resistant Photolabile Protecting Groups

4.1 Introduction

Protein patterning at the micrometer- or nanometer-scale is a crucial step in the fabrication of advanced biochips and lab-on-chip devices. Much progress for single protein patterning have been reported.[83,156-158] However, the fabrication of patterns formed from multiple proteins remains a major challenge due to the absence of suitable methodology. Some progress has been made on the micropatterning of multiple proteins. Microcontact printing has been used to prepare micrometre scale patterns from multiple proteins.[159-161] Eichinger et al.[159] prepared multiple protein patterns by the sequential printing of proteins with micrometer precision in registration using a polydimethylsiloxane (PDMS) stamp mounted on the stage of an inverted microscope. Chalmeau et al.[160] developed a new process called one-step-multiple-microcontact printing using a elastomeric multilevel PDMS stamp with two different molecules to contact the surface sequentially and then get the patterns of two different molecules. Microscope projection photolithography is another popular technique to prepare micrometre scale patterns of multiple proteins.[162-164] Kim et al.[162] prepared protein arrays composed of multiple proteins using microscope projection photolithography on a new protein-friendly photoresist polymer, poly (2, 2-dimethoxy nitrobenzyl methacrylate-r-methyl methacrylate-r-poly (ethylene glycol) methacrylate) (PDMP), which becomes soluble in near-neutral physiological buffer solutions upon UV exposure and exhibits excellent resistance to protein adsorption. Midthun et al.[165] reported the development of imprint lithography to prepare micrometre scale patterns of multiple proteins. They synthesized an imprint resist (ImR), which was fluorinated enough to be processable in fluorinated hydrofluoroether (HFE) solvents and free of unnecessary functional groups that might react with biomolecules. Multiprotein arrays were patterned by imprint lithography using these ImR and HFE solvents.

There is less work on the nanopatterning of multiple proteins. Christman et al.[75] prepared the multiple proteins at the nanoscale by electron beam lithography. They synthesized four different PEGs modified with biotin, maleimide, aminooxy and nitrilotriacetic acid respectively at the chain ends. The polymers were cross-linked on a silicon surface using electron beams to form micron- or nanosized structures sequentially on the same chip. Then proteins with different biotin binding sites could be attached onto specific regions. Multicomponent nanoscale protein patterns were then fabricated. Huang et al.[166] reported the patterning of bioprobes with nanoscale features on biocompatible polymer substrate by nanostencil lithography. They prepared a stencil with arrays of reservoirs and a SiNx mask with nanoapertures under each reservoir. Each reservoir could be loaded with different biomolecule solutions so that different biomolecules were patterned on the substrate through the apertures on the mask. After the removal of the stencil, multiple biomolecule patterns were left on the surface. Finally, some layer by layer patterning of multiple proteins based on specific protein-protein interactions (eg. Avidin-Biotin) have been reported.[81,95,167]

Therefore, it can be seen that proteins have been patterned at micrometre and nanometre length scales by techniques that include micro-contact printing[159-161], electron beam lithography[157,168-170], scanning probe lithography[83,156,158,171-174]. However, the main drawback of these techniques is their lack of capability to execute chemical transformations. One alternative approach is to use near-field optical techniques to carry out photochemical conversion on monolayers of moleules with photoactive functional groups. For example, monolayers of alkanethiols could be oxidised to alkylsulfonates by UV light in the near field,[103,175,176] benzylchloride terminated siloxane monolayers could be photoconverted into carboxylic acids[177] and oligo (ethylene glycol) groups could be oxidised to yield aldehyde groups after irradiation[67,178]. An attraction of such approaches is that they facilitate the integration of patterning with synthetic chemical methodology.[46,68] Scanning near field photolithography (SNP) was used by Alang Ahmed et al.[68] to selectively deprotect films formed by the adsorption of an aminosilane (APTES) protected by oligo (ethylene glycol) (OEG) modified

2-nitrophenylethoxycarbonyl (NPEOC) groups, OEG-NPEOC-APTES on glass. This silane contains a nitrophenyl photocleavable protecting group NPEOC, with an OEG substituent at either the meta or the para position relative to the nitro group, to make the film protein resistant until photodeprotection takes place.

Nitrophenylpropyloxycarbonyl (NPPOC) protecting group has a high photodeprotection efficiency and was introduced earlier as a protecting group for amines.[179-181] It undergoes a specific photocleavage mechanism to yield an alkene byproduct.[46,182] The NPEOC protecting group has a similar chemical structure to NPPOC and was introduced as a new building block for solid phase synthesis.[183-185] Alang Ahmed et al.[68] functionalised the phenyl ring of the NPEOC group with protein-resistant OEG chains to prevent nonspecific adsorption. The structure and proposed mechanism of deprotection of OEG-NPEOC-APTES are shown in Scheme 4.1. In this thesis, all the OEG-NPEOC-APTES molecules have seven EG chains (n=7).

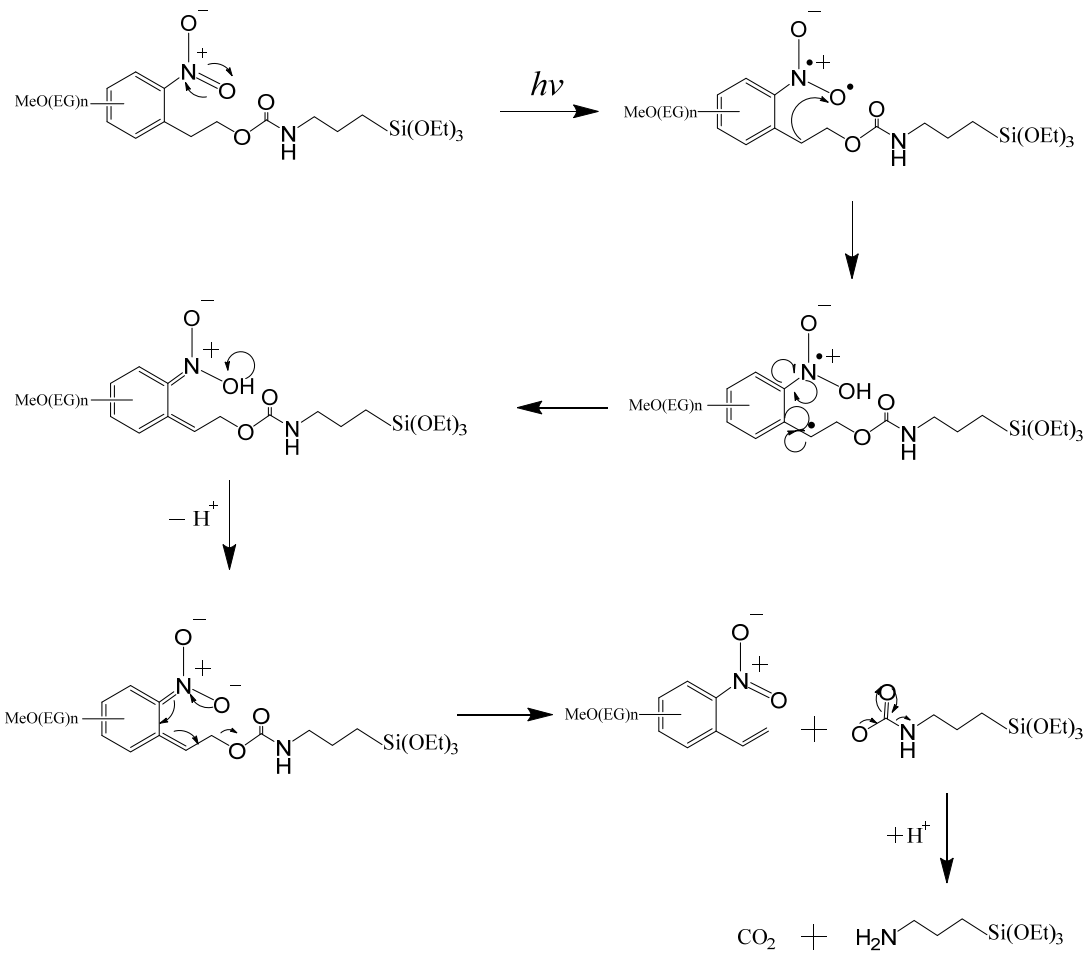

Scheme 4.1 Proposed mechanism for the photodeprotection of OEG-NPEOC-APTES.

After irradiation with UV light, OEG-NPEOC-APTES is photocleaved to leave APTES on the surface. Following photodeprotection, derivatization with cross-linkers is carried out. Finally proteins like XFP, avidins and membrane proteins are attached to form micro or nanoscale patterns. In this work, results are presented following surface patterning using mask-based patterning, interference lithography (IL) and SNP. Glutaraldehyde (GA) had been chosen as the cross-linker, which is a molecule with two aldehyde ends that links the free amine groups on the substrates with the amine groups in proteins efficiently. Amine groups in proteins are either at the N-terminus or at the side chain group like lysine residues which are placed at different sites of proteins depending on their sequences. So in this chapter, all proteins are bound onto the surfaces at either N-terminus or lysine residues with random orientation.

The feasibility of fabricating multiple protein patterns has been explored by taking advantage of the separation of writing and reading functions in a SNOM system and utilising SNP to over-write patterns composed of different proteins in the same region of a sample.

4.2 Experiment

4.2.1 Materials

Sulfuric acid ((1.83 S.G. 95+ %), hydrogen peroxide solution (100 volumes 30+ %), ammonia solution (S. G. 0.88, 35%) and toluene (HPLC grade) were supplied by Fisher Scientific (Loughborough, UK) and used as received. Ethanol (absolute) and glutaraldehyde (GA) solution (Grade II, 50% in water) were obtained from VWR international (Lutterworth, UK). Phosphate buffered saline (PBS) tablets, ammonium acetate and HEPES were supplied by Sigma-Aldrich (Poole, UK) and prepared into buffer solutions (pH 7.4). Oligo (ethylene glycol) modified 2-nitrophenylethoxycarbonyl protected aminopropyltriethoxysilane (OEG-NPEOC-APTES) was synthesized by AF ChemPharm Ltd (Sheffield, UK). Histidine-tagged (His-tagged) XFP and CPCA were provided by Dr Micheal. Carton (Department of molecular biology and biotechnology). Membrane proteins LH1 and LH2 isolated from R. sphaeroides were also provided by Dr Micheal. Carton. Streptavidin and NeutrAvidin were supplied by life technologies and used as received. Silicon wafers (reclaimed, p-type, <100>) were supplied by Compart Technology (Tamworth, UK) and cover slips (22 x 50 mm) were supplied by Menzel-Gläser (Braunschweig, Germany). Quartz slide (50 mm x 25 mm x 1 mm), 1000 mesh and 2000 mesh copper grids with diameter of 3.05 mm were supplied by Agar Scientific Ltd (Stansted, UK). The copper grids were used as mask during UV lithography. Water was de-ionised using an ELGA Veolia water system (PURELAB Ultra).

4.2.2 Preparation of OEG-NPEOC-APTES modified substrates

Silicon wafers, quartz or glass slides were cleaned with piranha solution and RCA solution. All the clean slides were immersed in a 0.1% (v/v) solution of OEG-NPEOC-APTES in toluene for 48 h. After reaction, the substrates were washed by rinsing with toluene and ethanol several times and dried under a stream of nitrogen. Finally the samples were annealed by heating to 120 ℃ for 1 h in a vacuum oven.

4.2.3 Study on the photodeprotection rate of OEG-NPEOC-APTES

Silica modified by OEG-NPEOC-APTES was cut into small samples (0.5 cm x 1 cm) under a dark environment. 244 nm or 325 nm wavelength laser was used to irradiate the samples for different times. Samples were analysed by XPS. Software CasaXPS was used to analyse the obtained spectra.

4.2.4 Preparation of single protein patterns on OEG-NPEC-APTES surfaces

Glass slides modified by OEG-NPEOC-APTES were cut into small pieces. Samples were patterned by exposure to laser illumination at 244 nm through a copper grid mask to make microscale patterns or using a Lloyd's mirror interferometer technique to make nanoscale patterns. For near-field lithography, a 325 nm wavelength laser was coupled to a WITEC SNOM system. After exposure, the samples were immersed into PBS solution (pH 7.4) for 15 min then GA solution (25% v/v in water) for 30 min and rinsed with water. Then the samples were incubated in protein solution overnight. The next day, samples were rinsed with PBS solution (pH 7.4) or HEPES buffer (pH 7.4) and the samples were stored in PBS solution or HEPES buffer at 4 ℃ in a fridge before subsequent analysis. The preparation process is shown in Scheme 4.2.

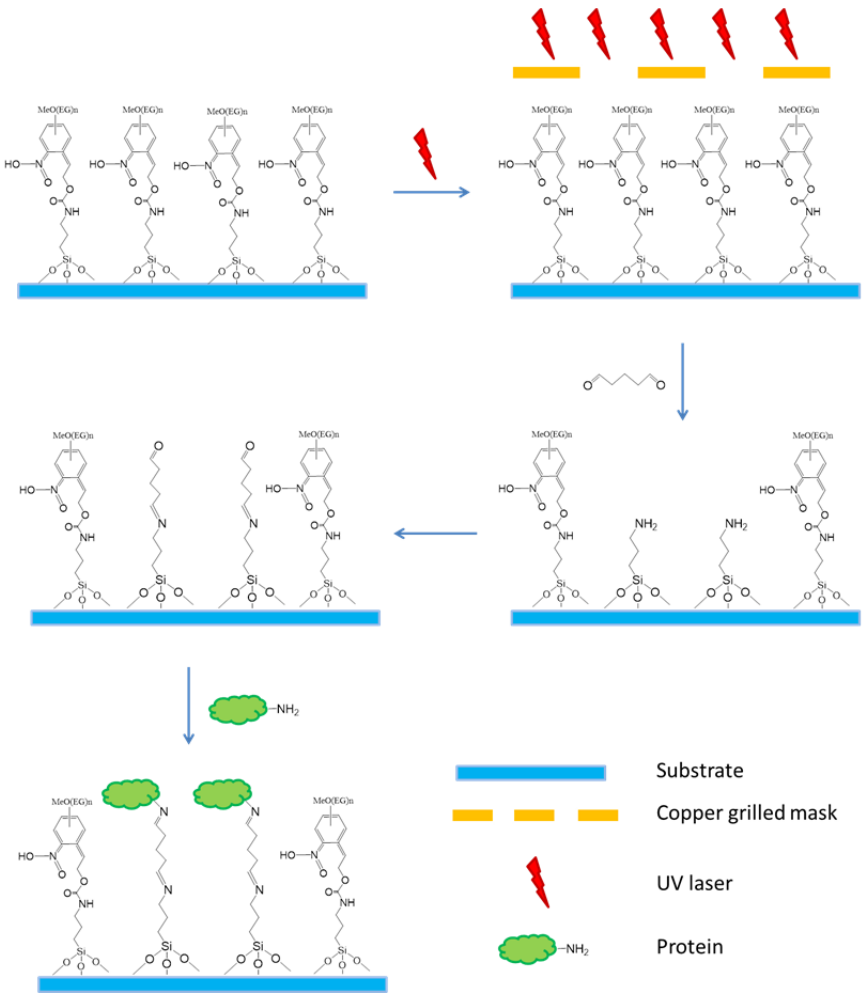

Scheme 4.2 Schematic illustration of the preparation process of single protein patterns through photolithography. Proteins are bound onto the surfaces at either N-terminus or lysine residues with random orientation.

4.2.5 Preparation of multi-protein patterns on OEG-NPEOC-APTES surfaces

After fabrication of micropatterns by mask-based patterning or nanolines by IL or SNP, flood illumination of the sample was used to deprotect remaining regions of the surface, enabling attachment of a second protein. Alternatively, multiple component patterns were fabricated by over-writing nanolines fabricated from different proteins using SNP. After the first patterning step, a protein was attached, the sample was rinsed and it was returned to the SNOM system. Using a finder-grid structure the region in which the first pattern had been formed was located, and a second series of lines was written over the top of it. The sample was rinsed by PBS solution (pH 7.4) or HEPES buffer (pH 7.4) for

several times and kept in PBS solution or HEPES buffer at 4 ℃ in a fridge before subsequent analysis. Preparation process of two protein patterns can be shown in Scheme 4.3.

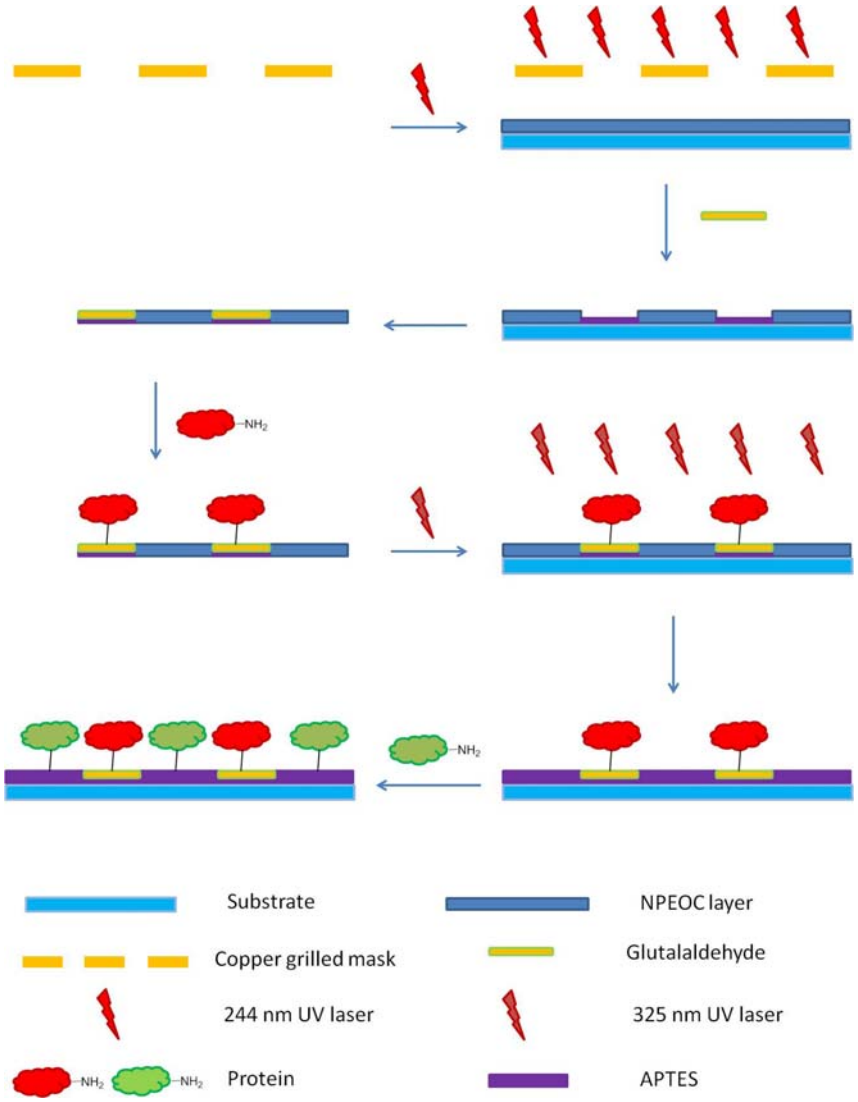

Scheme 4.3 Schematic illustration of the preparation process of two protein patterns through mask-based UV photolithography. Proteins are bound onto the surfaces at either N-terminus or lysine residues with random orientation.

4.2.6 Analysis of the single and multi-protein patterns

Patterning quartz and glass slides' samples with fluorescence have good optical properties so they are suitable for imaging by scanning confocal microscopy. Samples

with membrane proteins stored in HEPES buffer (pH 7.4) were rinsed by 100 mM ammonium acetate solution (pH 7.4) and dried by nitrogen gas. Ammonium acetate is volatile at low pressure so it can be used to replace the non-volatile salts in other buffers and reduce the contaminants on the surface. Then AFM in tapping mode was used to capture the images of protein patterns. Silicon wafers have very smooth surface so that protein patterns on this substrate are usually analysed by AFM.

4.3 Results and discussion

4.3.1 XPS

Figure 4.1(a) shows the C1s XPS spectrum of an OEG-NPEOC-APTES specimen. It was fitted with three components. The aromatic ring carbons and aliphatic carbons are represented by a single component at 285.0 eV while the carbon atoms bonded singly to oxygen and nitrogen are represented by a single component at 286.5 eV because they have similar chemical shifts. A third component was fitted at 289.3 eV due to the carbon atom in the carbamate group. Figure 4.1(b) shows the N1s region of XPS spectrum, which has been fitted with two components. The lower bonding energy (BE) peak is attributed to the nitrogen in the NHR group (R = H or C) (400.0 eV) while the higher BE peak is attributed to the nitrogen in the NO_2 group (406.0 eV). The ratio of these two peaks was expected to be 1, but the NO_2 component in Figure 4.1(b) is smaller than expected (NO_2/NHR equals to ca. 1:3). Some literature[186] suggests that this may be explained by the photo removal of the nitro group by the X-rays during analysis. In this spectrum, the ratio of these two peaks (NO_2/NH_2) before exposure was ca. 1:3.

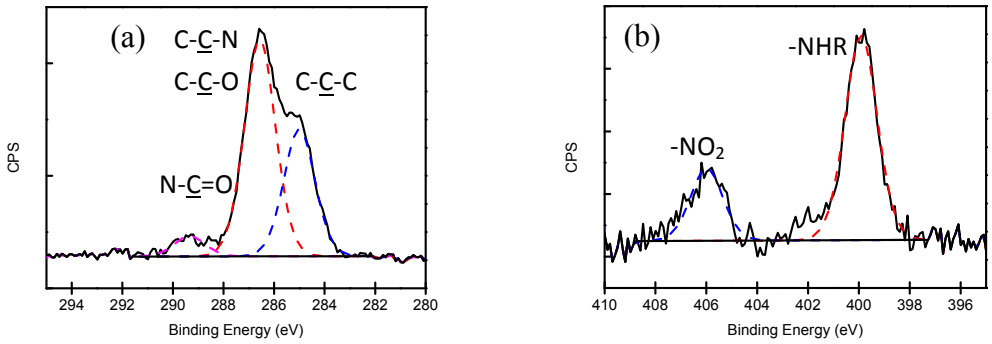

Figure 4.1 XPS spectra of OEG-NPEOC-APTES surfaces, (a) C1s region and (b) N1s region.

4.3.2 Photodeprotection rate of OEG-NPEOC-APTES

Figure 4.2 shows the variation in the N1s region in the XPS spectrum of OEG-NPEOC-APTES surfaces after exposure to 244 nm radiation at different doses. Before exposure, the ratio of NO_2/NH_2 peak area was ca. 1:3. The size of the NO_2

component decreased with increasing exposure. Its area became negligible after an exposure of 15 Jcm^{-2}. From ratio of the peak area corresponding to NO_2 and NHR groups, deprotection rate of OEG-NPEOC-APTES dependent on dose was deduced.

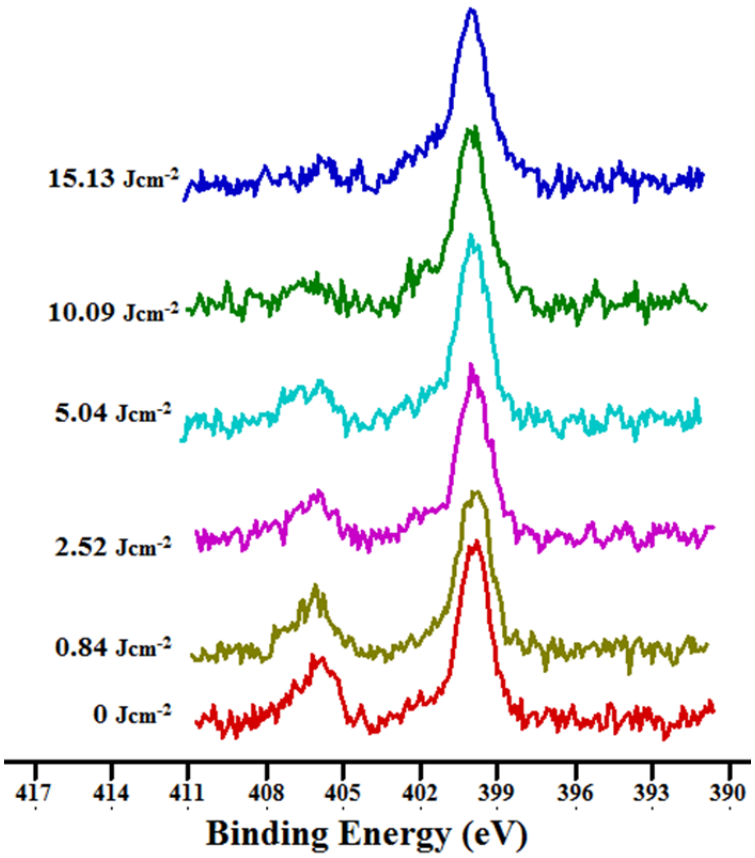

Figure 4.2 Variation of N1s regions in the XPS spectrum of OEG-NPEOC-APTES after exposure at different dose under 244 nm laser.

Figure 4.3 shows the variation in the NO_2/NH_2 ratio with dose. The ratio may be seen to decrease with increasing exposure. Figure 4.3 also shows that the wavelength of the laser affects the deprotection rate of OEG-NPEOC-APTES. At the shorter wavelength (244 nm) the rate of deprotection is higher than at the longer wavelength (325 nm), which suggests that high power laser leads to fast deprotection of OEG-NPEOC-APTES. In Figure 4.3 (a), it's observed that before exposure dose of 5 Jcm^{-2}, the ratio of nitro groups and amino groups decreases quickly from 0.37 to 0.18 while after exposure dose of 5 Jcm^{-2}, the ratio still decreases but more slowly. These results suggest that there may

be a competing reaction occurs when exposed by 244 nm laser, which may lead to the conversion of the nitro groups to a nitroso groups rather than cleavage of the C-N bond in the carbamate groups.

(a)

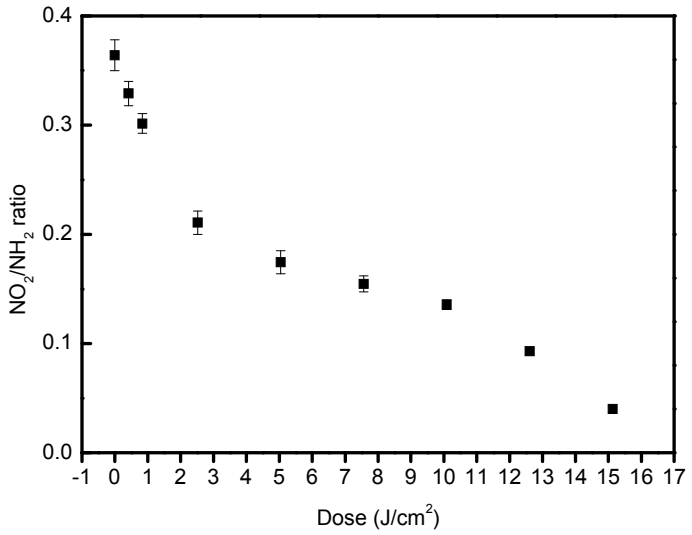

(b)

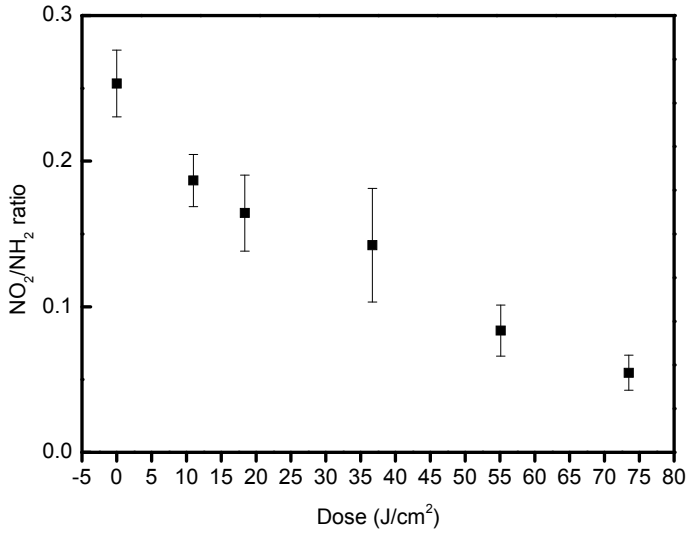

Figure 4.3 Variation in the NO_2/NH_2 ratio with dose after exposure at (a) 244 nm and (b) 325 nm.

4.3.3 Micrometre-scale and nanometre-scale patterns of OEG-NPEOC-APTES

4.3.3.1 Mask-based UV lithography

Micrometre-scale patterns were produced by exposing the OEG-NPEOC-APTES films to UV light through a 1000 mesh grid mask. In the exposed areas the OEG-NPEOC protecting groups were removed to yield amine groups on the surface. Figure 4.4 shows a friction force image of a microscale pattern, which was made by exposure to a dose of 9.78 Jcm^{-2} at 244 nm. Square regions exhibiting darker contrast are observed, corresponding to regions that were exposed through the mask. These data suggest that the exposed area terminated with amine groups yield a lower friction force. Alang Ahmad et al. measured and quantified the friction coefficient values of OEG-NPEOC-APTES films following exposure to UV light. They observed that the normalized coefficient of friction decreased after exposure, which means that the rate of energy dissipation was lower. The bars (bright contrast) were masked during exposure. The bright contrast reflects a strong interaction between silicon nitride tip and OEG regions. The size of the squares is 20 µm x 20 µm.

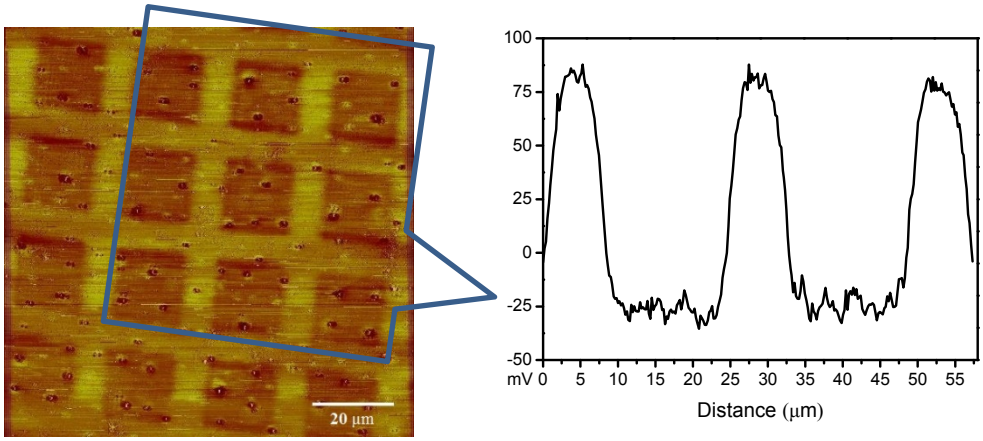

Figure 4.4 AFM friction force image (left) and its cross section (right) of microscale patterns formed by exposure of OEG-NPEOC-APTES at 244 nm through a mask with a dose of 9.78 Jcm^{-2}.

4.3.3.2 Interference lithography (IL)

Nanoscale patterns of OEG-NPEOC-APTES were made through IL using 244 nm laser. Figure 4.5 shows friction force images of IL patterns with different dimensions formed by varying the exposure dose and the angle 2θ between the mirror and the sample in the interferometer. Bands of dark contrast correspond to the amine terminated regions formed where the sample was exposed to a maximum in the interferogram. If the angle between the sample surface and mirror was set to be 10°, a linear pattern with a period of ca. 700 nm was produced (Figure 4.5a and b), while if the angle was set to be 20°, a linear pattern with a period of ca. 380 nm was produced (Figure 4.5c and d). FWHM of the features varies with both the rotation angle and the exposure. Comparing the feature sizes in Figure 4.5 (a) (b) and Figure 4.5 (c) (d), it can be seen that the FWHM of the dark bands in the exposed areas decreases as the angle between the sample and mirror increases. Feature sizes also changed depending on the exposure at a fixed rotation angle. The FWHM of dark bands in Figure 4.5 (a) was ca. 300 nm when the exposure was 6 Jcm^{-2}, decreasing to ca. 250 nm when the exposure was 4 Jcm^{-2} (Figure 4.5b). The FWHM of the dark bands in Figure 4.5 (c) decreased from 170 nm to 155 nm when the exposure decreased from 6 Jcm^{-2} to 4 Jcm^{-2} (Figure 4.5d). These results suggest that several factors will affect the FWHM of features prepared by IL. In order to obtain the features with certain size, it would be better to try different conditions.

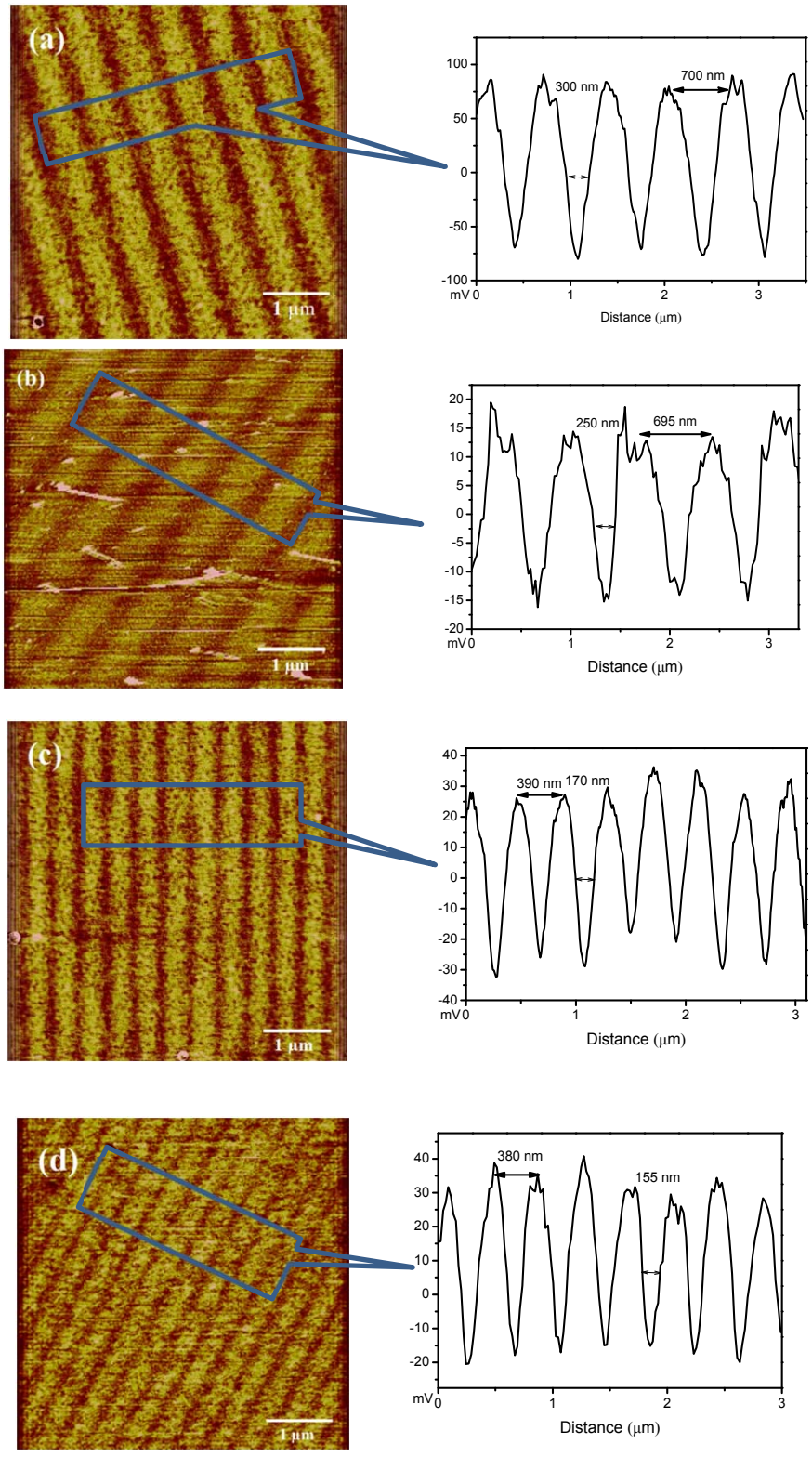

Figure 4.5 AFM friction force images (left) and their cross sections (right) of nanoscale patterns of OEG-NPEOC-APTES made by IL with different rotation angle and exposure dose: (a) 10°, 6 Jcm^{-2}; (b) 10°, 4 Jcm^{-2}; (c) 20°, 6 Jcm^{-2} and (d) 20°, 4 Jcm^{-2}.

4.3.3.3 Scanning near field photolithography (SNP)

Patterns were also fabricated using SNP. Figure 4.6 shows the friction force images of parts of the resulting patterns, in which linear structures are observed clearly. The darker contrast in these features results from the exposure of amine groups after localised deprotection by interaction of the NPEOC protecting group with the near field. Exposure to UV light at a slow scan speed of 1 μm s^{-1} yielded lines with the FWHM of ca. 500 nm (Figure 4.6a). Narrower lines with FWHM of ca. 350 nm were observed when using a faster scan speed of 1.5μm s^{-1} (Figure 4.6b). The results indicate that the FWHM of features prepared by SNP depends on the scan speed, or more precisely, the exposure time.

(a)

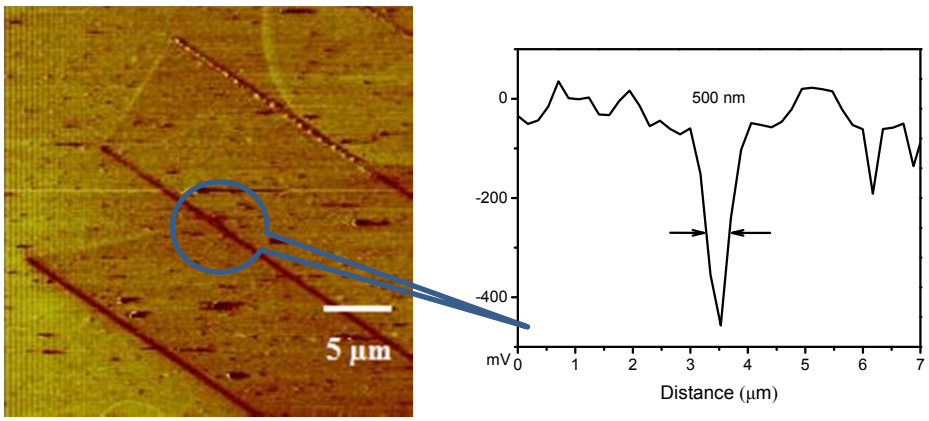

(b)

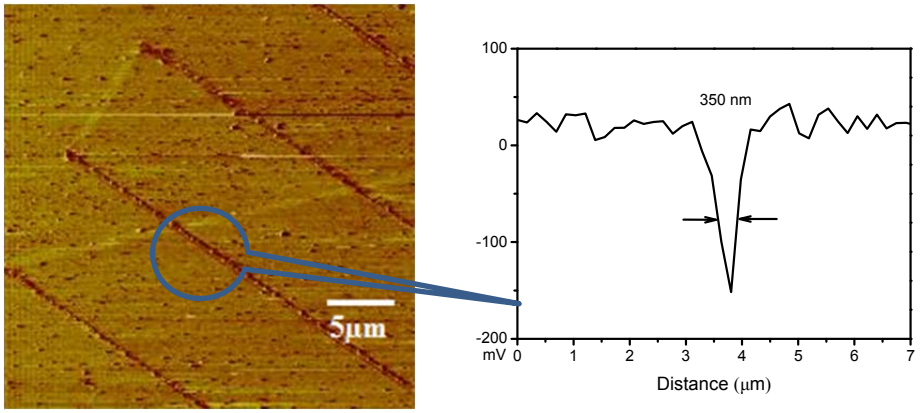

Figure 4.6 AFM friction force images (left) and the cross sectional profiles (right) of nanoscale patterns of OEG-NPEOC-APTES made by SNP at a scan speed of (a) 1 μm s^{-1} and (b) 1.5μm s^{-1}.

4.3.4 Single protein patterning

4.3.4.1 Protein attachment affected by exposure dose

Protein patterns were formed by immersion of patterned OEG-NPEOC-APTES films in solutions of the desired protein immediately after UV exposure. As the dose increases, the surface becomes increasingly deprotected, and a higher fraction of the adsorbates are amine terminated leading to increased rates of protein adsorption. When OEG-NPEOC-APTES patterns were prepared by exposure at different doses, protein patterns with different densities could be obtained. Figure 4.7 illustrates fluorescence images of YFP patterns (Figure 4.7a) and their cross sections (Figure 4.7b) after different exposures. For an exposure dose of 4.6 Jcm^{-2}, the pattern is clearly seen although there is not a strong contrast difference (ca. 40 au) between masked and exposed regions observed in the cross section. When the exposure dose is increased to 6 ~ 9 Jcm^{-2}, the protein densities in the exposed regions increase, giving rise to a greater contrast difference (ca. 80 au). When the exposure dose is increased to 11.5 Jcm^{-2}, the contrast difference becomes stronger (ca. 120 au). Squares with very bright yellow fluorescence can be observed, which indicate high protein densities in the exposed regions. Meanwhile, almost no fluorescence is observed in the unexposed area (bars). The large difference in the fluorescence intensity between the exposed and unexposed regions observed in the cross section demonstrates the high protein resistance of the ethylene glycol chain in OEG-NPEOC-APTES. The immobilization of YFP on exposed regions of OEG-NPEOC-APTES was estimated from the normalized fluorescence intensity, which was the difference in the value of YFP fluorescence intensity on the exposed regions (squares) and the unexposed regions (bars). In Figure 4.7(c), the fact that the density of attached proteins increases with the exposure indicates that the amount of protein attachment depends on the degree of deprotection of OEG-NPEOC-APTES.

(a)

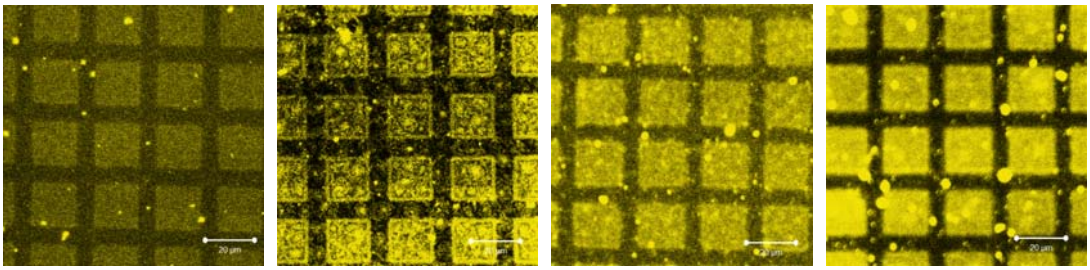

(b)

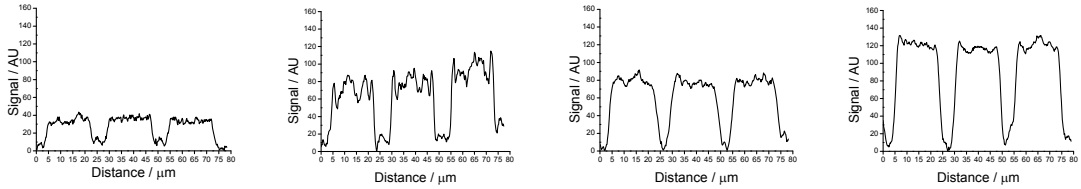

(c)

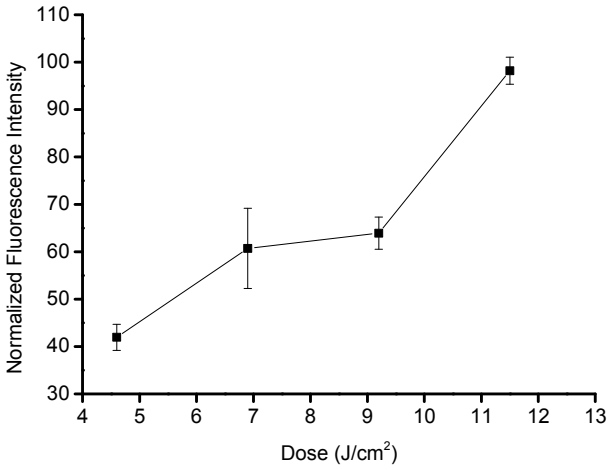

Figure 4.7 (a) Confocal fluorescence images and (b) their cross sections of YFP microscale patterns on OEG-NPEOC-APTES made at different exposure dose (From left to right: 4.6 Jcm^{-2}, 6.9 Jcm^{-2}, 9.2 Jcm^{-2}, 11.5 Jcm^{-2}). (c) Normalized fluorescence intensity as a function of exposure dose.

4.3.4.2 Microscale single protein patterns

Microscale single protein patterns were prepared by attaching proteins onto microscale patterns formed in OEG-NPEOC-APTES by UV lithography. Figure 4.8 shows confocal fluorescence images of patterns formed from a number of different proteins including GFP, YFP, CPCA, Anti-sheep IgG FITC conjugate (IgG), Streptavidin cy3 conjugate

(STA cy3), Streptavidin Alex Fluor 750 (STA 750), Atto 425 Streptavidin (STA 425), Atto 488 Streptavidin (STA 488) and Atto 655 Streptavidin (STA 655). The images of proteins are organised in order of their emission wavelength, which have the range from 450 nm to 800 nm. The emission range for each protein is shown under the micrographs. Clear fluorescence from the squares implies the good attachment of proteins onto the exposed areas, and the dark bars emphasized the protein resistance of the unexposed areas. The sizes of the squares to which protein is attached are ca. 20 μm x 20 μm. In the micrographs, the emission wavelengths of STA 655 and STA 750 have no overlap with other proteins so that their fluorescence can be separated easily by the filters in confocal microscope. Besides, IgG and STA 488 were identified to be good choices for the formation of multiple protein patterns with STA 655 and STA 750.

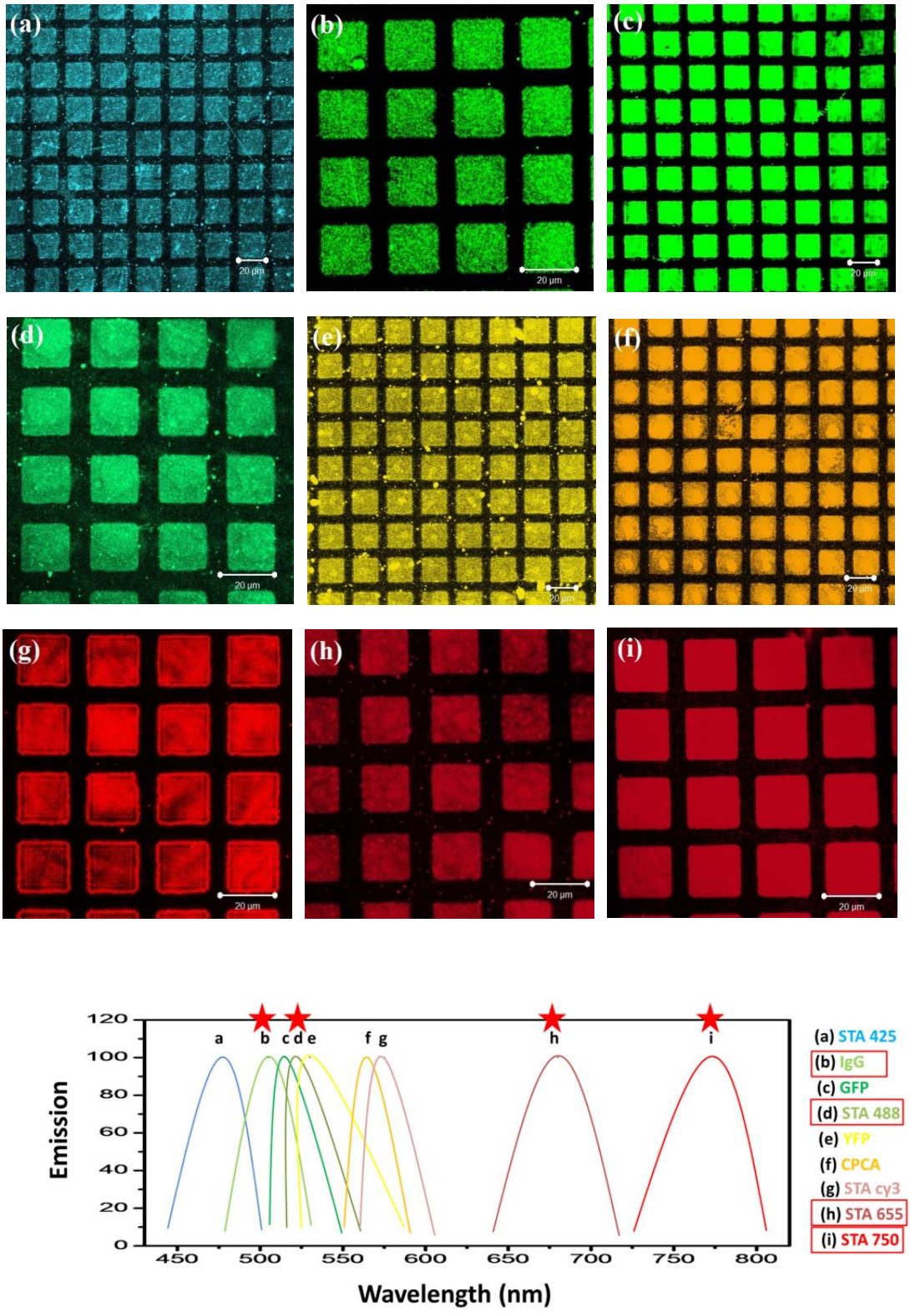

Figure 4.8 Confocal fluorescence images of microscale patterns of (a) STA 425; (b) IgG; (c) GFP; (d) STA 488; (e) YFP; (f) CPCA; (g) STA cy3; (h) STA 655; (i) STA 750 arranged in order of their emission wavelength.

4.3.4.3 Nanoscale single protein patterns

Large area nanoscale patterning of proteins was achieved by attaching proteins to nanoscale patterns formed in OEG-NPEOC-APTES films by interference lithography (IL). After UV exposure, the samples were derivatised with glutaraldehyde and then immersed in the protein solutions, leading to non-specific adsorption on regions where the adsorbates had been deprotected. Figure 4.9 shows confocal fluorescence images of GFP, STA 655 and YFP nanoscale patterns. Fluorescence of the linear structures coming from GFP, STA 655 or YFP is observed clearly in the exposed area of Figure 4.9 (a), (b) and (c) respectively. The period of GFP and STA 655 patterns made at rotation angle of 10^{o} and exposure dose of 6 Jcm^{-2} is ca. 700 nm. The period of YFP patterns made at rotation angle of 20^{o} and exposure dose of 4 Jcm^{-2} is ca. 400 nm.

(a) (b) (c)

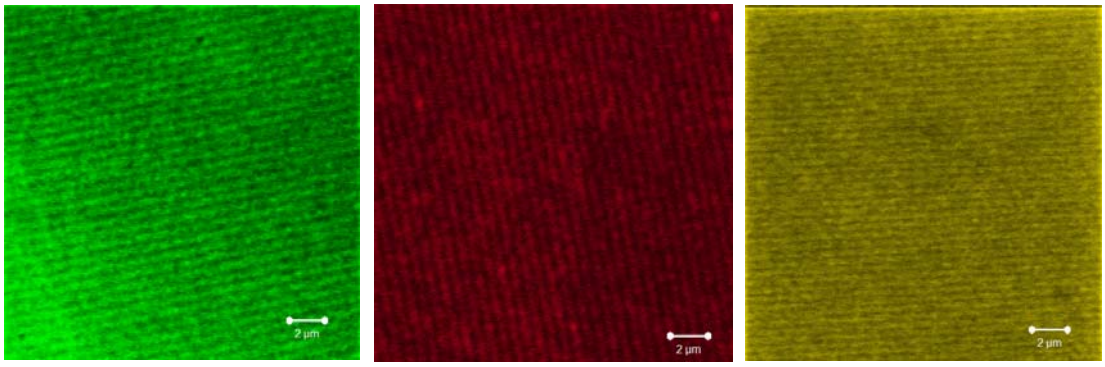

Figure 4.9 Confocal fluorescence images of IL patterns of (a) GFP and (b) STA 655 made at dose of 6 Jcm^{-2} and angle of 10^{o}; (c) YFP made at dose of 4 Jcm^{-2} and angle of 20^{o}.

Nanoscale patterns of membrane proteins like LH1 and LH2 were also prepared by IL. AFM height images and their cross sectional profiles are shown in Figure 4.10 for nanoscale patterns of LH2 prepared by IL under different conditions. Comparing those images the period of protein lines is only affected by the rotation angle. When the rotation angle was 10^{o}, the period was 560 nm. When the angle was increased to 20^{o} and

30^{o}, the period decreased to 420 nm and 300 nm respectively. For a fixed angle, the period was also fixed but the FWHM of the protein lines decreased when the exposure was reduced. However, the continuity of all the LH2 lines was good in all the images. The cross sections also tell us the thickness of LH2 on substrates measured in air is around 4 nm. LH2 is a cylindrical membrane protein complex with an external diameter of 7 nm and height of 6 nm.[99,187] Comparing with the known dimensions, the height of LH2 measured in air appears to be less. A possible reason is that the photodeprotection of OEG-NPEOC-APTES films will remove ca. 2 nm of material from surface, leading to an apparent decrease in height of proteins attached to the exposed regions. When the 2 nm difference is added to the measured 4 nm height, it gives a total height of ca. 6 nm, which is in agreement with the expected height of LH2. Escalante et al.[78] reported a similar height of LH2 measured from AFM images of LH2 complexes attached onto patterned substrates, which were obtained in liquid. The data support our results and indicate that analysis in air has little effect on the analysis results of protein height. From the AFM images, a high density arrangement of proteins was observed without significant height differences. It suggests that the protein complexes may self-orient on the surface in a quasi-oriented fashion. This observation is supported by the structure of membrane protein which has two separated hydrophilic charged regions.[78]

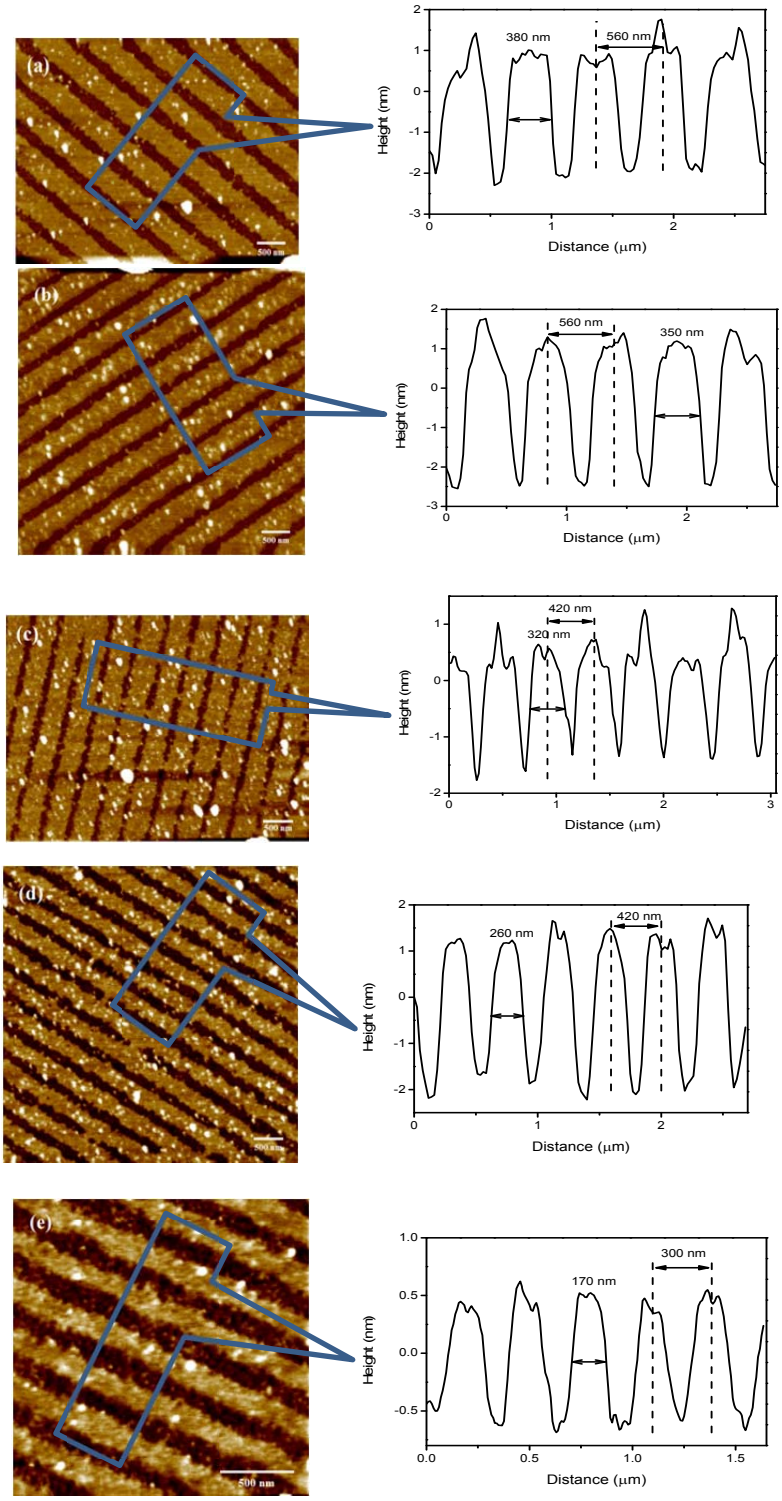

Figure 4.10 AFM height images (left) and their cross sections (right) of LH2 nanopatterns prepared by IL at different conditions: (a) Angle 10^{o}, Dose = 6 Jcm^{-2}; (b) Angle 10^{o}, Dose = 4 Jcm^{-2}; (c) Angle 20^{o}, Dose = 6 Jcm^{-2}; (d) Angle 20^{o}, Dose = 4 Jcm^{-2}; (e) Angle 30^{o}, Dose = 4 Jcm^{-2}.

Nanoscale patterns of proteins were also produced by scanning near field photolithography (SNP). The near field probe was traced across the surface leading to deprotection of the adsorbates. The sample was then immersed in as solution of protein and imaged by confocal microscopy. Figure 4.11(a) and (b) show YFP and CPCA nanopatterns. In contrast with the dark background, bright fluorescence is observed from the six protein lines, which confirms the immobilization of proteins onto the deprotected regions. The low background fluorescence observed in non-exposed regions indicates that little non-specific adsorption of proteins was occurred there. The two triangles pattern of IgG in Figure 4.11(c) and the dragon pattern of GFP in Figure 4.11(d) show the ability of SNP as a tool to produce more complicated structures. The dark region in Figure 4.11(d) is the gold finder-grid, where the fluorescence was quenched. The FWHM of YFP, CPCA, IgG and GFP lines are measured as approximate 800 nm, 700 nm, 600 nm and 500 nm respectively from their fluorescence. The exact FWHM of protein lines should be smaller than those values measured from fluorescence.

(a) (b)

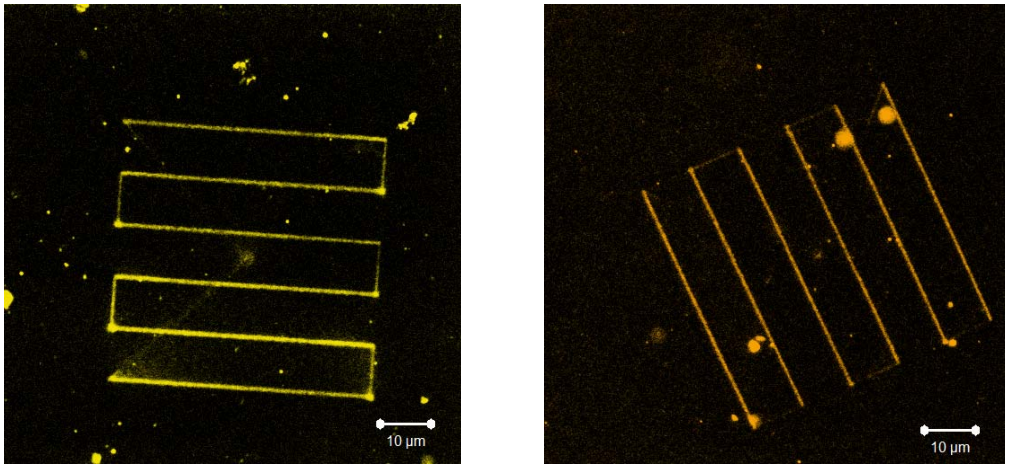

(c) (d)

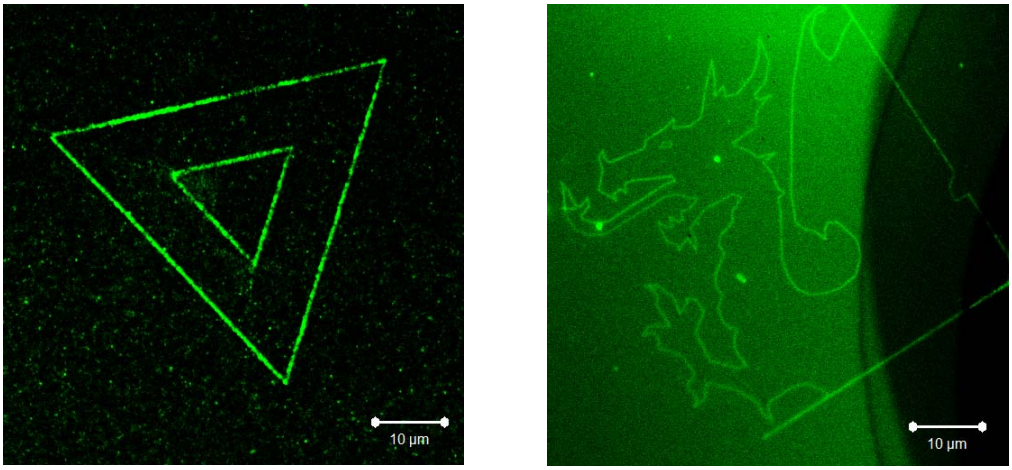

Figure 4.11 Confocal fluorescence images of SNP patterns of (a) YFP; (b) CPCA; (c) IgG and (d) GFP.

4.3.4.4 Microscale patterns of two proteins

OEG-NPEOC-APTES samples were exposed first through a mask. This enabled attachment of the first protein to the squares. The samples were then exposed without a mask, leading to the attachment of the second protein to the bars. Figure 4.12 illustrates confocal fluorescence images of microscale patterns of two proteins. Clear colour contrast demonstrates that two kinds of proteins had been well attached onto the specified regions. In Figure 4.12 (a), the protein in the square with red fluorescence is

STA 750 while the one in the bar with green fluorescence is Neutravidin. In Figure 4.12 (b), the red one in the square is STA 655 and the green protein in the bar is IgG. In Figure 4.12 (c), STA 655 is in the square and Neutravidin is in the bar.

IgG emits light in the range 500 nm to 550 nm and Neutravidin emits in almost the same range. Both of them can be excited by an argon laser (488 nm). However, STA 655 and STA 750 have emission maxima at significantly longer wavelengths, of 680 nm and 775 nm respectively. They can be excited by an HeCd laser (633 nm). Using filters BP 500-550 IR and BP 650-710 IR in the confocal microscope, the emission fluorescence of IgG and Neutravidin can be separated from that of STA 655 and STA 750 into different channels. In Figure 4.12 the images on the left show the emission fluorescence (Red) of either STA 655 or STA 750 from filter BP 650-710 IR while the ones in the middle show the emission fluorescence (Green) of either IgG or Neutravidin from filter BP 500-550 IR. The images on the right show the overlaid fluorescence from two different proteins. Very little overlap is observed, confirming that the two proteins have been successfully immobilized onto the squares and bars respectively.

(a)

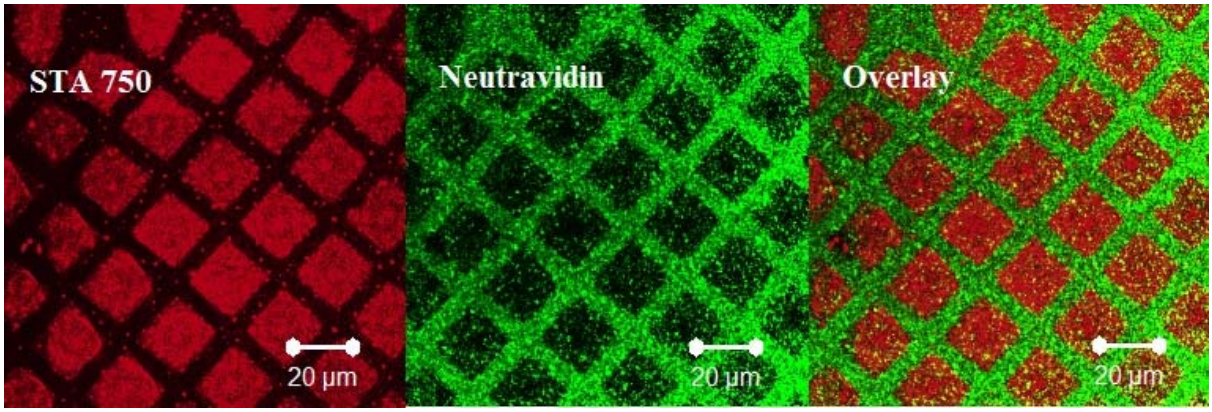

(b)

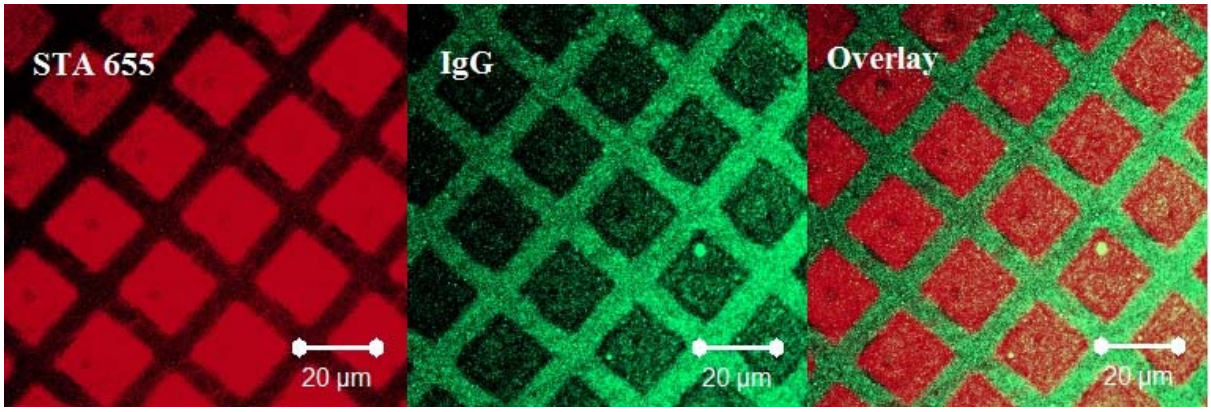

(c)

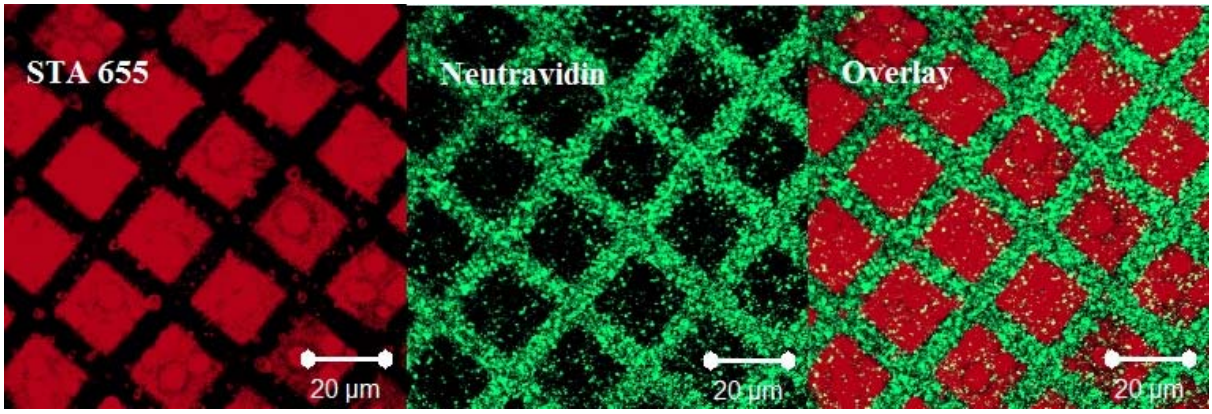

Figure 4.12 Confocal fluorescence images of (a) STA 750 and Neutravidin; (b) STA 655 and IgG and (c) STA 655 and Neutravidin microscale patterns.

4.3.4.5 Nanoscale patterns of multi proteins

Nanoscale multi-protein patterns were produced by SNP. Figure 4.13 shows the confocal fluorescence images of single, two, three and four protein SNP patterns. In

Figure 4.13 (a), a green triangle is observed that has been formed by SNP followed by the adsorption of GFP. In Figure 4.13 (b), an STA 655 pattern of 8 lines structure was overlaid on the green triangle structure of IgG to form the two proteins pattern. In Figure 4.13 (c), three proteins IgG, STA 655 and STA 488 which have the structures of two triangles, 8 lines and triangle respectively, overlap with each other to form a three-protein pattern. Similarly, four proteins IgG, STA 655, STA 488 and STA 750 which have the structures of triangle, circle, 8 lines and two triangles respectively in Figure 4.13 (d) form the pattern of four proteins. The challenge to produce multi-protein patterns by SNP is how to find the location of former patterns and over-write a new one on them. Either a finder-grid structure or a triangle scratched on the substrate was used as an identifying feature to facilitate registry of the probe. Under the microscope, the cantilever was moved to the exact position of former patterns and then SNP was carried out at the same region once more. A different protein was adsorbed following each lithography step. In Figure 4.13 (b) the green fluorescence of IgG comes from filter BP 500-550 IR while the red fluorescence of STA 655 comes from filter BP 650-710 IR in confocal microscopy. Clear colour contrast indicates the two-protein pattern was well fabricated. However, the emission wavelengths of IgG and STA 488, or STA 655 and STA 750, have lots of overlap so that filters cannot separate them completely. In Figure 4.13 (c) and (d), only the red fluorescence from STA 655 was separated while other structures have similar green colour. Even though only two colours were observed, well-defined structures of multiple different proteins were obtained successfully. The FWHM of protein lines in the fluorescence images is ranged from 300 nm to 800 nm.

(a) (b)

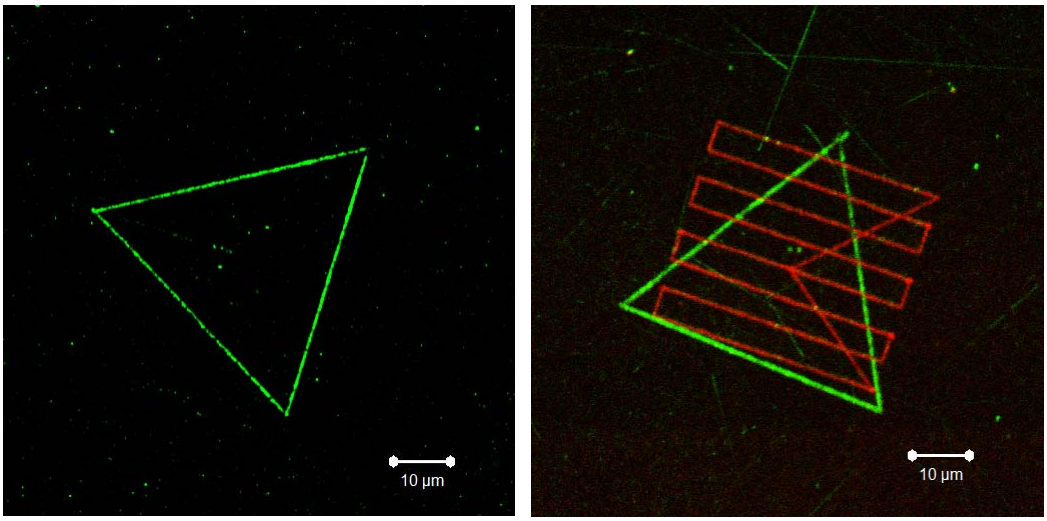

(c) (d)

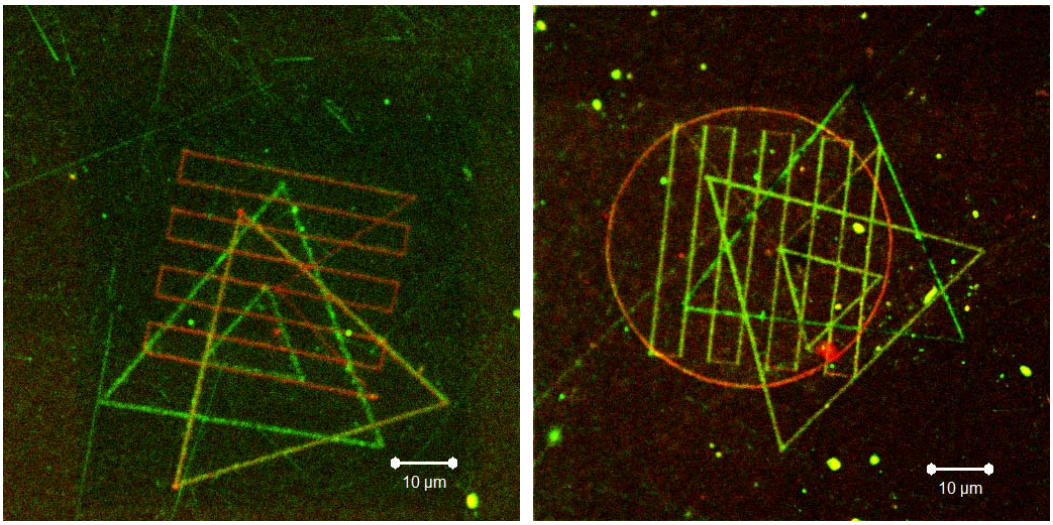

Figure 4.13 Confocal fluorescence images of multi proteins SNP patterns: (a) triangle-IgG; (b) triangle-IgG, 8 lines-STA 655; (c) two triangles-IgG, 8 lines-STA 655, triangle-STA 488; (d) triangle-IgG, circle-STA 655, 8 lines-STA 488, two triangles-STA 750.

Figure 4.14 shows AFM height and phase images of patterns formed by the sequential patterning of two membrane proteins LH1 and LH2. Protein patterns in height images are not observed very clearly due to the small feature size and the rough surface on nanometre length-scales. Attachment of proteins onto exposed regions of

OEG-NPEOC-APTES films may also reduce the height of proteins because the photodeprotection will remove approximately 2 nm of material from the surface. However, the protein patterns in phase images are shown clearly. Corresponding to the patterns in height images, the protein patterns are brighter than the other regions in phase images. This suggests that higher rate of energy dissipation has occurred in the protein attached areas. In Figure 4.14 (a), the triangle structure is formed by attachment of LH1 and the two triangle structure is formed by adsorption of LH2. The phase image on the right magnifies the crossing linear structure of these two membrane proteins, from which the overlap part of LH1 and LH2 is observed clearly. From the cross section, the FWHM of LH2 lines is 430 nm and that of LH1 lines is 200 nm. In Figure 4.14 (b), the 8 lines structure is LH1 pattern and the triangle structure is LH2 pattern. Phase image on the right magnifies the crossing part of LH1 and LH2 patterns. From the cross section, the FWHM of LH2 lines is 340 nm and that of LH1 lines is 300 nm.

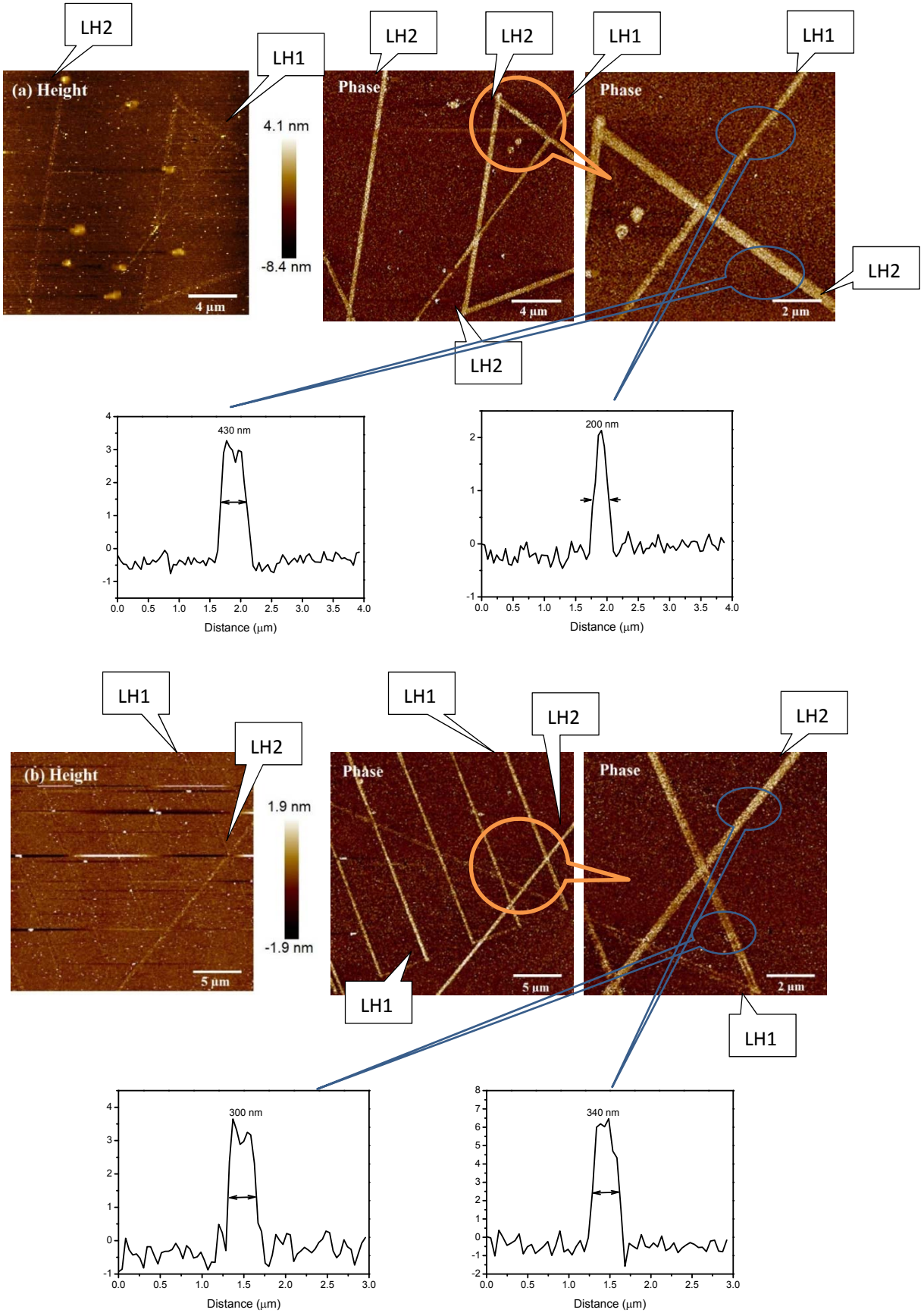

Figure 4.14 AFM Height and phase images of two membrane proteins SNP patterns: (a) two triangle-LH2, triangle-LH1; (b) triangle-LH2, 8 lines-LH1.

4.4 Conclusions

Protein resistant films have been formed by adsorption of OEG-NPEOC-APTES onto silicon, glass and quartz substrates. The deprotection rate of OEG-NPEOC-APTES under 244 nm or 325 nm UV laser had been achieved using the ratio of the NO_2 and NH_2 peaks in the XPS N1s spectra. AFM friction images revealed the formation of Microscale and nanoscale patterns of OEG-NPEOC-APTES that can immobilize biomolecules like proteins. Microscale and nanoscale patterns of single proteins have been successfully prepared by attaching proteins onto OEG-NPEOC-APTES patterns using glutaraldehyde. Regions functionalised by intact OEG-NPEOC-APTES showed good protein resistance with less non-specific adsorption. Furthermore, multi-protein patterns had been successfully made through second exposure by UV lithography or multi exposure by SNP and following attachment of different proteins. Confocal fluorescence images showed that up to four proteins' nanoscale patterns had been achieved at first time. Nanoscale patterns of membrane proteins LH1 and LH2 were also well fabricated on OEG-NPEOC-APTES SAMs by SNP using glutaraldehyde as cross linker. Further studies on the activity of these proteins and then the energy transfer between them are in progress.

Chapter 5 Preparation of NTA Functional Surfaces and Site-Specific Attachment of Histidine-Tagged Protein onto Microscale and Nanoscale Structures

5.1 Introduction

Two-dimensional assemblies of proteins are important in many biological applications including studies of cellular events[188-190], biosensors[191,192] and diagnostic systems[193,194]. In fundamental investigations of membrane protein function, spatial control over protein organisation is desirable[195]. Because the transport and catalytic functions of membrane proteins are usually vectorial in nature, controlled and oriented immobilization of proteins is important in practical applicability.[47,196] However, organizational control of proteins on sub-micrometer length scales remains extremely challenging. The development of biochips with site-specific protein patterns has been slow consequently.[21]

Recently, two affinity capture methods for the control of protein organization have been used widely by biochemists.[42] One is the biotin-mediated protein immobilization, which was firstly described by Bayer and Wilchek.[38] However, this interaction is quasi irreversible. A reversible affinity capturing would provide not only the homogeneous and oriented attachment of protein but also the possibility of detaching protein and then reusable surfaces. Another affinity immobilization using specific chelating interaction between NTA and his-tagged proteins via transition metal ion, usually Ni^{2+}, could offer a great solution for this purpose.[50] NTA is usually covalently bound to the surfaces and then loaded with Ni^{2+}. Proteins with a histidine tag at the C- or N- terminus can be bound to the surfaces through the coordination of the nickel ion with two valences occupied by two imidazole groups from His-tag and the other four occupied by the ligands from NTA molecule. The use of competitive agents like imidazole or EDTA could readily replace the His-tagged proteins so the interaction is reversible.[48,197]

Protein patterns are produced by a variety of techniques like nanoimprint lithography[198], micellar nanolithography[199], electron beam lithography[76], dip-pen nanolithography[72,200]

and near-field lithography[104]. A lot of progress has been reported but simple and generic methodologies are necessary. Surface chemical methods that could control the architecture of the biological interface are an essential part of such strategies and the control of non-specific adhesion is of primary importance. Oligo(ethylene glycol) (OEG) derivatives like OEG-terminated monolayers, poly(ethylene glycol) and poly(oligoethylene glycol methacrylate) brushes have been widely used for protein resistance[74,201,202].

A photosensitive silane OEG-NPEOC-APTES, and its potential for the manipulation of proteins at micrometer and nanometer scales, have been described in Chapter 4. This molecule consists of an aminosiloxane (APTES) that is protected by a protein-resistant OEG and photocleavable 2-nitrophenylethoxycarbonyl (NPEOC) group.[68] Here we describe an approach that is based around the use of OEG-NPEOC-APTES to enable the spatially selective fabrication of specific protein-binding surface sites (Scheme 5.1). The derivatization of aminobutylnitrilotriacetic acid (ABNTA) to regions of an OEG-NPEOC-APTES film that has been selectively deprotected by UV exposure was carried out, using glutaraldehyde as a simple bifunctional linker. High quality patterns of His-tagged GFP and CPCA were prepared through His-tagged site-specifically bound onto the NTA/Ni^{2+} functionalised structures. Ellipsometry and fluorescence measurements were utilized to demonstrate the efficiency of patterning and of site-specific binding of His-tagged proteins at micrometer and nanometer length scales.

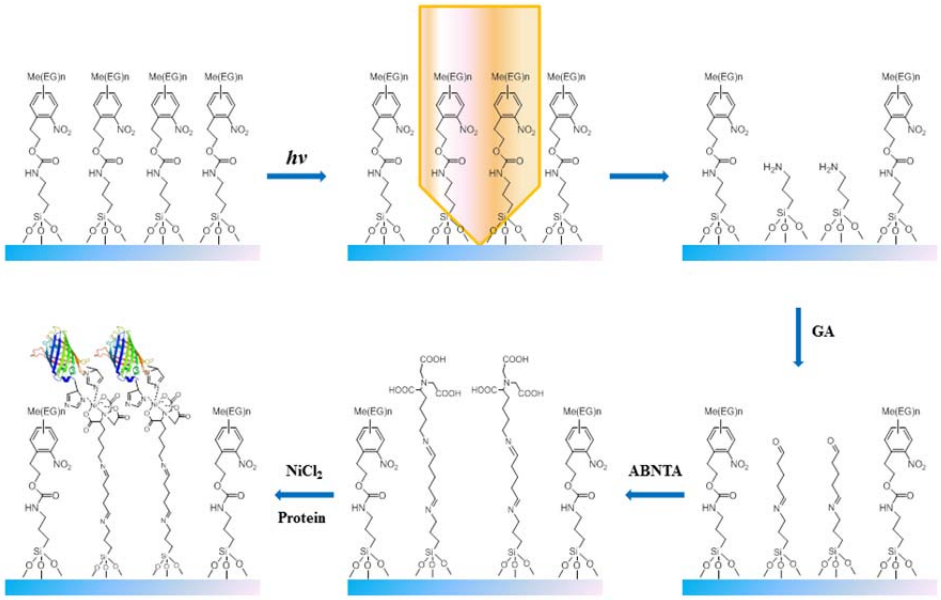

Scheme 5.1 Schematic representation of the preparation process of NTA/Ni^{2+} functionalized OEG-NPEOC-APTES patterns and site-specific attachment of His-tagged protein.

5.2 Experimental

5.2.1 Materials

Sulfuric acid ((1.83 S.G. 95+ %), hydrogen peroxide solution (100 vol. 30+ %), ammonia solution (S. G. 0.88, 35%) and toluene (HPLC grade) were supplied by Fisher Scientific (Loughborough, UK) and used as received. Ethanol (absolute) and glutaraldehyde solution (GA, Grade II, 50% in water) were obtained from VWR international (Lutterworth, UK). N-(5-amino-1-carboxypentyl)iminodiacetic acid (ABNTA) was purchased from Dojindo Molecular Technologies (Munich, Germany). Nitrilotriacetic acid functional thiol ($HS\text{-}C_{11}\text{-}(EG)_3\text{-}NTA$) was purchased from Prochimia Surfaces (Sopot, Poland). (3-Aminopropyl) triethoxysilane (APTES, 99%) was supplied by Sigma-Aldrich (Poole, UK). PBS buffer solution (pH=7.4) was prepared from tablets (Sigma-Aldrich). 2-nitrophenylethoxycarbonyl protected aminopropyltriethoxysilane (OEG-NPEOC-APTES) was synthesized by AF ChemPharm Ltd (Sheffield, UK). Histidine-tagged (His-tagged) GFP and CPCA purified through affinity purification were provided by Dr M. Carton (Department of molecular biology and biotechnology). Silicon wafers (reclaimed, p-type, <100>) were supplied by Compart Technology (Tamworth, UK). Quartz slides (50mm x 25mm x 1mm) were supplied by Agar Scientific Ltd (Stansted, UK) and glass cover slips (20 mm x 60 mm) were supplied by Menzel-Gläser (Braunschweig, Germany).

5.2.2 Surface chemistry of APTES

5.2.2.1 Preparation of APTES modified substrates

Clean silicon wafers, quartz or glass slides were immersed in a 10^{-2} (v/v) solution of APTES in toluene for 1 h. After reaction, the substrates were rinsed with toluene and ethanol several times and dried under a stream of nitrogen. The samples were annealed in a vacuum oven for 1 h at 120 ℃.

5.2.2.2 Preparation of NTA/Ni^{2+} functionalized APTES surfaces

Substrates modified with APTES were placed in a 25% (v/v) GA solution (pH ≈ 5) for 1

h, after which they were immersed in a 10mM ABNTA solution (pH ≈ 5) overnight to produce NTA functionalised surfaces. These surfaces were chelated with Ni^{2+} by immersion in a 500 mM $NiCl_2$ solution for 2 h. The reaction is shown in Scheme 5.2(a).

5.2.2.3 Preparation of -CF_3 tagged surfaces

The substrates modified with APTES were placed in a 25% (v/v) GA solution (pH ≈ 5) for 1 h, and then immersed in a 4% (v/v) solution of $NH_2CH_2CF_3$ in water for 3h to produce -CF_3 tagged surfaces. The reaction is shown in Scheme 5.2(b).

5.2.2.4 Preparation of HS-C_{11}-$(EG)_3$-NTA

Clean gold substrates were immersed in a 4 mM solution of HS-C_{11}-$(EG)_3$-NTA in water for 24 h. The samples were rinsed several times with deionized water and dried with N_2. The preparation process is shown in Scheme 5.2(c).

(a)

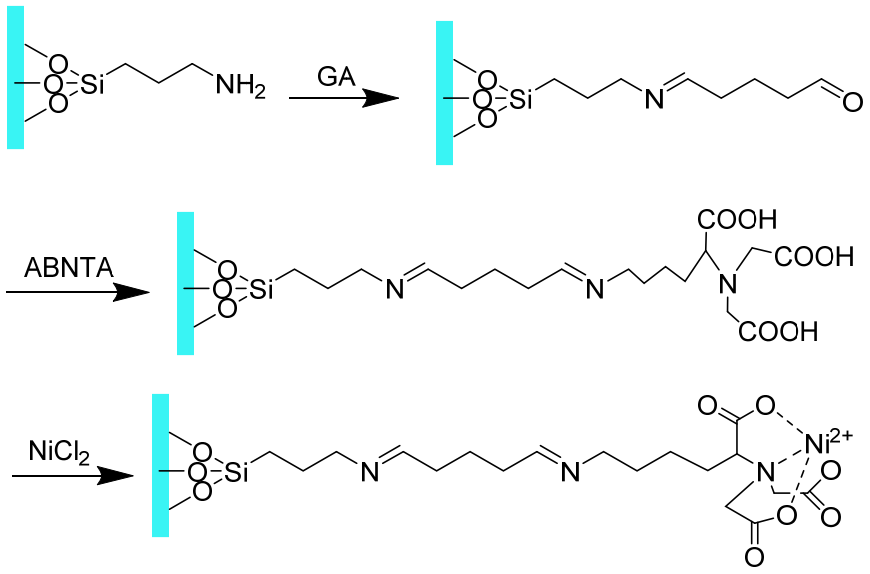

(b)

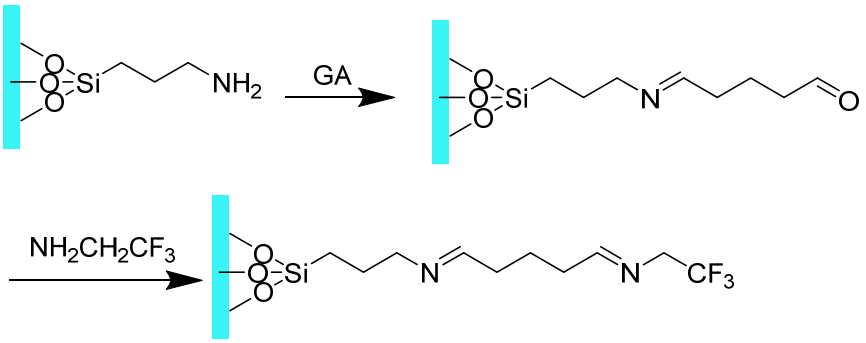

(c)

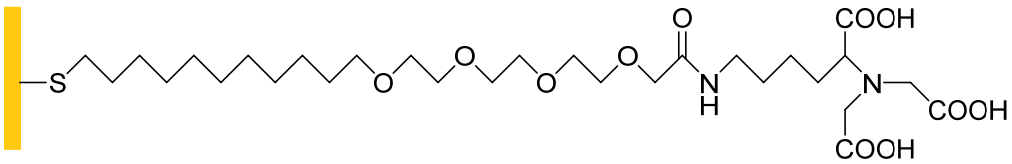

Scheme 5.2 Surface reaction scheme showing the steps of (a) APTES SAMs reacting with GA, ABNTA and $NiCl_2$ on silicon wafer; (b) APTES SAMs reacting with GA and $NH_2CH_2CF_3$ on silicon wafer; (c) HS-C_{11}-$(EG)_3$-NTA SAMs formation on gold substrates.

5.2.3 Surface chemistry of OEG-NPEOC-APTES

5.2.3.1 Preparation of NTA/Ni^{2+} functionalized OEG-NPEOC-APTES surfaces

OEG-NPEOC-APTES modified substrates were prepared as discussed in Chapter 4. They were first exposed to UV light with wavelength of 244 nm coupled to a frequency doubled argon ion laser or 325 nm coupled to a HeCd laser to remove the protecting group, after which they were immersed in PBS solution (pH = 7.4) for 30 min and dried with N_2 gas. The dose used was 14.6 J/cm^2 at 244 nm or 67.3 J/cm^2 at 325 nm to generate as many reaction sites as possible. Subsequently the substrates were put into 25% (v/v) GA solution (pH ≈ 5) for 1 h to derivatise the amine groups with GA to yield aldehyde functionalised surfaces. The substrates were then immersed in 10mM ABNTA solution (pH ≈ 5) overnight to produce NTA functional surfaces. The substrates with NTA functional surfaces were then immersed into 500 mM $NiCl_2$ solution for 2 h.

5.2.3.2 Preparation of NTA/Ni^{2+} functionalized OEG-NPEOC-APTES patterns

OEG-NPEOC-APTES modified substrates with microscale structures were fabricated by mask-based UV lithography via 244 nm laser and nanoscale structures were fabricated by scanning near field photolithography (SNP) via 325 nm laser. Then the selectively exposed regions were derivatised with NTA/Ni^{2+} as described above.

5.2.4 Site-specific attachment of His-tagged proteins

NTA/Ni^{2+} functionalized OEG-NPEOC-APTES surfaces were prepared as described above. Then those samples were immersed into his-tagged GFP or CPCA in PBS solution (pH = 7.4) overnight. His-tagged proteins were attached onto surfaces through chelation. The samples were rinsed with PBS solution (pH = 7.4) and dried with N_2 gas. In control experiment, proteins were attached onto underivatised OEG-NPEOC-APTES surfaces directly through physical adsorption.

5.2.5 Surface characterisation

5.2.5.1 XPS analysis

X-ray photo electron spectroscopy was performed using an Axis Ultra X-ray photoelectron spectrometer (Krato Analytical, Manchester, UK) equipped with delay-line-detector (DLD). It was used to analyse different functionalized APTES and OEG-NPEOC-APTES surfaces to obtain survey and high resolution spectra.

5.2.5.2 Ellipsometric thickness analysis

M-2000V ellipsometer (J. A. Woollam Co. Inc) was used to measure film thickness, using a Cauchy model. Thickness of His-tagged proteins that were attached to NTA/Ni^{2+} functionalised surfaces was measured by ellipsometry and calculated using the model in the software CompleteEASE.

5.2.5.3 Laser scanning confocal microscope analysis

Microscale and nanoscale patterns of His-tagged GFP and CPCA were characterized by LSM 510 Meta laser scanning confocal microscope (Carl Zeiss, Welwyn Garden City, UK). Fluorescence images with different sizes were obtained.

5.2.6 Evaluation of the specificity of immobilisation via NTA/Ni^{2+}/His-tag system

Site-specific protein patterning was carried out as described above. After characterization by scanning confocal microscopy, the samples were put into a 1 M imidazole solution overnight. They were then rinsed with PBS solution (pH = 7.4). Confocal microscope was used to check the protein fluorescence in the same region of each sample again. Image J software was used to calculate the fluorescence intensity of proteins before and after treatment with imidazole. At least ten regions were chosen to do the calculation and the mean and standard error of these values was reported.

5.3 Results and discussion

5.3.1 Surface preparation and Characterization

5.3.1.1 XPS analysis of NTA functionalised APTES surfaces

Deprotection of OEG-NPEOC-APTES yields APTES; the surface attachment chemistry was thus investigated first using APTES films. The reaction between GA and APTES was studied using XPS. It is known that the reaction between amine and aldehyde groups is fastest in a weakly acid environment (pH 4 to 6). XPS was used to characterize the chemical change on the surface. The XPS C1s high resolution spectra for different surfaces are shown in Figure 5.1 and the analysis results are summarized in Table 5.1. The spectrum of an APTES modified surface is fitted with two peaks: one with binding energy (BE) of 285.0 eV is attributed to C-C and another with BE of 286.6 eV is attributed to C-N. After reaction with GA, the spectrum of the APTES-GA surfaces is fitted with three peaks: 285.0 eV, attributed to C-C; 286.5 eV attributed to C-N or C=N and 288.1 eV attributed to C=O. When the aldehyde groups react with ABNTA, the spectrum of the APTES-GA-NTA surfaces is fitted with four peaks: 285.0 eV, attributed to C-C; 286.6 eV, attributed to C-N or C=N; 288.1 eV, attributed to C=O; and 289.0 eV, attributed to O-C=O. When preparing APTES surface, the experimental percentage of C-N is 18.8%. Considering the theoretical carbon species percentage is 33.3%, the APTES surface prepared may have a small amount of hydrocarbon contamination. When preparing aldehyde surfaces, a new peak corresponding to C=O species was observed. The experimental percentage of C=O is 11.7% which is quite close to the theoretical value 12.5%. It implies that almost all the amine groups have reacted with GA and been turned into aldehyde groups. When preparing NTA surfaces, another new peak corresponding to O-C=O was observed. The experiment percentage of O-C=O is 4.1%. Comparing with the theoretical value 16.7%, about one quarter of the adsorbents is derivatised by NTA.

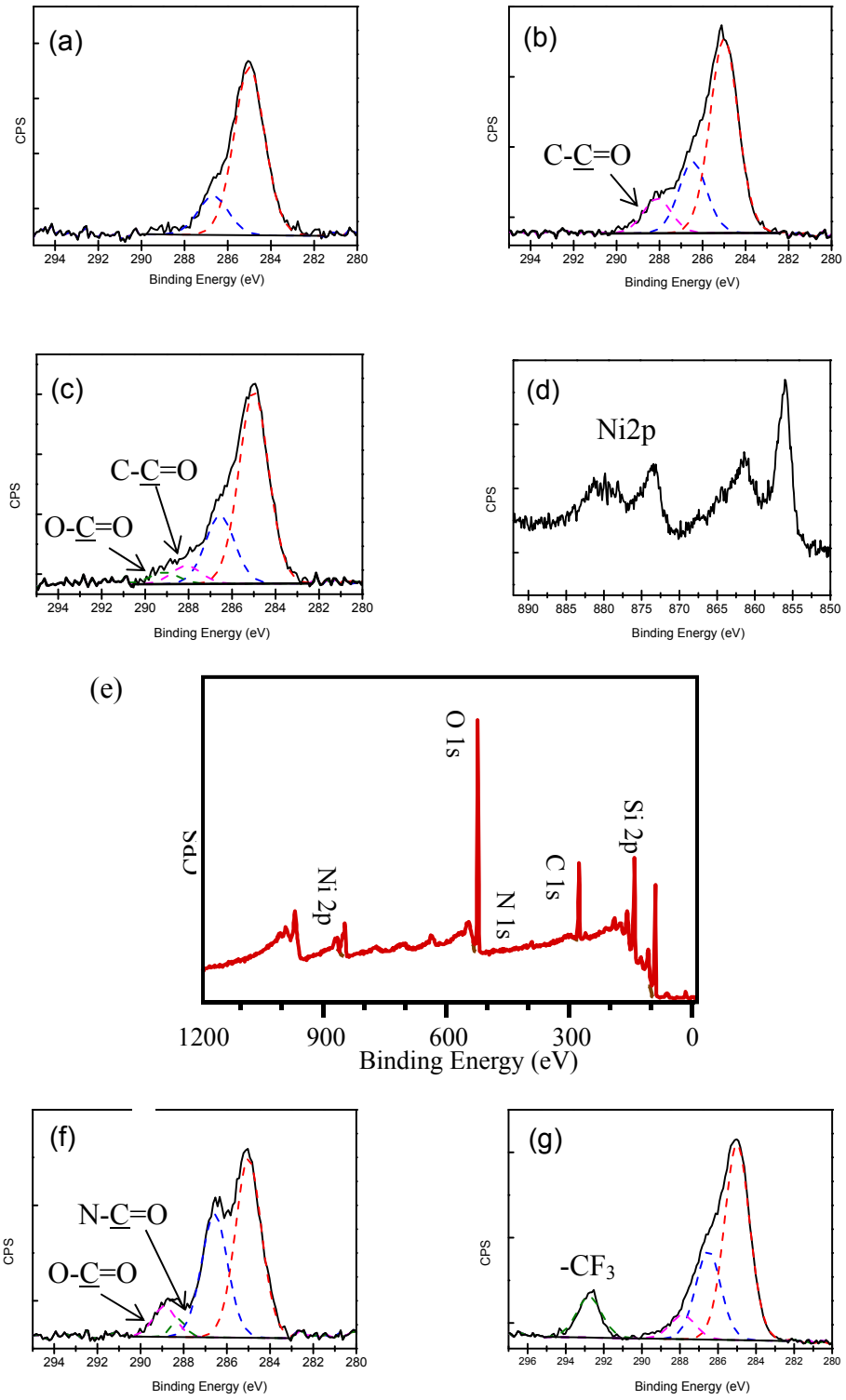

Figure 5.1 XPS C1s high resolution spectra of (a) APTES SAMs, (b) APTES + GA surfaces, (c) APTES + GA + ABNTA surfaces; XPS Ni2p high resolution spectrum of (d) NTA functional surfaces chelating with Ni^{2+}; (e) Survey spectrum of NTA functional surfaces chelating with Ni^{2+}; XPS C1s high resolution spectra of (f) HS-C11-$(EG)_3$-NTA SAMs on gold and (g) APTES + GA + $NH_2CH_2CF_3$ surfaces.

Table 5.1 Analysis of the XPS C1s high resolution spectra above

	APTES			APTES + GA			APTES + GA + ABNTA			APTES + GA + $NH_2CH_2CF_3$			HS-C_{11}-$(EG)_3$-NTA		
	BE	TP	EP	BE	TP	EP	BE	TP	EP	BE	TP	EP	BE	TP	EP
C-C	285.0 eV	66.7 %	81.2 %	285.0 eV	62.5 %	64.6 %	285.0 eV	44.4 %	66.2 %	285.0 eV	50%	56.1 %	285.0 eV	44.9 %	52.8 %
C-O; C-N; C=N	286.6 eV	33.3 %	18.8 %	286.5 eV	25%	23.7 %	286.6 eV	38.9 %	23.5 %	286.5 eV	40%	25.3 %	286.6 eV	41.4 %	36.4 %
C=O; N-C=O				288.1 eV	12.5 %	11.7 %	288.1 eV	N/A	6.3%	287.9 eV	N/A	6.9%	288.2 eV	3.4%	2.9%
O-C=O							289.0 eV	16.7 %	4.1%				288.9 eV	10.3 %	7.9%
$-CF_3$										292.8 eV	10%	11.7 %			

*BE = Binding Energy, TP = Theoretical Percentage, EP = Experimental Percentage.

To ensure that NTA species on the surfaces could coordinate with Ni^{2+}, the samples were immersed in a 500 mM $NiCl_2$ solution for 2 h and characterized by XPS. The appearance of Ni^{2+} signal in the survey spectrum (Figure 5.1e) confirmed chelation of NTA by Ni^{2+}. The experimental percentage of nickel was 1.27%, from which was concluded that the chelating efficiency of ABNTA units is ca. 0.93 Ni atoms per chelator (the theoretical value is 1).

In order to determine the positions of the characteristic peaks in XPS spectra, a SAM of HS-C_{11}-$(EG)_3$-NTA SAMs on gold was used as a reference. The C1s spectrum of the SAMs is also fit with four peaks: 285.0 eV, attributed to C-C; 286.6 eV, attributed to C-O, C-N and C-S; 288.2 eV, attributed to N-C=O ; and 288.9 eV, attributed to O-C=O. Comparison of this reference C1s spectrum (Figure 5.1f) with the one acquired for the APTES-GA-NTA surface (Figure 5.1c), reveals that they both have peaks with almost the same position for O-C=O.

The reaction between amine and aldehyde groups was also investigated by studying the

model reaction between APTES, GA and $NH_2CH_2CF_3$ using the same reaction conditions. The CF_3 group yields a clear peak with BE of 292.8 eV in C1s spectra, which is a good label in high resolution C1s spectra (Figure 5.1g). It means the reaction between amine and aldehyde works well under the weak acid environment.

From all the results above, it was deduced that NTA could be successfully immobilised by attachment of ABNTA to APTES using a GA linker.

5.3.1.2 XPS analysis of NTA functional OEG-NPEOC-APTES surfaces

The NPEOC protecting group is removed on exposure to illumination at 244 nm or 325 nm and the XPS analysis has been shown in Chapter 4. It was hypothesized that at dose of ca. 15 Jcm^{-2}, the protection will be incomplete. A small amount of intact OEG chains is left at the surface, along with amine groups, meaning that while the surface is partially protein-resistant, it is possible to use NTA-His tag reactions to immobilise proteins. NTA could be incorporated onto the exposed area by attachment to APTES through the method discussed above. XPS was used to characterize the chemical changes on the surfaces. The XPS C1s high resolution spectra for different surfaces are shown in Figure 5.2 and the compositional data are summarized in Table 5.2. The spectrum of OEG-NPEOC-APTES surface is fitted with three peaks: 285.0 eV, attributed to C-C on benzene rings and aliphatic carbons; 286.5 eV, attributed to C-O and C-N; 289.3 eV, attributed to O-C=O. After exposure, parts of the OEG-NPEOC groups had been removed, the spectrum is fitted with four peaks: 285.0 eV, attributed to C-C; 286.6 eV, attributed to C-O and C-N; 288.1 eV, attributed to C=O; and 289.0 eV, attributed to O-C=O. The experimental percentage of C-O or C-N groups was observed to decrease from 59.4% to 52.3% because that loss of OEG groups leads to a decrease in the size of the component O-C-O. The peak that appears at 288.1 eV shows that some OEG might have been turned into aldehyde (C=O) groups. After reaction with GA, the experimental percentage of C-C corresponding to peak at 285.0 eV was observed to increase to 53.8%, and the experimental percentage of C=O groups corresponding peak at 288.1 eV increased to 11.2% because of the incorporation of aldehyde groups at the

uppermosted of GA addict. After reaction with ABNTA, the experimental percentage of C-C increased further to 63.2% while that of C=O decreased to 4.2% because of the reaction between aldehyde on the surface and amine groups in ABNTA. At same time, the experimental percentage of O-C=O increased to 6.1% because ABNTA had been functionalized onto the surface. Analysis of the XPS Ni2p high resolution spectrum confirmed that NTA species on the surfaces had chelated with Ni^{2+}.

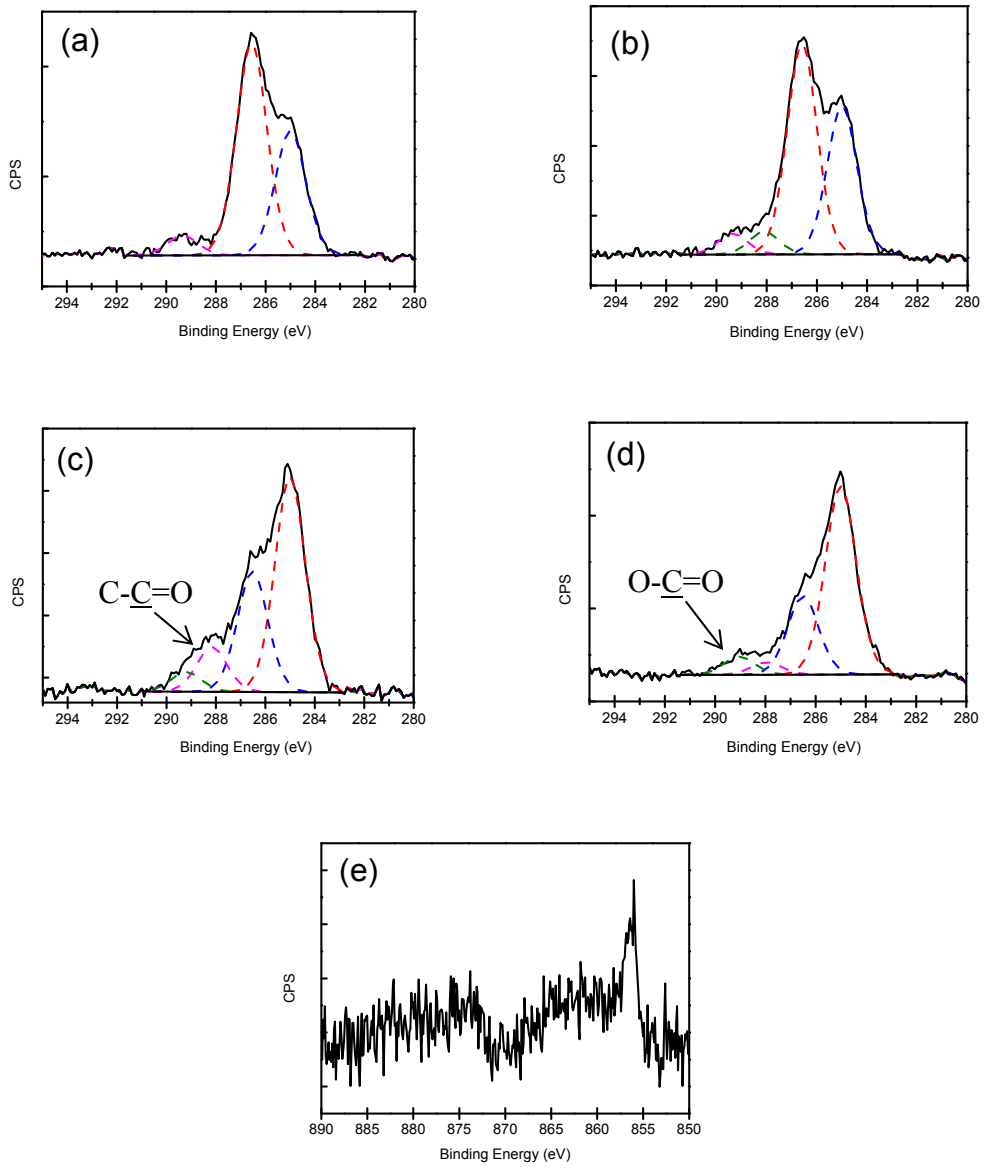

Figure 5.2 XPS C1s high resolution spectra of (a) OEG-NPEOC-APTES modified surface, (b) Surfaces (a) exposed by 244nm laser at the dose of 15 Jcm^{-2}, (c) Surface (b) reacting with GA, (d) Surfaces (c) reacting with ABNTA; XPS Ni2p high resolution spectrum of (e) NTA functional surfaces chelating with Ni^{2+}.

Table 5.2 Analysis of XPS C1s high resolution spectra above

	NPEOC		NPEOC exposed by 244nm laser		NPEOC exposure + GA		NPEOC exposure + GA + ABNTA	
	BE	EP	BE	EP	BE	EP	BE	EP
C-C	285.0eV	34.9%	285.0eV	36.8%	285.0eV	53.8%	285.0eV	63.2%
C-O; C-N; C=N	286.6eV	59.4%	286.6eV	52.3%	286.6eV	30.1%	286.5eV	26.5%
C=O			288.1eV	5.7%	288.1eV	11.2%	288.0eV	4.2%
O-C=O	289.3eV	5.6%	289.0eV	5.2%	289.3eV	4.9%	289.1eV	6.1%

*BE = Binding Energy, EP = Experimental Percentage.

These measurements were repeated for OEG-NPEOC-APTES surfaces exposed to irradiation at 325 nm. The XPS C1s high resolution spectra are shown in Figure 5.3 and the compositional data are summarized in Table 5.3. The sample was exposed to a dose of ca. 67 Jcm^{-2} and derivatised by reaction with GA and then ABNTA. The XPS C1s high resolution spectrum is shown in Figure 5.3 and the compositional analysis is shown in Table 5.3. The experimentally determined percentage of C-C increased gradually after each reaction while that of C=O increased after the reaction with GA and decreased after the binding of ABNTA. Finally the observation of a peak in the Ni2p spectrum confirmed that the surfaces could chelate with Ni^{2+}.

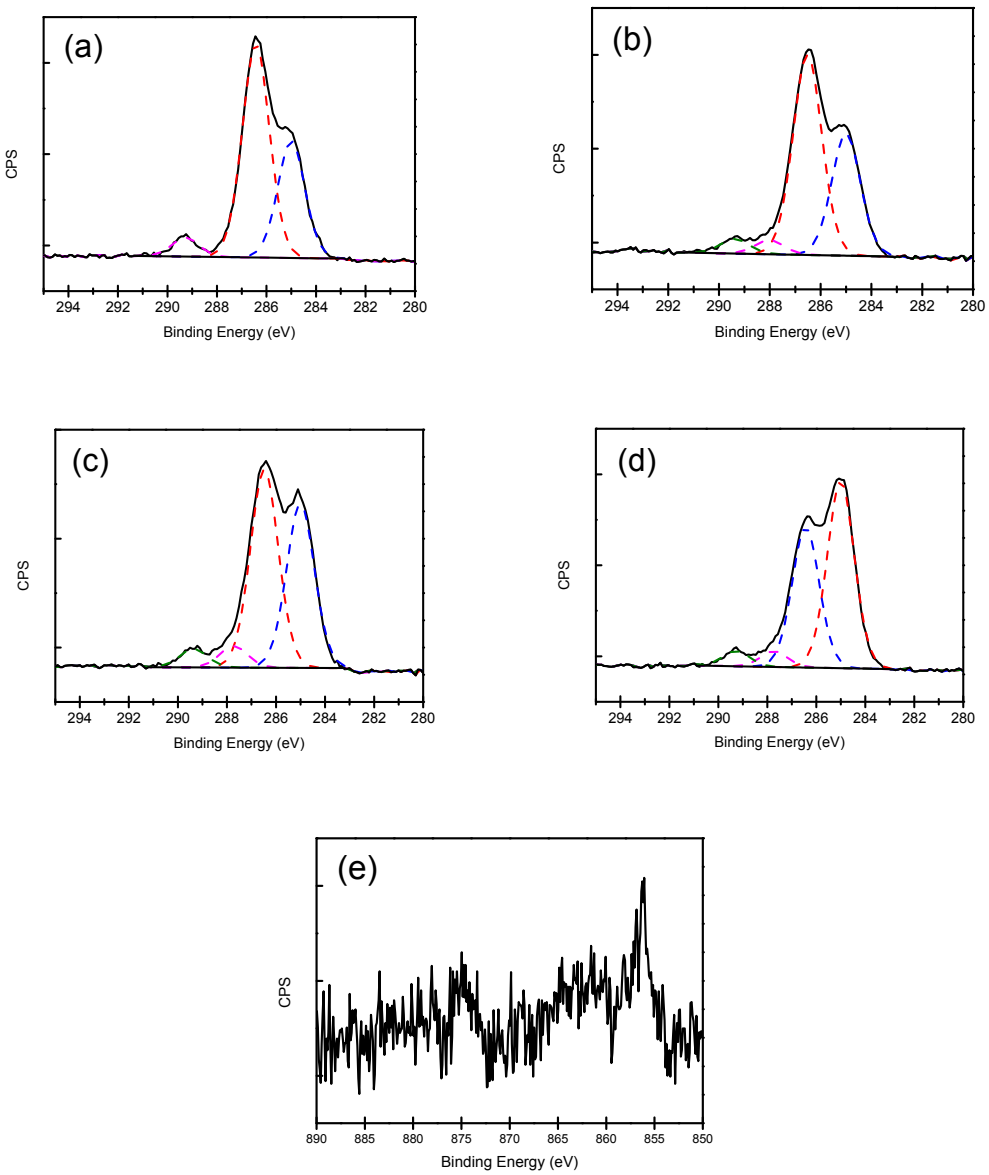

Figure 5.3 XPS C1s high resolution spectra of (a) OEG-NPEOC-APTES modified surface, (b) Surfaces (a) exposed by 325nm laser at the dose of 67 Jcm^{-2}, (c) Surface (b) reacting with GA, (d) Surfaces (c) reacting with ABNTA; XPS Ni2p high resolution spectrum of (e) NTA functional surfaces chelating with Ni^{2+}.

Table 5.3 Analysis of XPS C1s high resolution spectra above

	NPEOC		NPEOC exposed by 325nm laser		NPEOC exposure + GA		NPEOC exposure + GA + ABNTA	
	BE	EP	BE	EP	BE	EP	BE	EP
C-C	285.0eV	33.5%	285.0eV	34.7%	285.0eV	40.8%	285.0eV	52.2%
C-O; C-N; C=N	286.4eV	61.0%	286.5eV	57.1%	286.5eV	49.3%	286.5eV	39.1%
C=O			288.0eV	4.0%	287.7eV	5.4%	287.7eV	4.4%
O-C=O	289.3eV	5.5%	289.3eV	4.2%	289.3eV	4.5%	289.3eV	4.3%

*BE = Binding Energy, EP = Experimental Percentage.

5.3.2 Site-specific attachment of GFP and CPCA onto NTA functional OEG-NPEOC-APTES surfaces

Alang Ahmad et al. showed that OEG-NPEOC-APTES surfaces have good protein resistance.[68] After exposure, some of the OEG-NPEOC groups were removed and the exposed amine groups could be derivatised by protein while the remaining OEG-NPEOC groups still resisted non-specific protein attachment. It might be expected that the ratio of specifically adsorbed proteins to non-specifically adsorbed proteins would vary with the extent of deprotection, with attachment being purely via His-NTA interactions in the limit of infinite dilution. In order to explore the relationship between the amount of deprotection and the amount of non-specific adsorption, ellipsometry was used to characterize the protein attachment onto the exposed OEG-NPEOC-APTES surfaces. Figure 5.4 (a) shows the variation in thickness with exposure for two his-tagged proteins GFP and CPCA on NTA-functionalised OEG-NPEOC-APTES surfaces. The ellipsometric thickness is related to the adsorption amount and structure of protein. In Figure 5.4 (a), the thickness of the adsorbed protein layer increases with exposure for both GFP and CPCA up to a dose of ca. 5 Jcm^{-2}. Further increase of the dose leads to little subsequent change in the thickness of the protein layers. The final thickness of the GFP layer was ca. 35 Å and that of CPCA was ca. 40 Å. If we supposed

that most proteins were site specifically attached onto NTA-Ni^{2+} functional surfaces through his-tag, the thickness values are reasonable considering their orientation on the surfaces. Moreover, the thickness related to exposure dose can be fitted in the Langmuir adsorption model, which explains adsorption by assuming an adsorbate behaves as an ideal gas at isothermal conditions. In this case, surface coverage θ is plotted in Figure 5.4 (b) and 5.4 (c) by equation below.

$$\theta = \frac{kP}{1 + kP}$$

Exposure dose can be used to represent pressure (p) here. The parameter k is calculated from the linear fitting by equation $kt = \frac{T_t}{T_\infty - T_t}$ regardless of several bad points, in which T_t is the thickness of proteins corresponding to different doses. T_∞ were regarded as 41.94 Å for CPCA and 35.5 Å for GFP obtained from Figure 5.4 (a). The time t can be represented by exposure dose as well.

Figure 5.4 (b) and 5.4 (c) show that the adsorption behaves of GFP and CPCA onto NTA functional surfaces can be well explained by Langmuir model. From the graphs, it's observed that more than ninety percentage of surface has been covered by proteins of either GFP or CPCA after exposure dose of ca. 5 Jcm^{-2}. The results suggest that an exposure dose of ca. 5 Jcm^{-2} is sufficient to ensure the formation of a monolayer of site-specifically oriented proteins.

In a control experiment, proteins were attached onto exposed OEG-NPEOC-APTES surfaces through physical adsorption (Figure 5.4d). The thickness of proteins increased more slowly with the exposure and finally reached a stable value after an exposure of 10 Jcm^{-2}. The final thickness of GFP was ca. 40 Å and that of CPCA was ca. 65 Å. Comparison of Figure 5.4 (a) and (d) leads to the conclusion that more protein is attached to the NTA-Ni^{2+} functionalised surfaces than is adsorbed to the unmodified amine-containing surfaces. This means that when the surface is functionalised with NTA, protein is site-specifically bound at exposure too low to yield complete removal of the protein-resistant OEG-NPEOC groups.

(a)

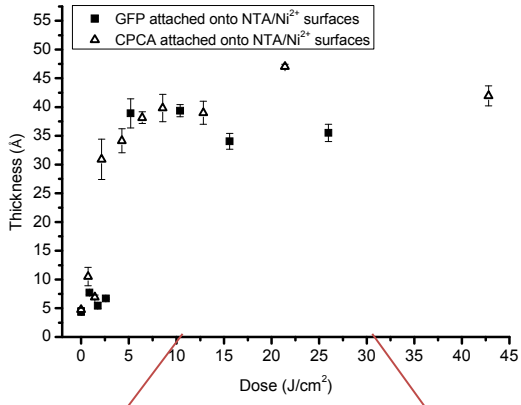

(b)

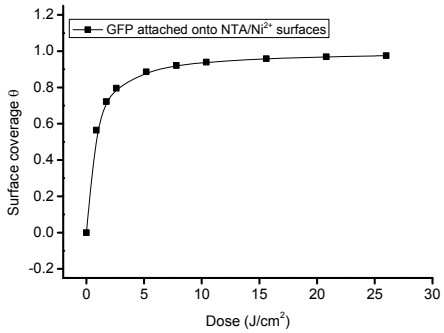

(c)

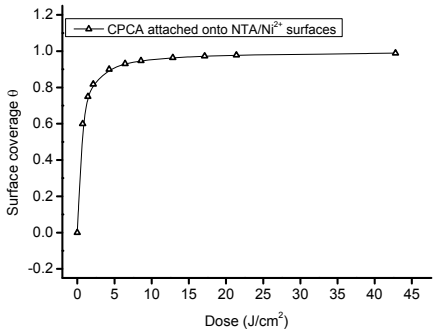

(d)

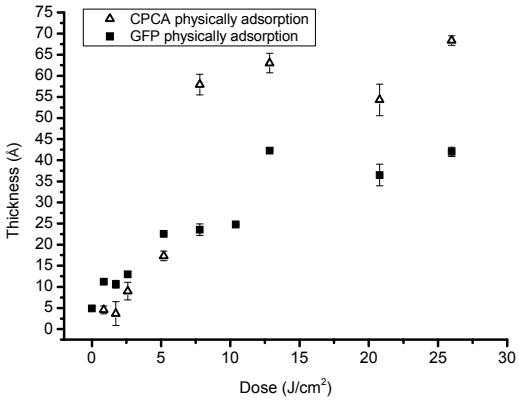

Figure 5.4 (a) Irradiation dose-dependent thickness of GFP and CPCA specifically attached on NTA/Ni^{2+} functional surfaces. Plots of surface coverage of (b) GFP and (c) CPCA on NTA/Ni^{2+} functional surfaces with respect to irradiation dose. (d) Irradiation dose-dependent thickness of GFP and CPCA physically adsorbing on surfaces.

5.3.3 Site-specific protein patterning

Microscale patterns were formed by UV lithography. After derivatisation with NTA and Ni^{2+}, His-tagged GFP and CPCA were attached onto the surfaces. Figure 5.5(a) and (b) show the confocal fluorescence images of GFP and CPCA microscale patterns. Bright fluorescence was observed for the exposed regions (squares) indicating high levels of attachment, and dark contrast regions in the masked areas (bars) indicated low levels of nonspecific protein adsorption on the unexposed regions where the OEG-NPEOC protecting groups were intact. Nanofabrication was carried out by SNP. A SNOM probe was coupled to light from a HeCd laser and traced across the OEG-NPEOC-APTES modified surfaces to fabricate patterns of 6 lines. The exposed regions were functionalized with NTA and Ni^{2+} and the samples were immersed in GFP and CPCA solutions to form nanopatterns consisting of site-specifically bound protein. Figure 5.5(c) and (d) shows confocal fluorescence images of GFP and CPCA nanopatterns. Strong fluorescence contrast was observed between the lines and the unexposed regions. Line cross sections through the nanopatterns demonstrate that sharp and well-defined features have been formed (Figure 5e and 5f). The full width at half-maximum (FWHM) is ca. 600 nm for the GFP lines and ca. 400nm for the CPCA lines. In the region with protein attachment, the signal could go up to 250 a.u. for GFP (Figure 5.5e) and 200 a.u. for CPCA (Figure 5.5f) and signal in the unmodified regions is nearly zero, which suggests very little nonspecific attachment. The small number of isolated spots apart from the six lines features may result from adventitious deposition.

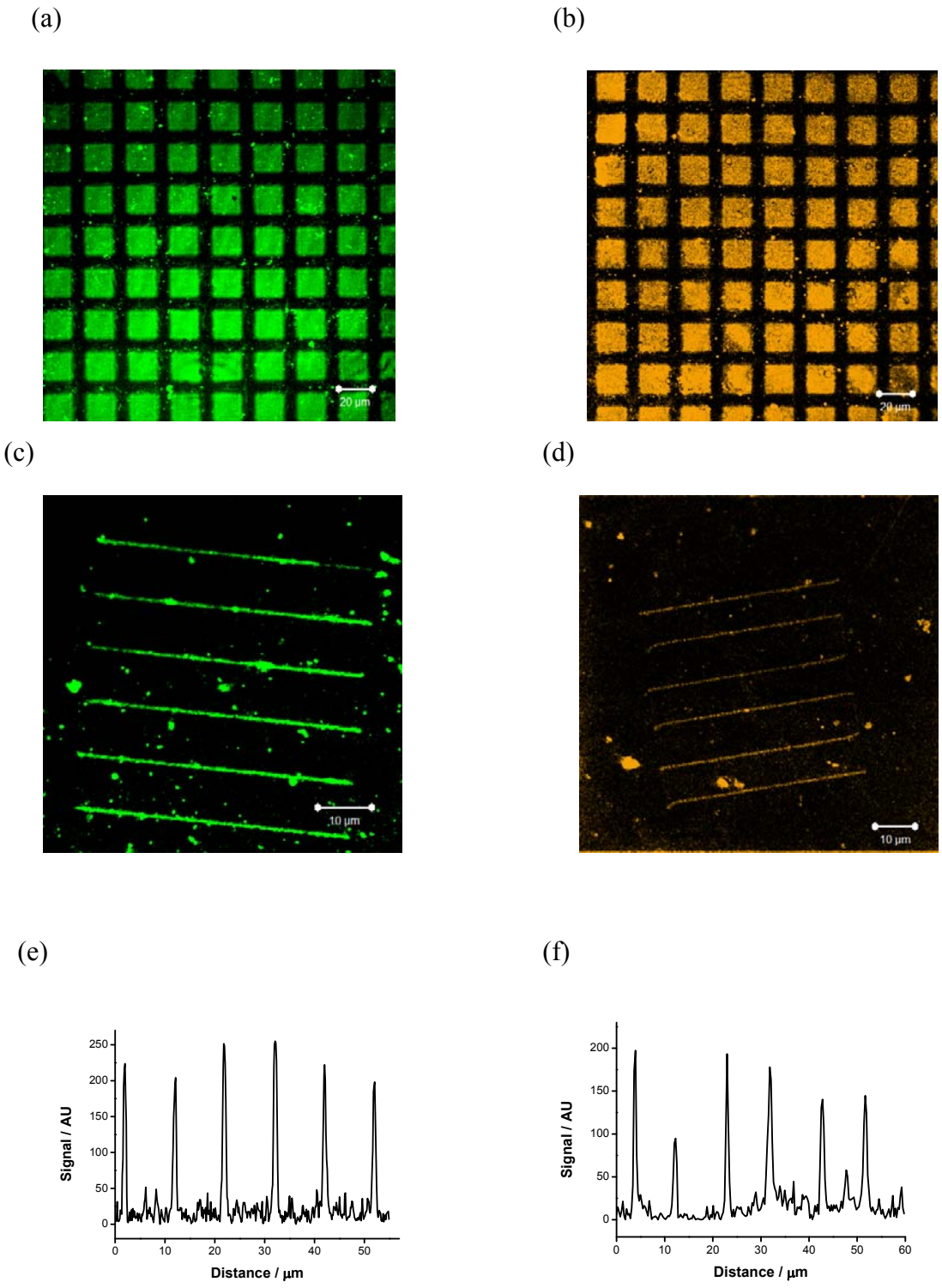

Figure 5.5 Confocal fluorescence images of (a) GFP and (b) CPCA micropatterns formed by UV lithography; (c) GFP and (d) CPCA nanopatterns formed by SNP. Cross sections through the nanopatterns (c) and (d) are shown in (e) and (d) respectively.

To determine whether site-specific binding of the His-tagged protein was occurring on NTA/Ni^{2+} surfaces, the reversibility of GFP micropattern formation was checked by the addition of a large excess of imidazole, which removes Ni^{2+} from the His-tagged protein/Ni^{2+}/NTA complex via ligand competition. Figure 5.6(a) and (b) shows that majority of the fluorescence of the His-tagged GFP immobilized on the NTA functional regions (square) was removed by the addition of 1M imidazole. Some residual spots are attributed to nonspecific binding. In the control experiment, GFP was physically attached onto OEG-NPEOC-APTES micropatterns and the fluorescence intensity didn't change before and after the treatment of imidazole (Figure 5.6c and d).

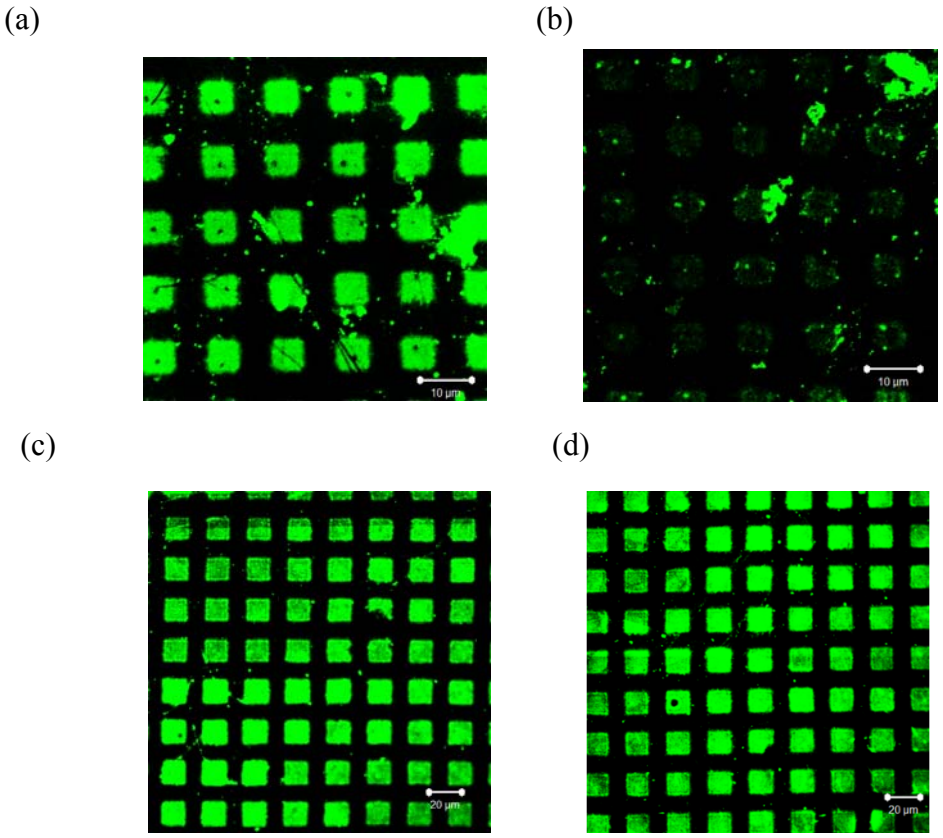

Figure 5.6 Confocal fluorescence images of (a) site-specific attachment of GFP onto microscale structures functionalised by NTA/Ni^{2+} and (b) the same micropatterns of GFP after treatment of 1M imidazole; (c) physical attachment of GFP onto microscale structures of OEG-NPEOC-APTES and (d) the same micropatterns of GFP after treatment of 1M imidazole.

In order to quantify these interactions, the immobilization of His-tagged GFP on NTA functionalised region was estimated from the normalized fluorescence intensity, which was the difference in the value of GFP fluorescence intensity on the NTA functional regions (squares) and the unexposed regions (bars). The normalized fluorescence intensity of GFP before the treatment with imidazole represents the total binding of protein while that after treatment of imidazole represents the nonspecific binding of protein. The difference between those two fluorescence intensity measurements is proportional to the fraction of specifically bound protein. From the graphic in Figure 5.7(a), it can be seen that when the number of binding sites increased, as the exposure was increased, the fraction of nonspecific binding was remained small (but non-zero) so that the specific binding was growing up with the increase of total binding and occupying around eighty percentage of it. The images related to the graphic could be found in Figure 5.7(b) and (c).

(a)

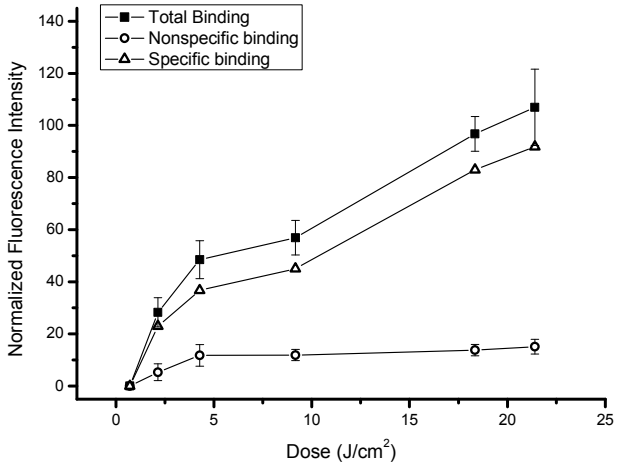

(b)

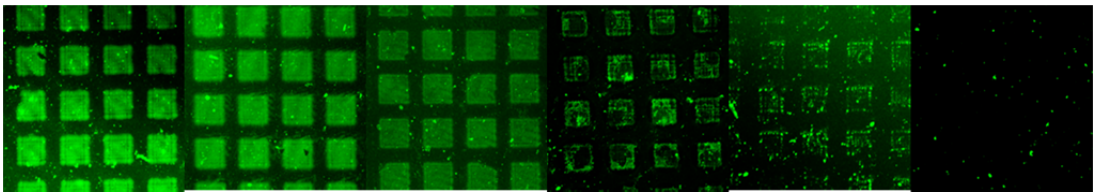

(c)

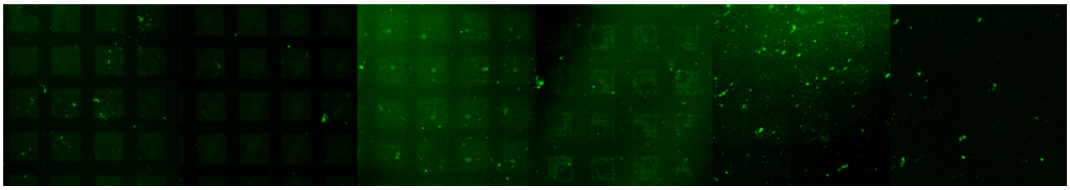

Figure 5.7 (a) Immobilization of his-tagged GFP on NTA/Ni^{2+} functional microscale structures, represented as normalized fluorescence intensity as a function of exposure dose. Specific binding was calculated as the difference between total binding and nonspecific binding; (b) GFP site-specifically attached onto microscale structures of OEG-NPEOC-APTES prepared by UV lithography at different dose, and (c) the same patterns of GFP after treatment of 1M imidazole, exposure dose for the patterns in (b) and (c) from left to right: 21.4 J/cm^2, 17.1 Jcm^{-2}, 8.6 Jcm^{-2}, 4.3 Jcm^{-2}, 2.1 Jcm^{-2}, 0.7 Jcm^{-2}.

5.4 Conclusions

A method was successfully developed to functionalize amine-terminated surfaces with ABNTA through the cross linker GA. XPS spectra established that NTA species had been bound onto surfaces and chelated with Ni^{2+}. From ellipsometric results and fluorescence images, it was found that the NTA functional OEG-NPEOC-APTES surfaces showed high affinity for the His-tagged proteins like GFP and CPCA. An exposure dose of 5 Jcm^{-2} is sufficient to ensure the formation of a monolayer of site-specifically oriented protein. Furthermore, site-specific protein patterns of GFP and CPCA were successfully prepared on NTA functional OEG-NPEOC-APTES surfaces via mask-based UV lithography and SNP. Compared with the protein patterns in last chapter, the attachment of GFP and CPCA in this chapter is reversible, which had been identified using competitive ligands like imidazole. Well-defined protein patterns with micrometer and nanometer sizes were obtained. It's thought that these simple strategies combining NTA/Ni^{2+}/His-tag system with photochemistry could offer great potential for the site-specific immobilization of biomacromolecules at microscale and nanoscale structrures.

Chapter 6 Nanofabrication of LH2 crystals on Aryl Azide-terminated SAMs

6.1 Introduction

Azide-terminated surfaces have attracted a great deal of interest recently for the applications in surface-click reactions[203]. Rolf Huisgen first established the synthesis and mechanism of the 1, 3-dipolar cycloaddition in 1961, which is a reaction between a 1, 3-dipole and a dipolarophile to form a five-membered ring.[204] In organic synthesis, 1, 3-dipolar cycloaddition is important for the synthesis of five- and six-membered heterocycles by uniting two unsaturated reactants. The azide cycloaddition reactions are widely valued for their ease of introduction and reduction of amino groups.[203] Recently there has been a great deal of interest in the use of click reactions to functionalise solid surfaces or biomaterials.[205-209] Devadoss et al. successfully functionalised graphitic carbon surfaces with aryl molecules through copper(I)-catalyzed 1, 3-dipolar cycloaddition.[206] Lummerstorfer et al. prepared monolayers of 11-azido-undecylsiloxane on silica surfaces by the substitution of 11-bromo-undecylsiloxane and then coupling with substituted acetylenes via Huisgen 1, 3-dipolar cycloaddition.[210] Wang et al. synthesized some cationic polymers as the gene carriers by copper (I)-catalyzed azide-alkyne cycloaddtion (CuAAC) step-growth polymerization of the dialkyne-oligoamine monomers and the diazide monomers.[209] However, azides are also useful photoactive functional groups that can be converted to nitrenes by exposure to UV light.[211,212] Azide-terminated SAMs can be modified by photolithography and also by photochemical reaction with primary and secondary amines. EI. Zubir et al. prepared some micro and nanoscale patterns on gold and aluminium oxide surfaces functionalised by azide-terminated thiols and phosphonic acids respectively via UV lithography and scanning near field photolithography.[213] Their results indicated that azide-terminated SAMs were good platforms for the immobilization of proteins through photoreactions.

In this Chapter, a new azide, 4-azido-3-(triethoxypropylsilane) benzamide (aryl azide) (Scheme 6.1a) is introduced. From former literature, possible photoreactions of this molecule can be deduced in Scheme 6.1. Phenyl azide (a) eliminates molecular nitrogen to yield a singlet nitrene (b) first, which could undergo intersystem crossing (ISC) to form a triplet phenyl nitrene (c) or rearrange to benzazirine (d). Benzazirine rearranges again to form ketenimine (e), which could react with amines to form 2-amino-3H-azepines (f)[214] or form polymers with itself. Ketenimine could also revert back into triplet phenyl nitrene irreversibly. Alternatively, single phenyl nitrene may form phenyl hydrazine (g) in the presence of amines[215,216] while triple phenyl nitrene may produce anilines (h) and diaryl diazo compounds (i)[215-219]. It was reported that singlet phenyl nitrene was converted to triple phenyl nitrene through ISC at 77 K but this would favour ring expansion at room temperature.[218,220,221] Hence in our experiment, phenyl azide (a) was supposed to form 2-amino-3H-azepines (f) in the presence of amines.

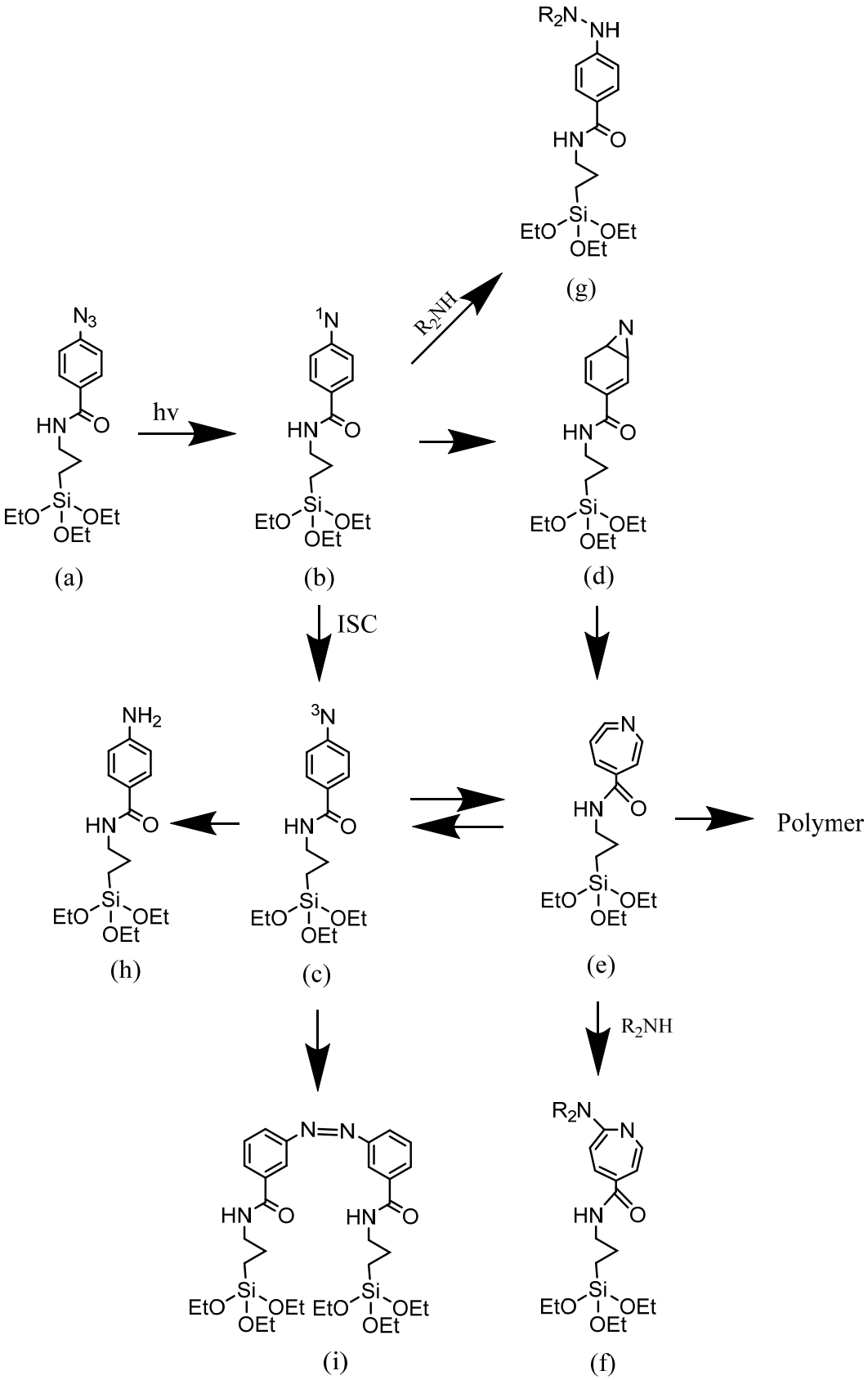

Scheme 6.1 Proposed process of photochemistry of aryl azides in the present of amines.

Interference lithography (IL), using a Lloyd's mirror interferometer coupled to 244 nm laser, was utilized to fabricate nanoscale structures on the aryl azide SAMs. As shown in Scheme 6.2, the azide-terminated surface was patterned to deactivate azides in the exposed areas. In the exposed areas, any intact azides or reactive products were blocked by reaction with octadecylamine. Then the sample was coated with a layer of adsorbed protein crystals and exposed a second time to process the photoreaction between the azide-terminated regions and amine groups in protein crystals. After removal of non-specifically attached parts, nanoscale patterns of protein had been produced on the surface.

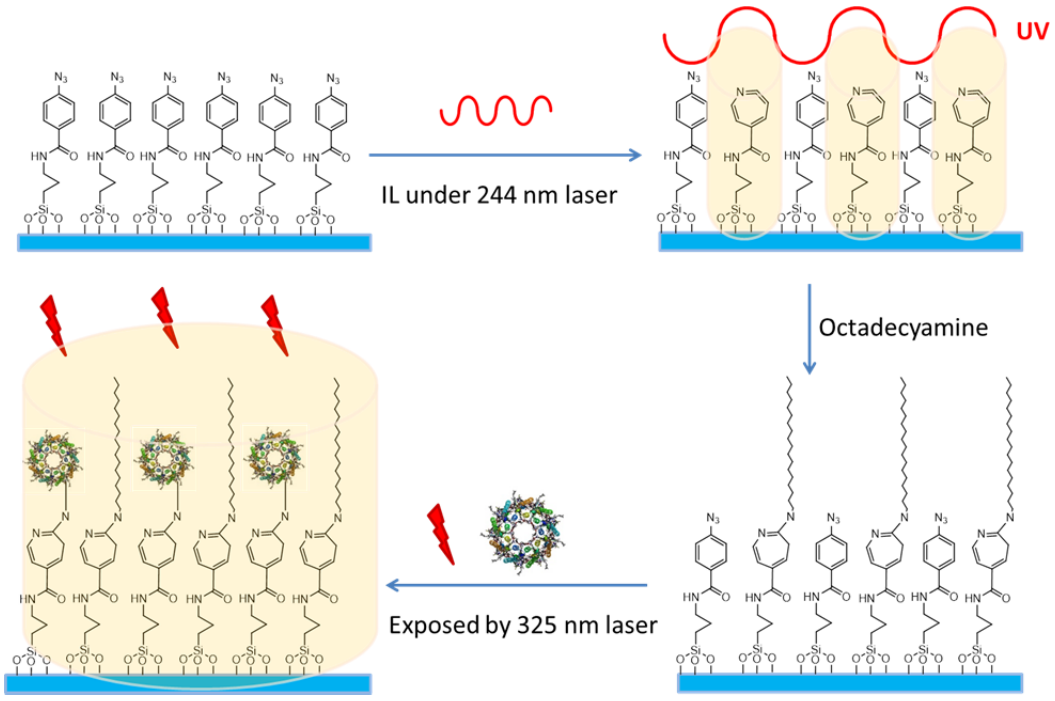

Scheme 6.2 Schematic illustration of the process to prepare nanoscale patterns of protein on aryl azide SAMs.

6.2 Experiment

6.2.1 Materials

Sulfuric acid ((1.83 S.G. 95+ %), hydrogen peroxide solution (100 volumes 30+ %), ammonia solution (S. G. 0.88, 35%) and toluene (HPLC grade) were supplied by Fisher Scientific (Loughborough, UK) and used as received. 4-azido-3-(triethoxypropylsilane) benzamide (Aryl azide) was synthesized by Paul J. Taylor from Prof. Nicholas H. Williams' group. Octadecylamine (97%), HEPES (≥99.5%, titration) and n-Dodecyl β-D-maltoside (β-DDM, ≥98% GC) were supplied by Sigma-Aldrich (Poole, UK). LH2 Crystals were provided by Dr Cvetelin. Vasilev (Department of molecular biology and biotechnology).

6.2.2 Preparation of Aryl azide SAMs on surfaces

Silicon wafers were first cleaned by piranha solution and RCA solution as discussed. They were immersed in 1 mM solution of aryl azide in toluene for 48 h to form SAMs. Then the samples were removed from solution, rinsed by toluene and ethanol for several times and dried by nitrogen gas. They were annealed in a vacuum oven for 1 h at 120 ℃.

6.2.3 Kinetic study of photoreaction of Aryl azide SAMs

SAMs of aryl azide were irradiated by either 325 nm or 244 nm laser at different dose and the water contact angles were analysed by Rame-Hart model 100-00-230 contact angle goniometer. Kratos Axis Ultra spectrometer (Kratos Analytical, Manchester, UK) were used to acquire the XPS spectra of the exposed surface and software CasaXPS was used to analyse the spectra.

6.2.4 Photoreaction of Aryl azide SAMs with Amines

Surfaces functionalised with aryl azide were immersed into 10 mM solutions of different amines like aminoethanol, octadecylamine and 2, 2, 2-trifluoroethylamine in ethanol. 325 nm laser with the power of 10mW was used to irradiate the whole samples for 15 min. The samples was then rinsed by ethanol and dried by nitrogen gas. Contact

angle measurements and XPS analysis were carried out on the surfaces.

6.2.5 Preparation of LH2 protein patterns on azide-terminated surfaces

Azide-terminated surfaces were patterned by interference lithography (IL) described in Chapter 2 under 244 nm laser and immersed into a 10 mM solution of octadecylamine in ethanol immediately for 0.5 h to passivate the exposed regions. Patterned samples were exposed by 325 nm laser again in the presence of a solution of LH2 crystals in 20 mM HEPES buffer solution (PH = 7.4). Then the samples were immersed into 20 mM HEPES buffer solution with 2% β-DDM for 0.5 h and sonicated to remove the non-specific attachment of proteins. AFM were used to analyse the LH2 patterns on the surfaces.

6.3 Results and Discussion

6.3.1 Study on the photoreaction of Aryl azide SAMs

6.3.1.1 Contact angle

Figure 6.1 shows the variation in the contact angle of aryl azide functionalised surfaces following exposure to light at 325 nm and 244 nm. Before irradiation, the contact angle was ca. 74^{o}. When irradiated by 325 nm laser (Figure 6.1a), this value was reduced to approximately 65^{o} by exposure to a dose of 0.56 Jcm^{-2}. The contact angle continued to decrease with the increasing exposure until it reached a limiting value of ca. 45^{o}. Further exposure did not affect the value of the contact angle, suggesting that the reaction was close to completion at a dose of ca. 33 Jcm^{-2}. When irradiated by the 244 nm laser (Figure 6.1b), the contact angle dropped to ca. 50^{o} rapidly by an exposure to dose of 0.81 Jcm^{-2}. It continued to decrease with the increasing exposure dose until it reached a limited value of 30^{o}. In comparison of those two graphics, contact angle of the surfaces irradiated by 244 nm laser decreased much more quickly than the one irradiated by 325 nm laser, probably due to the stronger power of the 244 nm laser. The deprotection processes for aryl azide SAMs at 325 nm and at 244 nm are possibly different. Only azide modification occurs when exposure is at 325 nm but at 244 nm, the possibility exists that ablation of adsorbate molecules may occur. Clear evidence for this hypothesis has not been acquired at present.

(a)

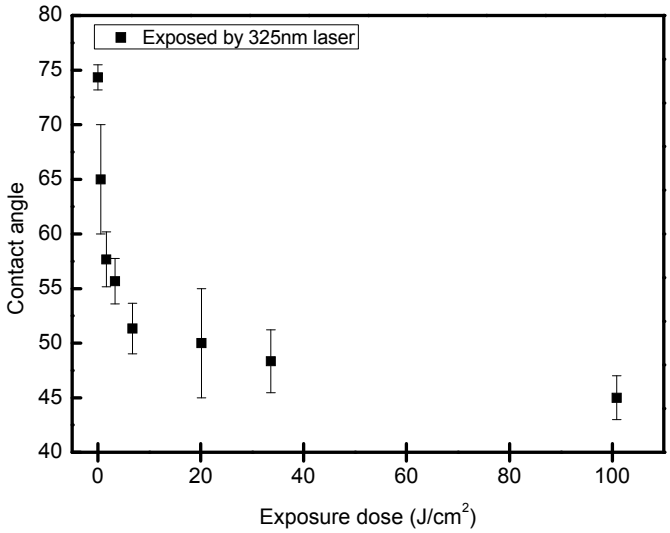

(b)

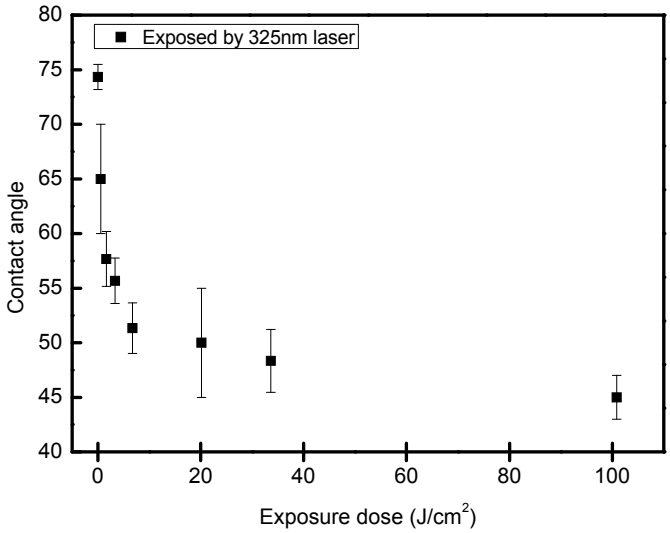

Figure 6.1 Graphs show the relationship between water contact angle of aryl azide functionalized surfaces and exposure dose under (a) 325 nm laser and (b) 244 nm laser.

6.3.1.2 XPS N1s spectra

Films of aryl azide terminated silanes were exposed to either a 325 nm or a 244 nm laser. Figure 6.2 shows the variation in the N1s spectra as a function of exposure for these SAMs.

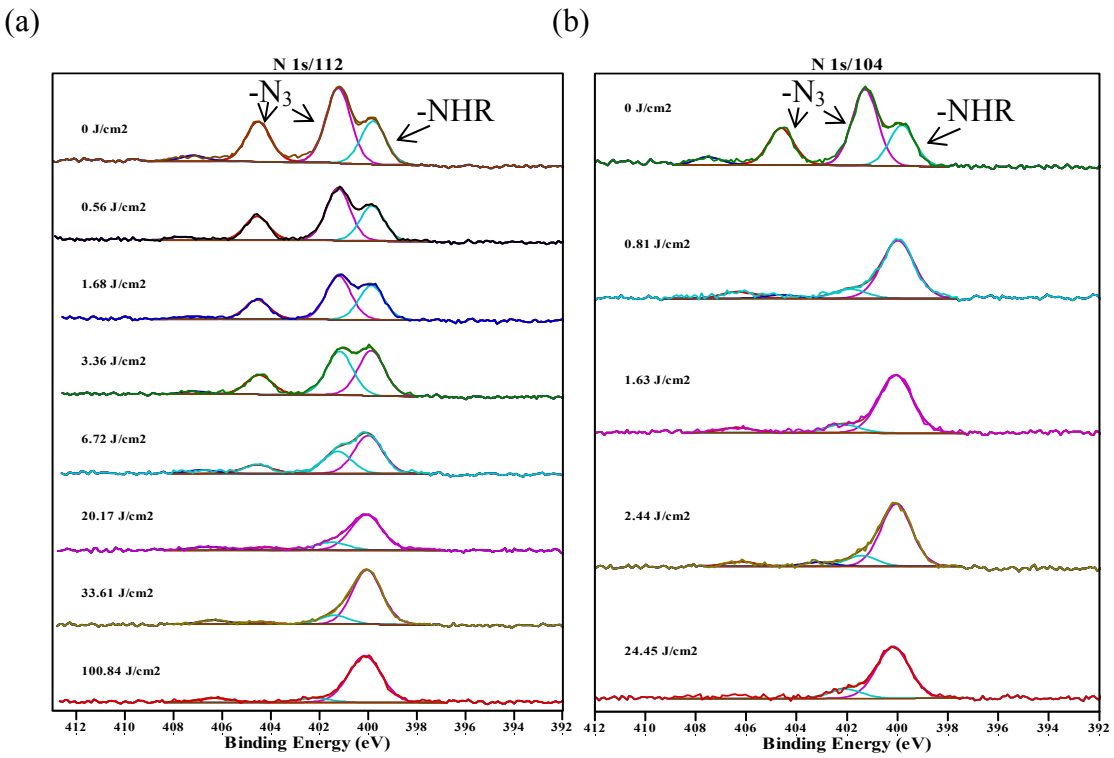

Figure 6.2 The variation of XPS N1s spectra for azide-terminated surfaces as a function of exposure dose under (a) 325 nm laser and (b) 244 nm laser.

Figure 6.3 shows the fractions of the N1s peaks attributable to the azide component as a function of exposure. Before irradiation by any laser, the spectrum for the virgin SAMs is fitted with three peaks. The peak at 399.7 eV is attributed to nitrogen in amide and aniline groups. Amide is characteristic of the virgin film while aniline comes from the products of photoreaction. The peaks at 401.2 eV and 404.5 eV were attributed to nitrogen in the azide group. As shown in Figure 6.2 (a) and 6.3 (a), under irradiation by the 325 nm laser, the area of the azide peak decreases gradually with increasing exposure while the areas of amide and aniline peaks increase at the same time. For the virgin SAMs, the area of the azide peak is 70.1% of the total area of the N1s peak and the sum of the amide and aniline peaks is 26.4%. After exposure to a dose of 33.6 Jcm^{-2}, the area of the azide peak declines to 16.2% and the area of the amide and aniline peaks grows to 77.9%. Those results are consistent with the contact angle results. As shown in Figure 6.2 (b) and 6.3 (b), under irradiation at 244 nm, the area of azide peaks decreases to 16.4% very quickly and and the area of the amide and aniline peaks grows to 75.1%

at an exposure of 0.81 Jcm^{-2}. Although the corresponding contact angles decrease a little further after more exposure, the area of the amide and aniline peaks in N1s spectra remains approximately unchanged. It is thought that other reactions occur during the process but the exposure doses of ca. 0.8 Jcm^{-2} under 244 nm laser and ca. 33 Jcm^{-2} under 325 nm laser were used to prepare patterns on azide-terminated surfaces in this experiment when irradiation was carried out.

(a)

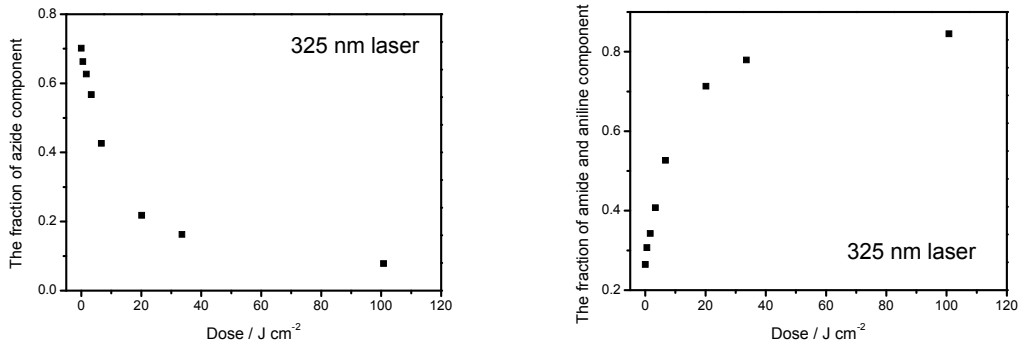

(b)

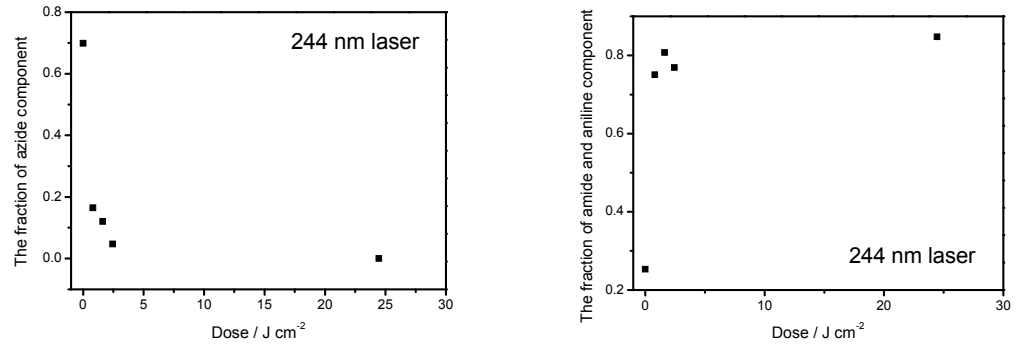

Figure 6.3 Variation in the fraction of azide component (left) and amide and aniline component (right) in XPS N1s spectra of aryl azide SAMs as a function of the exposure to UV laser at (a) 325 nm and (b) 244 nm.

6.3.2 Photoreaction of Aryl azide SAMs with Amines

6.3.2.1 Contact angle data

Aryl azides can react with amines, especially secondary amines, under irradiation by

UV light. In order to optimise the photo attachment chemistry, a series of reactions was performed involving the coupling of model amine to the surface. Contact angles were measured before and after the reaction. Figure 6.4 shows the water contact angle of the azide-terminated surfaces, which is ca. 74^{o} before exposure to UV light. When exposed to UV light, it is reduced to ca. 45^{o}. The sample was exposed while immersed under a layer of liquid ethanolamine, the contact angle decreases to ca. 39^{o}. This increase in the surface free energy is commensurate with the attachment of ethanolamine to the surface. After photoreaction with octadecylamine and 2, 2, 2-trifluoroethylamine, the contact angles increased to ca. 96^{o} and ca. 65^{o} respectively because in these cases the coupling of the amine to the surface yields a reduction in the surface free energy. Comparing with the contact angle results obtained by EI Zubir et al[213], the contact angle of azide terminated silanes on silica is slightly smaller than that of azide terminated phosphates on aluminium oxide and azide terminated thiols on gold, possibly indicating that they were more closely packed. The change of the contact angles after photoreactions with different amines is quite similar with the ones obtained by EI Zubir et al, which indicates that the reactions proceeded as expected.

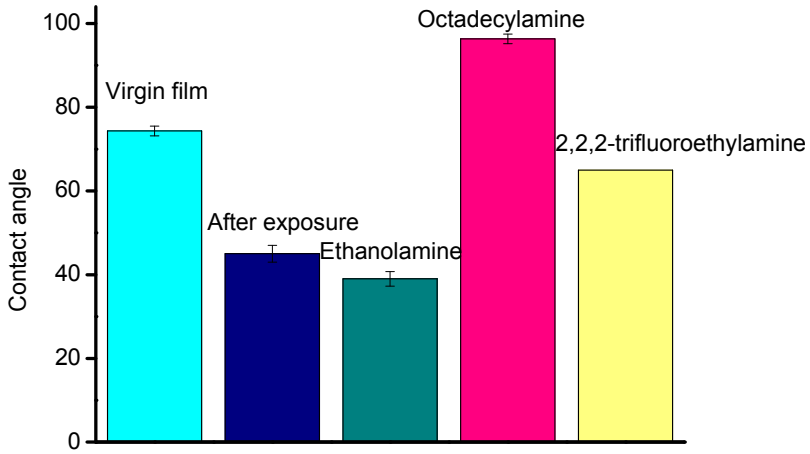

Figure 6.4 The contact angles of aryl azide SAMs before and after reaction with different amines by exposure of the surface while submerged between a film of the appropriate amine.

6.3.2.2 XPS C1s spectra

The photoreactions of aryl azide SAMs with amines were also investigated by XPS. Figure 6.5 (a) shows the C1s spectrum of the virgin SAMs. It is fitted with three components, which are attributed to –C-C-C- (BE = 285.0 eV), -C-C-N- (BE = 286.3 eV) and –C-C=O (BE = 288.1 eV) respectively. After the reaction with octadecylamine (Figure 6.5b), the percentage of the component at 285.0 eV increases from 65.7% of the total to 74.6% due to the coupling of the long carbon chain to the surface. If a full monolayer is formed after the reaction, the percentage of the component at 285.0 eV should increase to 88.9%. However, the actual result suggests that one fifth of the azide groups react with the amine. After the reaction with ethanolamine, the size of the components at 286.3 eV and 288.1 eV increases in the C1s spectrum (Figure 6.5c) because of the increasing amount of -C-C-N- and –C-C-O- at the surface. In Figure 6.5 (d), which shows the C1s after the reaction with 2, 2, 2-trifluoroethylamine, a new component may be seen at 292.9 eV, which is attributed to the $–CF_3$ group. The high resolution F1s spectrum shown in Figure 6.5 (e) provides good evidence for the photoreaction between aryl azide SAMs and 2, 2, 2-trifluoroethylamine, a strong peak is observed confirming the presence of a significant amount of fluorine. Those spectra are almost the same as the ones obtained by EI Zubir et al. using azide-terminated phosphonic acids to react with different amines[213]. All the results above confirm that the photoreactions of aryl azide SAMs with amines occur successfully.

(a) Virgin film

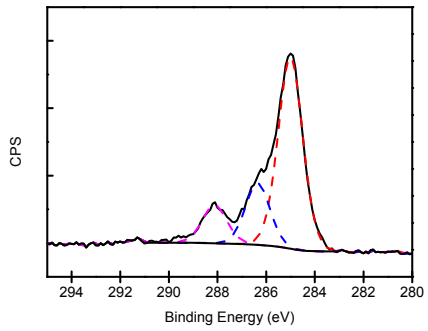

(b) UV + octadecylamine

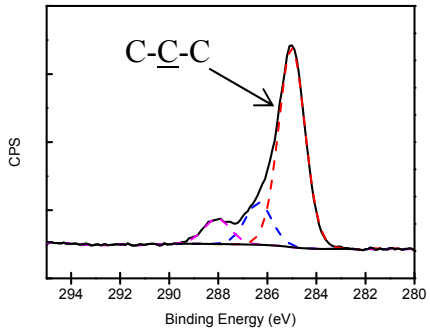

(c) UV + ethanolamine

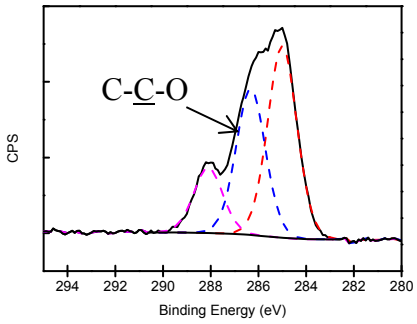

(d) UV + 2, 2, 2-trifluoroethylamine

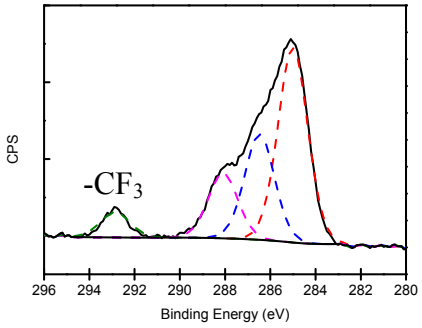

(e) F1s

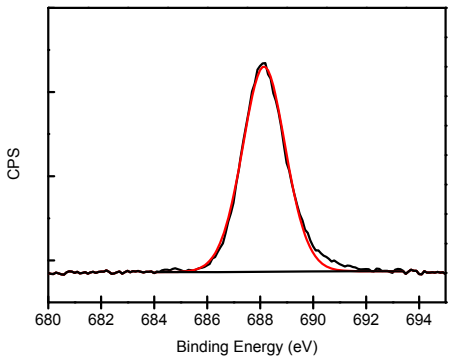

Figure 6.5 (a) to (d) XPS C1s spectra of aryl azide SAMs before and after reactions with different amines in the presence of UV light at 325 nm; (e) high resolution F1s spectrum of aryl azide SAMs after photoreaction with 2, 2, 2-trifluoroethylamine.

6.3.3 Nanofabrication by IL

Figure 6.6 shows friction images of microscale and nanoscale patterns formed on aryl azide terminated SAMs made by mask-based lithography and IL respectively. In those

images, the dark areas were exposed regions by UV light and passivated by octadecylamine. These regions are possibly terminated with long hydrocarbon chains from octadecylamine, which makes the surface more hydrophobic. When the hydrophilic AFM tip crosses the more hydrophobic surface, the rate of energy dissipation is lower so the coefficient of friction becomes smaller. The bright areas were unexposed and terminated with azide groups, giving rise to a higher rate of energy dissipation and hence a larger coefficient of friction. Success of patterning on azide-terminated surfaces provides good platform to prepare protein patterns.

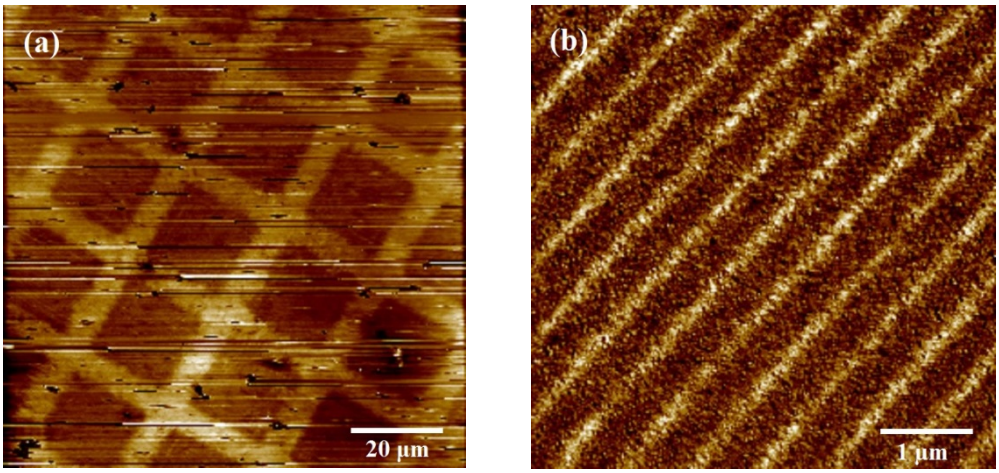

Figure 6.6 AFM friction images of (a) microscale patterns and (b) nanoscale IL patterns on aryl azide SAMs.

6.3.4 Immobilization of LH2 crystals

Protein immobilization is an important application of the modified SAMs. The azide-terminated surface was exposed to selectively passivate regions. Protein crystals were deposited onto the surface. It was hypothesized that amine groups on LH2 proteins in close proximity to unmodified azide groups on the surface would be photochemically coupled to them during flood exposure at 325 nm. The remaining non-covalently bound proteins were washed away by buffer solution. The covalently bound LH2 proteins form the nanometre scale patterns. Figure 6.7 shows the AFM height images of LH2 patterns. They exhibit well-defined regions of bright and dark contrast. The dark regions were

exposed to minima in the interferogram. In these regions any remaining azides were reacted with octadecylamine. There was very little non-specific adsorption in these regions. The bright areas show high density immobilization of LH2 onto the intact azide-terminated regions after photoreaction. As discussed before, when changing the rotation angle of the mirror in IL setting and exposure dose, the period and FWHM of exposed regions will be changed. In Figure 6.7, the period and the FWHM of the features are shown in corresponding cross sections. When the angle was set to be 10^{o} and the exposure was ca. 6 Jcm^{-2}, the FWHM of the features was ca. 150 nm and the period was ca. 550 nm (Figure 6.7a). When the angle was 15^{o} and exposure dose was 4 Jcm^{-2}, the FWHM of linear patterns was ca. 190nm and the period was ca. 590 nm (Figure 6.7b). When the angle was 20^{o} and exposure dose was 4 Jcm^{-2}, the FWHM of linear patterns was ca. 105 nm and the period was ca. 290 nm (Figure 6.7c). The height of LH2 protein measured in air is ca. 3nm in all images. LH2 is a cylindrical membrane protein complex with an external diameter of 7 nm and height of 7 nm.[99,187] Comparing with the known dimension of LH2, the measured height is reduced, probably because more material was added to the dark regions during the passivation, which leads to a decrease of the apparent height of the LH2 in AFM images. The images on the right show the magnified regions of the left images, from which the pattern produced at an angle of 20^{o} is less well-defined so that an angle 10^{o} and 15^{o} seem better in order to fabricate well-defined patterns of proteins through this methodology.

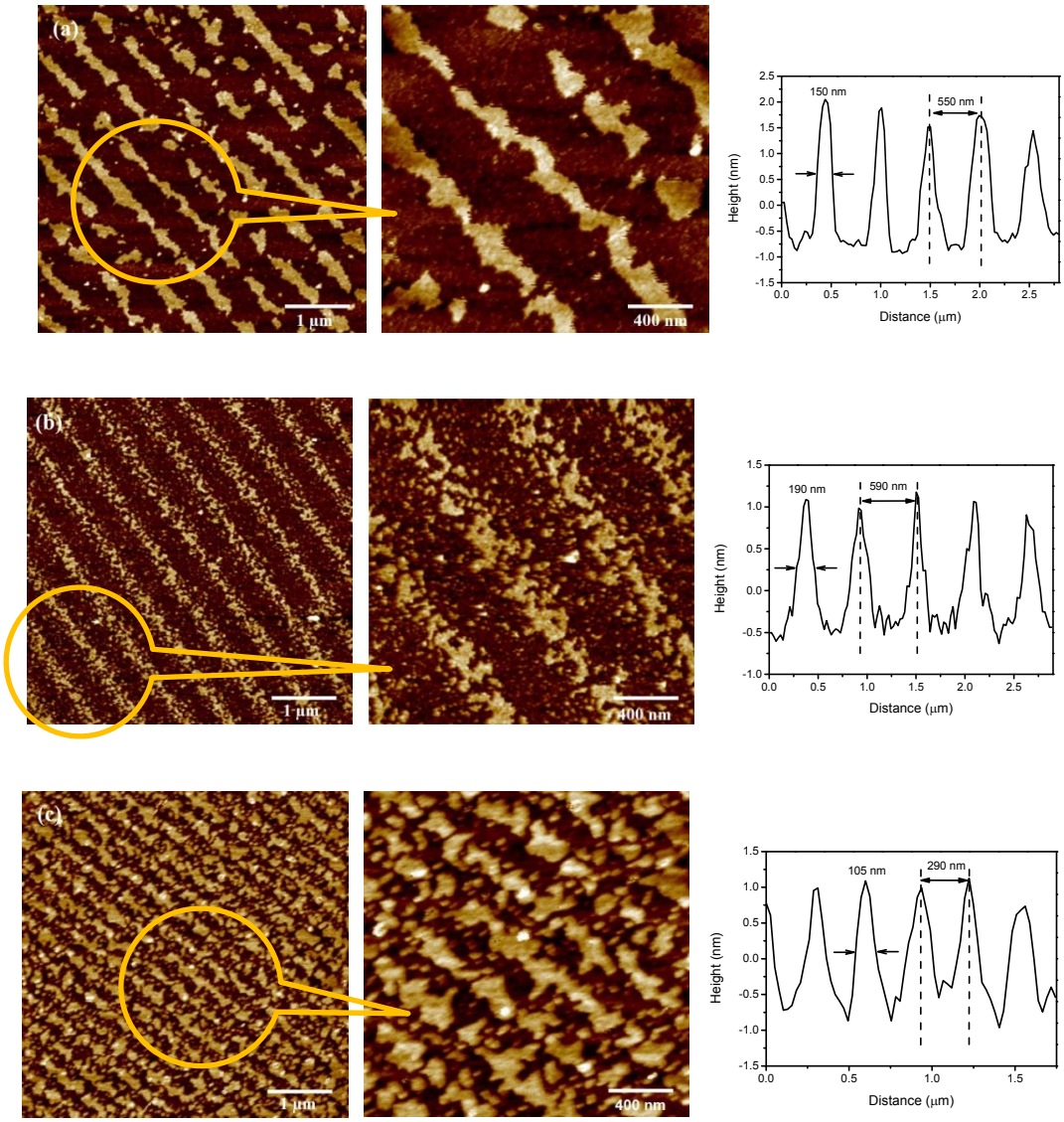

Figure 6.7 AFM height images of LH2 nanoscale patterns made via IL under different conditions: (a) angle = 10^{o}, dose = 6 Jcm^{-2}; (b) angle = 15^{o}, dose = 4 Jcm^{-2}; (c) angle = 20^{o}, dose = 4 Jcm^{-2}.

6.4 Conclusions

SAMs of a new aryl azide, 4-azido-3-(triethoxypropylsilane) benzamide (aryl azide), have been successfully prepared on silica surfaces. Compared with others' work, this molecule formed more closely packed monolayers. XPS data and contact angle results demonstrated the photodeprotection rate of aryl azide SAMs under laser exposure at 325 nm and 244 nm. Dose of ca. 33 Jcm^{-2} under 325 nm laser and that of ca. 0.8 Jcm^{-2} under 244 nm laser were used for the patterning. Those measurements also confirmed that the photoreactions between aryl azide and different amines were carried out successfully. Nanometer scale patterns fabricated on aryl azide surface by IL were obtained. The exposed regions were passivated by octadecylamine and the unexposed regions were coupled with LH2 crystals through photoreactions between azide and amine groups. AFM images showed that different sizes of parallel lines patterns of LH2 were fabricated with the FWHM of protein lines as small as 105 nm.

Chapter 7 Conclusion

The present study has demonstrated the successful fabrication of single and multiple protein patterns in siloxane monolayers on silica surfaces through photochemical methods. Different lithographic techniques like mask-based UV lithography, Interferometric lithography (IL) and scanning near-field photolithography (SNP) have shown the capability to generate micrometer and nanometer scale features on the self-assemble monolayers (SAMs) of silanes.

In Chapter 3, APTES SAMs have been successfully formed on hydrated substrates under ambient conditions. The water content in the solvent toluene was measured on different days using Karl Fisher Titration. The data suggested that a small amount of water ranged from 67.3 ppm to 93.3 ppm was present in solvent and its amount varied comparatively little over time, which affected film formation very little. The APTES surface had good surface coverage with a water contact angle up to 55°. AFM height images indicated that APTES surface was quite flat with a roughness less than 0.5 nm. The thickness of the APTES films increased with the immersion time and concentration, which suggested the eventual formation of multilayers. This hypothesis was supported by XPS results, in which the percentage of nitrogen increased with the immersion time and concentration. 10^{-2} (v/v) APTES solution in toluene and reaction time of 1 h were chosen as the optimum conditions for the preparation of APTES monolayers in the later chapters.

In Chapter 4, SAMs of aminopropyltriethoxysilane protected by oligo (ethylene glycol) modified 2-nitrophenylethoxycarbonyl (OEG-NPOEC-APTES) were prepared on silica surfaces. XPS results indicated the deprotection rate of OEG-NPEOC-APTES SAMs which was monitored using the ratio of NO_2 and NH_2 peaks in XPS N1s spectra. Micrometre and nanometre scale patterns were fabricated on OEG-NPEOC-APTES SAMs by mask-based UV lithography, IL and SNP respectively, and used as the

platforms for the attachment of different proteins through cross-linker glutaraldehyde. Unexposed OEG-NPEOC-APTES SAMs showed good protein resistance. Furthermore, confocal fluorescence images confirmed that nanometer scale patterns of up to four kinds of proteins were achieved successfully for the first time through over-writing exposure using SNP. Membrane proteins like LH1 and LH2 could also be well patterned through this method. However, those proteins are just adsorbed on the surfaces with random orientation. Site-specific protein patterning was studied further in the next chapter based on the OEG-NPEOC-APTES SAMs.

Chapter 5 demonstrated a method to functionalise the photodeprotected OEG-NPEOC-APTES surface with aminobutylnitrilotriacetic acid (ABNTA) through the bifunctional linker glutaraldehyde. Attachment of ABNTA to selectively photo-deprotected OEG-NPEOC-APTES regions was carried out to produce patterns for site-specific protein binding. Ellipsometric results and confocal fluorescence images confirmed the site-specific attachment of His-tagged GFP and CPCA onto NTA/Ni^{2+} functionalized OEG-NPEOC-APTES surface with high efficiency and affinity. An exposure dose of ca. 5 Jcm^{-2} is sufficient to ensure the formation of a monolayer of site-specifically oriented protein. The reversibility of site-specific attachment of His-tagged proteins was also identified using competition ligands like imidazole.

Chapter 6 introduced a new azide, 4-azido-3-(triethoxypropylsilane) benzamide (aryl azide). Closely packed monolayers of this aryl azide have been successfully prepared on silica surfaces. XPS data and contact angle results demonstrated the photodeprotection rate of aryl azide SAMs under 325 nm and 244 nm laser. An exposure dose of ca. 0.8 Jcm^{-2} under 244 nm laser and that of ca. 33 Jcm^{-2} under 325 nm laser were used to produce patterns. XPS data and contact angle results also confirmed that the photoreactions between aryl azide and different amines were carried out successfully. Nanometer scale patterns fabricated on aryl azide surface by IL were obtained, on which LH2 crystals were attached through photoreaction between azide and amine groups. AFM images confirmed that different sizes of parallel lines patterns of LH2 were

fabricated with the FWHM of protein lines as small as 105 nm.

In sum, study on the formation of APTES SAMs provides optimum conditions to prepare smooth and dense APTES SAMs. Fabrication of multiple protein patterns on OEG-NPEOC-APTES SAMs shows the good protein resistance and photo deprotection features of OEG-NPEOC-APTES as well as the capability of SNP to produce complicated nanostructures. Based on this work, site-specific protein patterning was carried out successfully. Study on the new aryl azide provides a different method to create protein patterns. All these achievements are novel and useful for the development of a low dimensional system that can replicate the photosynthesis.

Chapter 8 Future Work

Multiple-protein patterns of LH1 and LH2 at nanometer scale could be used as the platform to build up the low-dimensional system that replicates the bacterial photosynthetic apparatus on a chip. Energy transfer between the photosynthetic apparatus could be investigated further. The spectrum of each component in the nanoscale patterns of multiple proteins could also be studied. It is hypothesized that there will be an energy shift due to the protein-protein interactions at nanometer scale.

OEG-NPEOC-APTES surface functionalised with ABNTA could be utilized on other substrates like IL-fabricated gold nanostructures[80] to prepared oriented protein patterns. Other kinds of proteins especially the membrane proteins can be oriented patterned by this method. Further study on the energy transfer between membrane proteins can be carried out based on this work.

The new aryl azide SAMs could be refunctionalised by ABNTA to prepare site-specific protein patterns or multiple-protein patterns. The patterns of membrane proteins prepared by this method could provide another way to build up the low-dimensional system that replicates the photosynthesis. The image resolution of LH2 patterns on aryl azide SAMs could be increased by using high resolution AFM to study the detailed structure of patterned LH2.

Reference

1 MacAlear J, W. J. Microsubstrates and method for making micropattern devices. *US Patent* **4,103,073** (1978).

2 MacAlear J, W. J. Microdevice substrate and method for making micropattern devices. *US Patent* **4,103,064** (1978).

3 Langmuir, I. The constitution and fundamental properties of solids and liquids. II. Liquids. *J Am Chem Soc* **39**, 1848-1906 (1917).

4 Langmuir, I. The condensation and evaporation of gas molecule. *P Natl Acad Sci USA* **3**, 141-147 (1917).

5 Langmuir, I. The shapes of group molecules forming the surfaces of liquids. *P Natl Acad Sci USA* **3**, 251-257 (1917).

6 Blodgett, K. B. Monomolecular films of fatty acids on glass. *J Am Chem Soc* **56**, 495-495 (1934).

7 Netzer, L. & Sagiv, J. A New Approach to Construction of Artificial Monolayer Assemblies. *J Am Chem Soc* **105**, 674-676 (1983).

8 Ulman, A. Formation and structure of self-assembled monolayers. *Chem Rev* **96**, 1533-1554 (1996).

9 Sagiv, J. Organized Monolayers by Adsorption .1. Formation and Structure of Oleophobic Mixed Monolayers on Solid-Surfaces. *J Am Chem Soc* **102**, 92-98 (1980).

10 Sellers, H., Ulman, A., Shnidman, Y. & Eilers, J. E. Structure and Binding of Alkanethiolates on Gold and Silver Surfaces - Implications for Self-Assembled Monolayers. *J Am Chem Soc* **115**, 9389-9401 (1993).

11 Ogawa, H., Chihara, T. & Taya, K. Selective Monomethyl Esterification of Dicarboxylic-Acids by Use of Monocarboxylate Chemisorption on Alumina. *J Am Chem Soc* **107**, 1365-1369 (1985).

12 Linford, M. R. & Chidsey, C. E. D. Alkyl Monolayers Covalently Bonded to Silicon Surfaces. *J Am Chem Soc* **115**, 12631-12632 (1993).

13 Lee, H., Kepley, L. J., Hong, H. G. & Mallouk, T. E. Inorganic Analogs of Langmuir-Blodgett Films - Adsorption of Ordered Zirconium 1,10-Decanebisphosphonate Multilayers on Silicon Surfaces. *J Am Chem Soc* **110**, 618-620 (1988).

14 Kim, J. Y., Seidler, P., Wan, L. S. & Fill, C. Formation, structure, and reactivity of amino-terminated organic films on silicon substrates. *J Colloid Interf Sci* **329**, 114-119 (2009).

15 Tripp, C. P. & Hair, M. L. Reaction of Alkylchlorosilanes with Silica at the Solid Gas and Solid Liquid Interface. *Langmuir* **8**, 1961-1967 (1992).

16 Angst, D. L. & Simmons, G. W. Moisture Absorption Characteristics of Organosiloxane Self-Assembled Monolayers. *Langmuir* **7**, 2236-2242 (1991).

17 Wasserman, S. R., Tao, Y. T. & Whitesides, G. M. Structure and Reactivity of Alkylsiloxane Monolayers Formed by Reaction of Alkyltrichlorosilanes on Silicon Substrates. *Langmuir* **5**, 1074-1087 (1989).

18 Brandriss, S. & Margel, S. Synthesis and Characterization of Self-Assembled Hydrophobic Monolayer Coatings on Silica Colloids. *Langmuir* **9**, 1232-1240 (1993).

19 Silberzan, P., Leger, L., Ausserre, D. & Benattar, J. J. Silanation of Silica Surfaces - a New Method of Constructing Pure or Mixed Monolayers. *Langmuir* **7**, 1647-1651 (1991).

20 Banga, R., Yarwood, J., Morgan, A. M., Evans, B. & Kells, J. Ftir and Afm Studies of the Kinetics and Self-Assembly of Alkyltrichlorosilanes and (Perfluoroalkyl)Trichlorosilanes onto Glass and Silicon. *Langmuir* **11**, 4393-4399 (1995).

21 Rusmini, F., Zhong, Z. Y. & Feijen, J. Protein immobilization strategies for protein biochips. *Biomacromolecules* **8**, 1775-1789 (2007).

22 Patel, N. *et al.* Immobilization of protein molecules onto homogeneous and mixed carboxylate-terminated self-assembled monolayers. *Langmuir* **13**, 6485-6490 (1997).

23 Yang, H. C., Dermody, D. L., Xu, C. J., Ricco, A. J. & Crooks, R. M. Molecular interactions between organized, surface-confined monolayers and vapor-phase probe molecules .8. Reactions between acid-terminated self-assembled monolayers and vapor-phase bases. *Langmuir* **12**, 726-735 (1996).

24 Wang, H., Chen, S. F., Li, L. Y. & Jiang, S. Y. Improved method for the preparation of carboxylic acid and amine terminated self-assembled monolayers of alkanethiolates. *Langmuir* **21**, 2633-2636 (2005).

25 Ducker, R. E., Montague, M. T. & Leggett, G. J. A comparative investigation of methods for protein immobilization on self-assembled monolayers using glutaraldehyde, carbodiimide, and anhydride reagents. *Biointerphases* **3**, 59-65 (2008).

26 Viitala, T., Vikholm, I. & Peltonen, J. Protein immobilization to a partially cross-linked organic monolayer. *Langmuir* **16**, 4953-4961 (2000).

27 Gauvreau, V. *et al.* Engineering surfaces for bioconjugation: Developing strategies and quantifying the extent of the reactions. *Bioconjugate Chem* **15**, 1146-1156 (2004).

28 Wacker, R., Schroder, H. & Niemeyer, C. M. Performance of antibody microarrays fabricated by either DNA-directed immobilization, direct spotting, or streptavidin-biotin attachment: a comparative study. *Anal Biochem* **330**, 281-287 (2004).

29 Corey, D. R., Munozmedellin, D. & Huang, A. Strand Invasion by Oligonucleotide Nuclease Conjugates. *Bioconjugate Chem* **6**, 93-100 (1995).

30 Rizzi, S. C. & Hubbell, J. A. Recombinant protein-co-PEG networks as cell-adhesive and proteolytically degradable hydrogel matrixes. Part 1: Development and physicochernical characteristics. *Biomacromolecules* **6**, 1226-1238 (2005).

31 Morpurgo, M., Veronese, F. M., Kachensky, D. & Harris, J. M. Preparation and characterization of poly(ethylene glycol) vinyl sulfone. *Bioconjugate Chem* **7**, 363-368 (1996).

32 Fernandezlafuente, R. *et al.* Preparation of Activated Supports Containing Low Pk Amino-Groups - a New Tool for Protein Immobilization Via the Carboxyl Coupling Method. *Enzyme Microb Tech* **15**, 546-550 (1993).

33 Sigrist, H. *et al.* Surface Immobilization of Biomolecules by Light. *Opt Eng* **34**, 2339-2348 (1995).

34 Das, M. & Fox, C. F. Chemical Cross-Linking in Biology. *Annu Rev Biophys Bio* **8**, 165-193 (1979).

35 Pillai, V. N. R. Photo-Removable Protecting Groups in Organic-Synthesis. *Synthesis-Stuttgart*, 1-26 (1980).

36 Pease, A. C. *et al.* Light-Generated Oligonucleotide Arrays for Rapid DNA-Sequence Analysis. *P Natl Acad Sci USA* **91**, 5022-5026 (1994).

37 Pirrung, M. C. & Huang, C. Y. A general method for the spatially defined immobilization of biomolecules on glass surfaces using "caged" biotin. *Bioconjugate Chem* **7**, 317-321 (1996).

38 Wilchek, M. & Bayer, E. A. The Avidin Biotin Complex in Bioanalytical Applications. *Anal Biochem* **171**, 1-32 (1988).

39 Luo, S. F. & Walt, D. R. Avidin Biotin Coupling as a General-Method for Preparing Enzyme-Based Fiber-Optic Sensors. *Anal Chem* **61**, 1069-1072 (1989).

40 Bayer, E. A., Benhur, H. & Wilchek, M. Biocytin Hydrazide - a Selective Label for Sialic Acids, Galactose, and Other Sugars in Glycoconjugates Using Avidin Biotin Technology. *Anal Biochem* **170**, 271-281 (1988).

41 Orth, R. N., Clark, T. G. & Craighead, H. G. Avidin-biotin micropatterning methods for biosensor applications. *Biomed Microdevices* **5**, 29-34 (2003).

42 You, C., Bhagawati, M., Brecht, A. & Piehler, J. Affinity capturing for targeting proteins into micro and nanostructures. *Anal Bioanal Chem* **393**, 1563-1570 (2009).

43 Hengsakul, M. & Cass, A. E. G. Protein patterning with a photoactivatable derivative of biotin. *Bioconjugate Chem* **7**, 249-254 (1996).

44 Sandberg, S. A. *et al.* Spatially-Addressable Immobilization of Macromolecules on Solid Supports. *J Am Chem Soc* **117**, 12050-12057 (1995).

45 Kim, K., Yang, H., Jon, S., Kim, E. & Kwak, J. Protein patterning based on electrochemical activation of bioinactive surfaces with hydroquinone-caged biotin. *J Am Chem Soc* **126**, 15368-15369 (2004).

46 Ahmad, S. A. A. *et al.* Micrometer- and Nanometer-Scale Photopatterning Using 2-Nitrophenylpropyloxycarbonyl-Protected Aminosiloxane Monolayers. *J Am Chem Soc* **131**, 1513-1522 (2009).

47 de Groot, G. W., Demarche, S., Santonicola, M. G., Tiefenauer, L. & Vancso, G. J. Smart polymer brush nanostructures guide the self-assembly of pore-spanning lipid bilayers with integrated membrane proteins. *Nanoscale* **6**, 2228-2237 (2014).

48 Schmid, E. L., Keller, T. A., Dienes, Z. & Vogel, H. Reversible oriented surface immobilization of functional proteins on oxide surfaces. *Anal Chem* **69**, 1979-1985 (1997).

49 Hochuli, E., Dobeli, H. & Schacher, A. New Metal Chelate Adsorbent Selective for Proteins and Peptides Containing Neighboring Histidine-Residues. *J Chromatogr* **411**, 177-184 (1987).

50 Sigal, G. B., Bamdad, C., Barberis, A., Strominger, J. & Whitesides, G. M. A self-assembled monolayer for the binding and study of histidine tagged proteins by surface plasmon resonance. *Anal Chem* **68**, 490-497 (1996).

51 Lata, S. & Piehler, J. Stable and functional immobilization of histidine-tagged proteins via multivalent chelator headgroups on a molecular poly(ethylene glycol) brush. *Anal Chem* **77**, 1096-1105 (2005).

52 Lata, S., Reichel, A., Brock, R., Tampe, R. & Piehler, J. High-affinity adaptors for switchable recognition of histidine-tagged proteins. *J Am Chem Soc* **127**, 10205-10215 (2005).

53 Ostuni, E., Chapman, R. G., Holmlin, R. E., Takayama, S. & Whitesides, G. M. A survey of structure-property relationships of surfaces that resist the adsorption of protein. *Langmuir* **17**, 5605-5620 (2001).

54 Luk, Y. Y., Kato, M. & Mrksich, M. Self-assembled monolayers of alkanethiolates presenting mannitol groups are inert to protein adsorption and cell attachment. *Langmuir* **16**, 9604-9608 (2000).

55 Chapman, R. G. *et al.* Polymeric thin films that resist the adsorption of proteins and the adhesion of bacteria. *Langmuir* **17**, 1225-1233 (2001).

56 Zalipsky, S. & Harris, J. M. Introduction to chemistry and biological applications of poly(ethylene glycol). *Poly(Ethylene Glycol)* **680**, 1-13 (1997).

57 Crouzet, C., Decker, C. & Marchal, J. Characterization of Primary Reactions of Oxidative-Degradation in Course of Autoxidation of Poly(Oxyethlene)S at 25degreesc - Study in Aqueous-Solution with Initiation by Irradiation of Solvent .8. Kinetic Studies at Ph between 1 and 1. *Makromol Chem* **177**, 145-157 (1976).

58 Hamburger, R., Azaz, E. & Donbrow, M. Autoxidation of Polyoxyethylenic Nonionic Surfactants and of Polyethylene Glycols. *Pharm Acta Helv* **50**, 10-17 (1975).

59 Gerhardt, W. & Martens, C. Oxidation of Polyethyleneoxides and Polyethyleneoxide Ethers - the Formation of Acetaldehyde during the Oxidation of Diethylene Glycol with Oxigen. *Z Chem* **25**, 143-143 (1985).

60 Talarico, T., Swank, A. & Privalle, C. Autoxidation of pyridoxalated hemoglobin polyoxyethylene conjugate. *Biochem Bioph Res Co* **250**, 354-358 (1998).

61 Herold, D. A., Keil, K. & Bruns, D. E. Oxidation of Polyethylene Glycols by Alcohol-Dehydrogenase. *Biochem Pharmacol* **38**, 73-76 (1989).

62 Prime, K. L. & Whitesides, G. M. Adsorption of Proteins onto Surfaces Containing End-Attached Oligo(Ethylene Oxide) - a Model System Using Self-Assembled Monolayers. *J Am Chem Soc* **115**, 10714-10721 (1993).

63 Prime, K. L. & Whitesides, G. M. Self-Assembled Organic Monolayers - Model Systems for Studying Adsorption of Proteins at Surfaces. *Science* **252**, 1164-1167 (1991).

64 Ahmad, S. A., Hucknall, A., Chilkoti, A. & Leggett, G. J. Protein Patterning by UV-Induced Photodegradation of Poly(oligo(ethylene glycol) methacrylate) Brushes. *Langmuir* **26**, 9937-9942 (2010).

65 Alswieleh, A. M., Cheng, N., Leggett, G. J. & Armes, S. P. Spatial Control over Cross-Linking Dictates the pH-Responsive Behavior of Poly(2-(tert-butylamino)ethyl methacrylate) Brushes. *Langmuir* **30**, 1391-1400 (2014).

66 Alswieleh, A. M. *et al.* Zwitterionic Poly(amino acid methacrylate) Brushes. *J Am Chem Soc* **136**, 9404-9413 (2014).

67 Ducker, R. E., Janusz, S., Sun, S. Q. & Leggett, G. J. One-step photochemical introduction of nanopatterned protein-binding functionalities to oligo(ethylene glycol)-terminated self-assembled monolayers. *J Am Chem Soc* **129**, 14842-+ (2007).

68 Ahmad, S. A. A. *et al.* Protein Micro- and Nanopatterning Using Aminosilanes with Protein-Resistant Photolabile Protecting Groups. *J Am Chem Soc* **133**, 2749-2759 (2011).

69 Lopez, G. P., Biebuyck, H. A., Harter, R., Kumar, A. & Whitesides, G. M. Fabrication and Imaging of 2-Dimensional Patterns of Proteins Adsorbed on Self-Assembled Monolayers by Scanning Electron-Microscopy. *J Am Chem Soc* **115**, 10774-10781 (1993).

70 Singhvi, R. *et al.* Engineering Cell-Shape and Function. *Science* **264**, 696-698 (1994).

71 Xia, Y. N. & Whitesides, G. M. Soft lithography. *Angew Chem Int Edit* **37**, 551-575 (1998).

72 Wu, C. C., Reinhoudt, D. N., Otto, C., Velders, A. H. & Subramaniam, V. Protein Immobilization on Ni(II) Ion Patterns Prepared by Microcontact Printing and Dip-Pen Nanolithography. *Acs Nano* **4**, 1083-1091 (2010).

73 Groll, J., Ameringer, T., Spatz, J. P. & Moeller, M. Ultrathin coatings from isocyanate-terminated star PEG prepolymers: Layer formation and characterization. *Langmuir* **21**, 1991-1999 (2005).

74 Groll, J., Haubensak, W., Ameringer, T. & Moeller, M. Ultrathin coatings from isocyanate terminated star PEG prepolymers: Patterning of proteins on the layers. *Langmuir* **21**, 3076-3083 (2005).

75 Christman, K. L. *et al.* Positioning Multiple Proteins at the Nanoscale with Electron Beam Cross-Linked Functional Polymers. *J Am Chem Soc* **131**, 521-527 (2009).

76 Turchanin, A. *et al.* Molecular self-assembly, chemical lithography, and biochemical tweezers: A path for the fabrication of functional nanometer-scale protein arrays. *Adv Mater* **20**, 471-+ (2008).

77 Hoff, J. D., Cheng, L. J., Meyhofer, E., Guo, L. J. & Hunt, A. J. Nanoscale protein patterning by imprint lithography. *Nano Lett* **4**, 853-857 (2004).

78 Escalante, M. *et al.* Directed assembly of functional light harvesting antenna complexes onto chemically patterned surfaces. *Nanotechnology* **19** (2008).

79 Schuller, C. Inelastic light scattering of semiconductor nanostructures - Fundamentals and recent advances. *Springer Trac Mod Ph* **219**, 1-+ (2006).

80 Tsargorodska, A. *et al.* Fast, Simple, Combinatorial Routes to the Fabrication of Reusable, Plasmonically Active Gold Nanostructures by Interferometric Lithography of Self-Assembled Monolayers. *Acs Nano* **8**, 7858-7869 (2014).

81 Adams, J. *et al.* Large-Area Nanopatterning of Self-Assembled Monolayers of Alkanethiolates by Interferometric Lithography. *Langmuir* **26**, 13600-13606 (2010).

82 Leggett, G. J. Light-directed nanosynthesis: near-field optical approaches to integration of the top-down and bottom-up fabrication paradigms. *Nanoscale* **4**, 1840-1855 (2012).

83 Piner, R. D., Zhu, J., Xu, F., Hong, S. H. & Mirkin, C. A. "Dip-pen" nanolithography. *Science* **283**, 661-663 (1999).

84 Hong, S. H., Zhu, J. & Mirkin, C. A. Multiple ink nanolithography: Toward a multiple-pen nano-plotter. *Science* **286**, 523-525 (1999).

85 Lee, K. B., Park, S. J., Mirkin, C. A., Smith, J. C. & Mrksich, M. Protein nanoarrays generated by dip-pen nanolithography. *Science* **295**, 1702-1705 (2002).

86 Demers, L. M. *et al.* Direct patterning of modified oligonucleotides on metals and insulators by dip-pen nanolithography. *Science* **296**, 1836-1838 (2002).

87 Lim, J. H. *et al.* Direct-write dip-pen nanolithography of proteins on modified silicon oxide surfaces. *Angew Chem Int Edit* **42**, 2309-2312 (2003).

88 Lee, K. B., Lim, J. H. & Mirkin, C. A. Protein nanostructures formed via direct-write dip-pen nanolithography. *J Am Chem Soc* **125**, 5588-5589 (2003).

89 Salaita, K. *et al.* Massively parallel dip-pen nanolithography with 55000-pen two-dimensional arrays. *Angew Chem Int Edit* **45**, 7220-7223 (2006).

90 Hyun, J., Ahn, S. J., Lee, W. K., Chilkoti, A. & Zauscher, S. Molecular recognition-mediated fabrication of protein nanostructures by dip-pen lithography. *Nano Lett* **2**, 1203-1207 (2002).

91 Irvine, E. J., Hernandez-Santana, A., Faulds, K. & Graham, D. Fabricating protein immunoassay arrays on nitrocellulose using Dip-pen lithography techniques. *Analyst* **136**, 2925-2930 (2011).

92 Amro, N. A., Xu, S. & Liu, G. Y. Patterning surfaces using tip-directed displacement and self-assembly. *Langmuir* **16**, 3006-3009 (2000).

93 Wadu-Mesthrige, K., Amro, N. A., Garno, J. C., Xu, S. & Liu, G. Y. Fabrication of nanometer-sized protein patterns using atomic force microscopy and selective immobilization. *Biophys J* **80**, 1891-1899 (2001).

94 Liu, G. Y. & Amro, N. A. Positioning protein molecules on surfaces: A nanoengineering approach to supramolecular chemistry. *P Natl Acad Sci USA* **99**, 5165-5170 (2002).

95 Zhou, D. J., Wang, X. Z., Birch, L., Rayment, T. & Abell, C. AFM study on protein immobilization on charged surfaces at the nanoscale: Toward the fabrication of three-dimensional protein nanostructures. *Langmuir* **19**, 10557-10562 (2003).

96 El Zubir, O., Barlow, I., Leggett, G. J. & Williams, N. H. Fabrication of molecular nanopatterns at aluminium oxide surfaces by nanoshaving of self-assembled monolayers of alkylphosphonates. *Nanoscale* **5**, 11125-11131 (2013).

97 Leggett, G. J. Scanning near-field photolithography-surface photochemistry with nanoscale spatial resolution. *Chem Soc Rev* **35**, 1150-1161 (2006).

98 Betzig, E. & Trautman, J. K. Near-Field Optics - Microscopy, Spectroscopy, and Surface Modification Beyond the Diffraction Limit. *Science* **257**, 189-195 (1992).

99 Reynolds, N. P. *et al.* Directed formation of micro- and nanoscale patterns of functional light-harvesting LH2 complexes. *J Am Chem Soc* **129**, 14625-14631 (2007).

100 Sun, S. Q., Thompson, D. G., Graham, D. & Leggett, G. J. DNA nanofabrication by scanning near-field photolithography of oligo (ethylene glycol) terminated SAMs: Controlled scan-rate dependent switching between head group oxidation and tail group degradation. *J Mater Chem* **21**, 14173-14177 (2011).

101 Wong, L. S., Janusz, S. J., Sun, S. Q., Leggett, G. J. & Micklefield, J. Nanoscale Biomolecular Structures on Self-Assembled Monolayers Generated from Modular Pegylated Disulfides. *Chem-Eur J* **16**, 12234-12243 (2010).

102 Sun, S. Q., Thompson, D., Schmidt, U., Graham, D. & Leggett, G. J. Micro-/nano-patterning of DNA and rapid readout with SERS tags. *Chem Commun* **46**, 5292-5294 (2010).

103 Sun, S. Q., Chong, K. S. L. & Leggett, G. J. Nanoscale molecular patterns fabricated by using scanning near-field optical lithography. *J Am Chem Soc* **124**, 2414-2415 (2002).

104 Reynolds, N. P. *et al.* Site-Specific Immobilization and Micrometer and Nanometer Scale Photopatterning of Yellow Fluorescent Protein on Glass Surfaces. *J Am Chem Soc* **131**, 896-+ (2009).

105 Sener, M. K., Olsen, J. D., Hunter, C. N. & Schulten, K. Atomic-level structural and functional model of a bacterial photosynthetic membrane vesicle. *P Natl Acad Sci USA* **104**, 15723-15728 (2007).

106 Harvey Lodish, A. B., S Lawrence Zipursky, Paul Matsudaira, David Baltimore, and James Darnell. Molecular Cell Biology. *New York: W. H. Freeman* (2003).

107 Ng, W. W., Hong, C. S. & Yariv, A. Holographic Interference Lithography for Integrated-Optics. *Ieee T Electron Dev* **25**, 1193-1200 (1978).

108 Brueck, S. R. J. Optical and interferometric lithography - Nanotechnology enablers. *P Ieee* **93**, 1704-1721 (2005).

109 Wachulak, P. W., Capeluto, M. G., Menoni, C. S., Rocca, J. J. & Marconi, M. C. Nanopatterning in a compact setup using table top extreme ultraviolet lasers. *Opto-Electron Rev* **16**, 444-450 (2008).

110 Synge, E. H. A suggested method for extending microscopic resolution into the ultra-microscopic region. *Philos Mag* **6**, 356-362 (1928).

111 Synge, E. H. A microscopic method. *Philos Mag* **11**, 65-80 (1931).

112 Lewis, A., Isaacson, M., Harootunian, A. & Muray, A. Development of a 500-a Spatial-Resolution Light-Microscope .1. Light Is Efficiently Transmitted through Gamma-16 Diameter Apertures. *Ultramicroscopy* **13**, 227-231 (1984).

113 Pohl, D. W., Denk, W. & Lanz, M. Optical Stethoscopy - Image Recording with Resolution Lambda/20. *Appl Phys Lett* **44**, 651-653 (1984).

114 Tadmor, R. Line energy and the relation between advancing, receding, and young contact angles. *Langmuir* **20**, 7659-7664 (2004).

115 Bico, J., Marzolin, C. & Quere, D. Pearl drops. *Europhys Lett* **47**, 220-226 (1999).

116 *http://en.wikipedia.org/wiki/File:Video_contact_angle.gif*.

117 Ohlidal, I. & Franta, D. Ellipsometry of Thin Film Systems. *Prog Opt* **41**, 181-282 (2000).

118 *http://commons.wikimedia.org/wiki/File:Ellipsometry_setup.svg*.

119 Binnig, G., Quate, C. F. & Gerber, C. Atomic Force Microscope. *Phys Rev Lett* **56**, 930-933 (1986).

120 Leggett, G. J. Friction force microscopy of self-assembled monolayers: probing molecular organisation at the nanometre scale. *Anal Chim Acta* **479**, 17-38 (2003).

121 Martin, Y., Williams, C. C. & Wickramasinghe, H. K. Atomic Force Microscope Force Mapping and Profiling on a Sub 100-a Scale. *J Appl Phys* **61**, 4723-4729 (1987).

122 Neubauer, G., Cohen, S. R., Mcclelland, G. M., Horne, D. & Mate, C. M. Force Microscopy with a Bidirectional Capacitance Sensor. *Rev Sci Instrum* **61**, 2296-2308 (1990).

123 Alexander, S. *et al.* An Atomic-Resolution Atomic-Force Microscope Implemented Using an Optical-Lever. *J Appl Phys* **65**, 164-167 (1989).

124 *http://en.wikipedia.org/wiki/Atomic_force_microscopy*.

125 Junno, T., Anand, S., Deppert, K., Montelius, L. & Samuelson, L. Contact Mode Atomic-Force Microscopy Imaging of Nanometer-Sized Particles. *Appl Phys Lett* **66**, 3295-3297 (1995).

126 Drake, B. *et al.* Imaging Crystals, Polymers, and Processes in Water with the Atomic Force Microscope. *Science* **243**, 1586-1589 (1989).

127 Hansma, P. K. *et al.* Tapping Mode Atomic-Force Microscopy in Liquids. *Appl Phys Lett* **64**, 1738-1740 (1994).

128 Watts, J. F. & Wolstenholme, J. *An introduction to surface analysis by XPS and AES*. (J. Wiley, 2003).

129 Briggs, D. *Surface analysis of polymers by XPS and static SIMS*. Digitally printed 1st pbk. edn, (Cambridge University Press, 2005).

130 *http://en.wikipedia.org/wiki/X-ray_photoelectron_spectroscopy*.

131 Blomfield, C. J. Spatially resolved X-ray photoelectron spectroscopy. *J Electron Spectrosc* **143**, 241-249 (2005).

132 Briggs, D. & Beamson, G. Primary and Secondary Oxygen-Induced C1s Binding-Energy Shifts in X-Ray Photoelectron-Spectroscopy of Polymers. *Anal Chem* **64**, 1729-1736 (1992).

133 D. Briggs, M. P. S. in *Practical Surface Analysis by Auger and X-ray Photoelectron Spectroscopy* 429-431 (John Wiley & Sons Ltd., 1983).

134 John F. Watts, J. W. *An Introduction to Surface Analysis by XPS and AES*. 73-76 (John Wiley & Sons Ltd., 2003).

135 Minsky, M. Memoir on Inventing the Confocal Scanning Microscope. *Scanning* **10**, 128-138 (1988).

136 Tata, B. V. R. & Raj, B. Confocal laser scanning microscopy: Applications in material science and technology. *B Mater Sci* **21**, 263-278 (1998).

137 Wright, S. J. & Wright, D. J. Introduction to confocal microscopy. *Method Cell Biol* **70**, 1-+ (2002).

138 Vickerman, J. C. *Surface Analysis - The principal Techniques*. 457 (Wiley, 1997).

139 *http://en.wikipedia.org/wiki/Secondary_ion_mass_spectrometry*.

140 Kim, J., Cho, J., Seidler, P. M., Kurland, N. E. & Yadavalli, V. K. Investigations of Chemical Modifications of Amino-Terminated Organic Films on Silicon Substrates and Controlled Protein Immobilization. *Langmuir* **26**, 2599-2608 (2010).

141 Aissaoui, N., Bergaoui, L., Landoulsi, J., Lambert, J. F. & Boujday, S. Silane Layers on Silicon Surfaces: Mechanism of Interaction, Stability, and Influence on Protein Adsorption. *Langmuir* **28**, 656-665 (2012).

142 Rozlosnik, N., Gerstenberg, M. C. & Larsen, N. B. Effect of solvents and concentration on the formation of a self-assembled monolayer of octadecylsiloxane on silicon (001). *Langmuir* **19**, 1182-1188 (2003).

143 Legrange, J. D., Markham, J. L. & Kurkjian, C. R. Effects of Surface Hydration on the Deposition of Silane Monolayers on Silica. *Langmuir* **9**, 1749-1753 (1993).

144 Stevens, M. J. Thoughts on the Structure of alkylsilane monolayers. *Langmuir* **15**, 2773-2778 (1999).

145 Zeng, X. X., Xu, G. H., Gao, Y. A. & An, Y. Surface Wettability of (3-Aminopropyl)triethoxysilane Self-Assembled Monolayers. *J Phys Chem B* **115**, 450-454 (2011).

146 Samha, H., Linford, M., Zhang, F., Davis, R. & Sautter, K. Chemical vapor deposition of three aminosilanes on silicon dioxide: Surface characterization, stability, effects of silane concentration, and cyanine dye adsorption. *Abstr Pap Am Chem S* **241** (2011).

147 Howarter, J. A. & Youngblood, J. P. Optimization of silica silanization by 3-aminopropyltriethoxysilane. *Langmuir* **22**, 11142-11147 (2006).

148 Zhu, M. J., Lerum, M. Z. & Chen, W. How To Prepare Reproducible, Homogeneous, and Hydrolytically Stable Aminosilane-Derived Layers on Silica. *Langmuir* **28**, 416-423 (2012).

149 Acres, R. G. *et al.* Molecular Structure of 3-Aminopropyltriethoxysilane Layers Formed on Silanol-Terminated Silicon Surfaces. *J Phys Chem C* **116**, 6289-6297 (2012).

150 Fadeev, A. Y. & McCarthy, T. J. Self-assembly is not the only reaction possible between alkyltrichlorosilanes and surfaces: Monomolecular and oligomeric covalently attached layers of dichloro- and trichloroalkylsilanes on silicon. *Langmuir* **16**, 7268-7274 (2000).

151 Kanan, S. A., Tze, W. T. Y. & Tripp, C. P. Method to double the surface concentration and control the orientation of adsorbed (3-aminopropyl)dimethylethoxysilane on silica powders and glass slides. *Langmuir* **18**, 6623-6627 (2002).

152 Rai, V. R. & Agarwal, S. Mechanism of Self-catalytic Atomic Layer Deposition of Silicon Dioxide Using 3-Aminopropyl Triethoxysilane, Water, and Ozone. *Chem Mater* **23**, 2312-2316 (2011).

153 Mcgovern, M. E., Kallury, K. M. R. & Thompson, M. Role of Solvent on the Silanization of Glass with Octadecyltrichlorosilane. *Langmuir* **10**, 3607-3614 (1994).

154 Pasternack, R. M., Amy, S. R. & Chabal, Y. J. Attachment of 3-(Aminopropyl)triethoxysilane on Silicon Oxide Surfaces: Dependence on Solution Temperature. *Langmuir* **24**, 12963-12971 (2008).

155 Cassie, A. B. D. & Baxter, S. Wettability of porous surfaces. *T Faraday Soc* **40**, 0546-0550 (1944).

156 Kenseth, J. R., Harnisch, J. A., Jones, V. W. & Porter, M. D. Investigation of approaches for the fabrication of protein patterns by scanning probe lithography. *Langmuir* **17**, 4105-4112 (2001).

157 Lussi, J. W. *et al.* Selective molecular assembly patterning at the nanoscale: a novel platform for producing protein patterns by electron-beam lithography on SiO2/indium tin oxide-coated glass substrates. *Nanotechnology* **16**, 1781-1786 (2005).

158 Salaita, K., Wang, Y. H. & Mirkin, C. A. Applications of dip-pen nanolithography. *Nat Nanotechnol* **2**, 145-155 (2007).

159 Eichinger, C. D., Hsiao, T. W. & Hlady, V. Multiprotein Microcontact Printing with Micrometer Resolution. *Langmuir* **28**, 2238-2243 (2012).

160 Chalmeau, J., Thibault, C., Carcenac, F. & Vieu, C. Micro-contact printing of two different biomolecules in one step using deformable poly(dimethylsiloxane)-based stamp. *Jpn J Appl Phys* **47**, 5221-5225 (2008).

161 Xu, H. *et al.* Microcontact Printing of Dendrimers, Proteins, and Nanoparticles by Porous Stamps. *J Am Chem Soc* **131**, 797-803 (2009).

162 Kim, M. *et al.* Addressable Micropatterning of Multiple Proteins and Cells by Microscope Projection Photolithography Based on a Protein Friendly Photoresist. *Langmuir* **26**, 12112-12118 (2010).

163 Kwon, K. W., Choi, J. C., Suh, K. Y. & Doh, J. Multiscale Fabrication of Multiple Proteins and Topographical Structures by Combining Capillary Force Lithography and Microscope Projection Photolithography. *Langmuir* **27**, 3238-3243 (2011).

164 Reuther, C., Tucker, R., Ionov, L. & Diez, S. Programmable Patterning of Protein Bioactivity by Visible Light. *Nano Lett* **14**, 4050-4057 (2014).

165 Midthun, K. M. *et al.* Orthogonal Patterning of Multiple Biomolecules Using an Organic Fluorinated Resist and Imprint Lithography. *Biomacromolecules* **14**, 993-1002 (2013).

166 Huang, M. *et al.* Reusable Nanostencils for Creating Multiple Biofunctional Molecular Nanopatterns on Polymer Substrate. *Nano Lett* **12**, 4817-4822 (2012).

167 Biebricher, A., Paul, A., Tinnefeld, P., Golzhauser, A. & Sauer, M. Controlled three-dimensional immobilization of biomolecules on chemically patterned surfaces. *J Biotechnol* **112**, 97-107 (2004).

168 Zhang, G. J. *et al.* Nanoscale patterning of protein using electron beam lithography of organosilane self-assembled monolayers. *Small* **1**, 833-837 (2005).

169 Pesen, D. *et al.* Patterning of protein templates by electron beam lithography. *Biophys J*, 163a-163a (2007).

170 Bat, E., Lee, J., Lau, U. Y. & Maynard, H. D. Trehalose glycopolymer resists allow direct writing of protein patterns by electron-beam lithography. *Nat Commun* **6** (2015).

171 Tang, Q. L., Zhang, Y. X., Chen, L. H., Yan, F. N. & Wang, R. Protein delivery with nanoscale precision. *Nanotechnology* **16**, 1062-1068 (2005).

172 Xu, S. & Liu, G. Y. Nanometer-scale fabrication by simultaneous nanoshaving and molecular self-assembly. *Langmuir* **13**, 127-129 (1997).

173 Shi, J. J., Chen, J. X. & Cremer, P. S. Sub-100 nm Patterning of supported bilayers by nanoshaving lithography. *J Am Chem Soc* **130**, 2718-+ (2008).

174 Chwang, A. B., Granstrom, E. L. & Frisbie, C. D. Fabrication of a sexithiophene semiconducting wire: Nanoshaving with an atomic force microscope tip. *Adv Mater* **12**, 285-288 (2000).

175 Sun, S. Q. & Leggett, G. J. Micrometer and nanometer scale photopatterning of self-assembled monolayers of phosphonic acids on aluminum oxide. *Nano Lett* **7**, 3753-3758 (2007).

176 Ducker, R. E. & Leggett, G. J. A mild etch for the fabrication of three-dimensional nanostructures in gold. *J Am Chem Soc* **128**, 392-393 (2006).

177 Sun, S. Q. *et al.* Fabrication of biological nanostructures by scanning near-field photolithography of chloromethylphenylsiloxane monolayers. *Nano Lett* **6**, 29-33 (2006).

178 Montague, M. *et al.* Fabrication of biomolecular nanostructures by scanning near-field photolithography of oligo(ethylene glycol)-terminated self-assembled monolayers. *Langmuir* **23**, 7328-7337 (2007).

179 Bhushan, K. R., DeLisi, C. & Laursen, R. A. Synthesis of photolabile 2-(2-nitrophenyl)propyloxycarbonyl protected amino acids. *Tetrahedron Lett* **44**, 8585-8588 (2003).

180 Pirrung, M. C., Wang, L. X. & Montague-Smith, M. P. 3 '-nitrophenylpropyloxycarbonyl (NPPOC) protecting groups for high-fidelity automated 5 ' -> 3 ' photochemical DNA synthesis. *Org Lett* **3**, 1105-1108 (2001).

181 Beier, M. & Hoheisel, J. D. Production by quantitative photolithographic synthesis of individually quality checked DNA microarrays. *Nucleic acids research* **28**, E11 (2000).

182 Hasan, A. *et al.* Photolabile protecting groups for nucleosides: Synthesis and photodeprotection rates. *Tetrahedron* **53**, 4247-4264 (1997).

183 Schirmeister, H., Himmelsbach, F. & Pfleiderer, W. Nucleosides .51. The 2-(4-Nitrophenyl)Ethoxycarbonyl (Npeoc) and 2-(2,4-Dinitrophenyl)Ethoxycarbonyl (Dnpeoc) Groups for Protection of Hydroxy Functions in Ribonucleosides and 2'-Deoxyribonucleosides. *Helv Chim Acta* **76**, 385-401 (1993).

184 Lang, H. *et al.* Nucleotides - LXIII - New 2-(4-nitrophenyl)ethyl(npe)- and 2-(4-nitrophenyl)ethoxycarbonyl(npeoc)-protected 2 '-deoxyribonucleosides and their 3 '-phosphoramidites - Versatile building blocks for oligonucleotide synthesis. *Helv Chim Acta* **82**, 2172-2185 (1999).

185 Hermann, C., Kvassiouk, E. & Pfleiderer, W. New Building Blocks for Photolithographic Syntheses of Oligoribonucleotides. *Helv Chim Acta* **94**, 362-370 (2011).

186 Moon, J. H. *et al.* Selective cleavage of the nitro group from a nitrophenyl monolayer by synchrotron soft X-ray. *Langmuir* **14**, 5673-5675 (1998).

187 Koepke, J., Hu, X. C., Muenke, C., Schulten, K. & Michel, H. The crystal structure of the light-harvesting complex II (B800-850) from Rhodospirillum molischianum. *Structure* **4**, 581-597 (1996).

188 Binder, W. H., Barragan, V. & Menger, F. M. Domains and rafts in lipid membranes. *Angew Chem Int Edit* **42**, 5802-5827 (2003).

189 Simons, K. & Toomre, D. Lipid rafts and signal transduction. *Nat Rev Mol Cell Bio* **1**, 31-39 (2000).

190 Chevalier, S. *et al.* Creating Biomimetic Surfaces through Covalent and Oriented Binding of Proteins. *Langmuir* **26**, 14707-14715 (2010).

191 Zhao, W. W., Xu, J. J. & Chen, H. Y. Photoelectrochemical DNA Biosensors. *Chem Rev* **114**, 7421-7441 (2014).

192 Tamura, T. & Hamachi, I. Recent Progress in Design of Protein-Based Fluorescent Biosensors and Their Cellular Applications. *Acs Chem Biol* **9**, 2708-2717 (2014).

193 Ma, H. C. & Horiuchi, K. Y. Chemical microarray: a new tool for drug screening and discovery. *Drug Discov Today* **11**, 661-668 (2006).

194 Miller, J. C. *et al.* Antibody microarray profiling of human prostate cancer sera: Antibody screening and identification of potential biomarkers. *Proteomics* **3**, 56-63 (2003).

195 Hayden, C. C., Hwang, J. S., Abate, E. A., Kent, M. S. & Sasaki, D. Y. Directed Formation of Lipid Membrane Microdomains as High Affinity Sites for His-Tagged Proteins. *J Am Chem Soc* **131**, 8728-+ (2009).

196 Wegner, G. J., Lee, N. J., Marriott, G. & Corn, R. M. Fabrication of histidine-tagged fusion protein arrays for surface plasmon resonance imaging studies of protein-protein and protein-DNA interactions. *Anal Chem* **75**, 4740-4746 (2003).

197 Zayats, M., Kanwar, M., Ostermeier, M. & Searson, P. C. Surface-tethered protein switches. *Chem Commun* **47**, 3398-3400 (2011).

198 Maury, P. *et al.* Creating nanopatterns of his-tagged proteins on surfaces by nanoimprint lithography using specific NiNTA-Histidine interactions. *Small* **3**, 1584-1592 (2007).

199 Wolfram, T., Belz, F., Schoen, T. & Spatz, J. P. Site-specific presentation of single recombinant proteins in defined nanoarrays. *Biointerphases* **2**, 44-48 (2007).

200 Tinazli, A., Piehler, J., Beuttler, M., Guckenberger, R. & Tampe, R. Native protein nanolithography that can write, read and erase. *Nat Nanotechnol* **2**, 220-225 (2007).

201 Gautrot, J. E., Huck, W. T. S., Welch, M. & Ramstedt, M. Protein-Resistant NTA-Functionalized Polymer Brushes for Selective and Stable Immobilization of Histidine-Tagged Proteins. *Acs Appl Mater Inter* **2**, 193-202 (2010).

202 Kang, E. *et al.* Specific adsorption of histidine-tagged proteins on silica surfaces modified with Ni2+/NTA-derivatized poly(ethylene glycol). *Langmuir* **23**, 6281-6288 (2007).

203 Kolb, H. C., Finn, M. G. & Sharpless, K. B. Click chemistry: Diverse chemical function from a few good reactions. *Angew Chem Int Edit* **40**, 2004-+ (2001).

204 Huisgen, R. Centenary Lecture - 1,3-Dipolar Cycloadditions. *P Chem Soc London*, 357-& (1961).

205 Collman, J. P., Devaraj, N. K., Eberspacher, T. P. A. & Chidsey, C. E. D. Mixed azide-terminated monolayers: A platform for modifying electrode surfaces. *Langmuir* **22**, 2457-2464 (2006).

206 Devadoss, A. & Chidsey, C. E. D. Azide-modified graphitic surfaces for covalent attachment of alkyne-terminated molecules by "click" chemistry. *J Am Chem Soc* **129**, 5370-+ (2007).

207 Das, A. K., Engelhard, M. H., Liu, F., Bullock, R. M. & Roberts, J. A. S. The Electrode as Organolithium Reagent: Catalyst-Free Covalent Attachment of Electrochemically Active Species to an Azide-Terminated Glassy Carbon Electrode Surface. *Inorg Chem* **52**, 13674-13684 (2013).

208 Gole, A. & Murphy, C. J. Azide-derivatized gold nanorods: Functional materials for "Click" chemistry. *Langmuir* **24**, 266-272 (2008).

209 Wang, Y. *et al.* Reduction-Degradable Linear Cationic Polymers as Gene Carriers Prepared by Cu(I)-Catalyzed Azide-Alkyne Cycloaddition. *Biomacromolecules* **12**, 66-74 (2011).

210 Lummerstorfer, T. & Hoffmann, H. Click chemistry on surfaces: 1,3-dipolar cycloaddition reactions of azide-terminated monolayers on silica. *J Phys Chem B* **108**, 3963-3966 (2004).

211 Yan, M. D. & Ren, J. Covalent immobilization of ultrathin polymer films by thermal activation of perfluorophenyl azide. *Chem Mater* **16**, 1627-1632 (2004).

212 Burdzinski, G. *et al.* Early events in the photochemistry of aryl azides from femtosecond UV/vis spectroscopy and quantum chemical calculations. *J Am Chem Soc* **128**, 13402-13411 (2006).

213 El Zubir, O. *et al.* Generic Methods for Micrometer- And Nanometer-Scale Surface Derivatization Based on Photochemical Coupling of Primary Amines to Monolayers of Aryl Azides on Gold and Aluminum Oxide Surfaces. *Langmuir* **29**, 1083-1092 (2013).

214 Wollman, E. W., Kang, D., Frisbie, C. D., Lorkovic, I. M. & Wrighton, M. S. Photosensitive Self-Assembled Monolayers on Gold - Photochemistry of Surface-Confined Aryl Azide and Cyclopentadienylmanganese Tricarbonyl. *J Am Chem Soc* **116**, 4395-4404 (1994).

215 Keana, J. F. W. & Cai, S. X. New Reagents for Photoaffinity-Labeling - Synthesis and Photolysis of Functionalized Perfluorophenyl Azides. *J Org Chem* **55**, 3640-3647 (1990).

216 Soundararajan, N. & Platz, M. S. Descriptive Photochemistry of Polyfluorinated Azide Derivatives of Methyl Benzoate. *J Org Chem* **55**, 2034-2044 (1990).

217 Leyva, E., Platz, M. S., Persy, G. & Wirz, J. Photochemistry of Phenyl Azide - the Role of Singlet and Triplet Phenylnitrene as Transient Intermediates. *J Am Chem Soc* **108**, 3783-3790 (1986).

218 Leyva, E. & Platz, M. S. The Temperature-Dependent Photochemistry of Phenyl Azide in Diethylamine. *Tetrahedron Lett* **26**, 2147-2150 (1985).

219 Marcinek, A., Leyva, E., Whitt, D. & Platz, M. S. Evidence for Stepwise Nitrogen Extrusion and Ring Expansion Upon Photolysis of Phenyl Azide. *J Am Chem Soc* **115**, 8609-8612 (1993).

220 Leyva, E., Young, M. J. T. & Platz, M. S. High Yields of Formal Ch Insertion Products in the Reactions of Polyfluorinated Aromatic Nitrenes. *J Am Chem Soc* **108**, 8307-8309 (1986).

221 Leyva, E., de Loera, D. & Leyva, S. Photochemistry of 7-azide-1-ethyl-3-carboxylate-6,8-difluoroquinolone: a novel reagent for photoaffinity labeling. *Tetrahedron Lett* **49**, 6759-6761 (2008).